Modeling, Analysis, Simulation and Real-Time Hardware In-The-Loop Implementation of Hybrid/Electric Vehicles' Powertrain

by

Ahmed S. Abdelrahman

A thesis submitted to the
School of Graduate and Postdoctoral Studies in partial
fulfillment of the requirements for the degree of

Doctor of Philosophy in Electrical Engineering

Department of Electrical, Computer and Software Engineering/ Faculty of Engineering and Applied Science

University of Ontario Institute of Technology

Oshawa, Ontario, Canada

March 2019

© Ahmed Abdelrahman, 2019

THESIS EXAMINATION INFORMATION

Submitted by: **Ahmed Abdelrahman**

Ph.D. in **Elecrical Engineering**

Thesis title: Modeling, Analysis, Simulation and Real-Time Hardware In-The-Loop Implementation of Hybrid/Electric Vehicles' Powertrain

An oral defense of this thesis took place on **March 1st, 2019** in front of the following examining committee:

Examining Committee:

Chair of Examining Committee	Dr. Shahram Heydari
Research Supervisor	Dr. Mohamed Youssef
Examining Committee Member	Dr. Sheldon S. Williamson
Examining Committee Member	Dr. Jing Ren
Examining Committee Member	Dr. Hossam Gaber
University Examiner	Dr. Yuping He
External Examiner	Dr. AYMAN EL-REFAIE, Professor, Marquette University

The above committee determined that the thesis is acceptable in form and content and that a satisfactory knowledge of the field covered by the thesis was demonstrated by the candidate during an oral examination. A signed copy of the Certificate of Approval is available from the School of Graduate and Postdoctoral Studies.

Abstract

Two of the major revolutions, during the last decade, are the automotive industry's hybrid electric vehicles (HEVs) and electric vehicles (EVs). Consequently, and driven by the economic directives, they are getting more attention in the eyes of electrical engineers, automotive corporations and researchers worldwide.

Powertrain is considered to be the most important part in HEVs/EVs from a cost and performance perspective; as it converts electrical power to mechanical power. Hence, providing an accurate engineering model for it, is crucial to precisely size its components and investigate the dynamic performance of any HEV/EV for a better performance

This thesis investigates modeling, analysis and simulation of propulsion system in HEVs/EVs with particular emphasis on transient modeling. To achieve that, a novel complete simulation model on PSIM platform has been performed; proved worthy on two commercially existing cars in the market, namely Chevy Volt and Nissan Leaf. This was done using real data obtained from the Oak Ridge National Laboratory and the Environmental Protection Agency (EPA). Another milestone is that the simulation results have been validated experimentally in real-time through using Hardware in-the Loop (HIL) technology. In this thesis, the main focus is to develop a versatile generic approach based on transient analysis of HEVs/EVs propulsion powertrain. Moreover, evaluates the power train performance when incorporated with new futuristic innovative components. For example, a new proposed two-speed transmission system developed by inMotive corporation that can be applied to most of electrified vehicles. Further, wide band gap (WBG) devices such as GaN semiconductors and SiC devices have been integrated in the system, one at a time. A comparison study in terms of total power losses and efficiency calculations at different temperatures and switching frequencies due to using each of them has been

accomplished. This approach is not only considering the system dynamics through controlling different state variables, but also implementing a daily real driving cycle to emulate exactly the same real driving environment. For a sound design, the developed model, which has low computational intensity, is utilized to determine the proper sizing and later the dynamic behavior of the main components such as battery, DC-DC converter, DC-AC converter and electrical motor..

To prove the versatility of the developed model, it was tried on permanent magnet based cars (Chevy Volt and Nissan Leaf) and futuristic high performance induction motors (Audi eTron) A thorough investigation of the performance of three different topologies of induction motors; singly-fed induction motor (SFIM), doubly-fed induction motor (DFIM), and cascaded doubly-fed induction motor (CDFIM) has been conducted. This performance comparison is supported by a comprehensive finite element analysis and cost assessment to obtain the best candidate to be used in HEVs/EVs applications.

Keywords: Plug-in Hybrid Electric Vehicles (PHEVs); Battery Electric Vehicles (BEVs); Permanent magnet synchronous motor (PMSM); Real-time Simulation; Hardware in-the-Loop (HIL); Wide Band Gap (WBG) devices.

AUTHOR'S DECLARATION

I hereby declare that this thesis consists of original work of which I have authored. This is a true copy of the thesis, including any required final revisions, as accepted by my examiners.

I authorize the University of Ontario Institute of Technology to lend this thesis to other institutions or individuals for the purpose of scholarly research. I further authorize University of Ontario Institute of Technology to reproduce this thesis by photocopying or by other means, in total or in part, at the request of other institutions or individuals for the purpose of scholarly research. I understand that my thesis will be made electronically available to the public.

Ahmed S. Abdelrahman

Acknowledgment

First and foremost, I thank God the almighty and the most merciful, for the success of this thesis.

I express my sincere gratitude towards Dr. Mohamed Youssef, my advisor, for his guidance and support over the course of my doctorate program. I am incredibly grateful to him to have given me an opportunity to conduct research in my area of interest.

My heartfelt thanks are extended to my family for giving me the determination to overcome many trying moments to pursue my dreams and to my colleagues who helped me a lot over the course of my PhD.

To my wonderful daughters, thank you for bearing with me and being my greatest supporter. To my incredible wife, my friend, mentor and critic, thank you for not letting me give up and for giving me all the encouragement I needed to continue.

Last but not least this dissertation is dedicated to my late father who has been my constant source of inspiration. His constant love and support has meant more than anything. May his kind soul rest in peace.

My Beloved Dad, this is for you!!

TABLE OF CONTENTS

Abstract ii
Acknowledgment v
TABLE OF CONTENTS vi
LIST OF TABLES ix
LIST OF FIGURES x
Nomenclature xv
Abbreviations xviii
1 Chapter 1. Introduction 1
1.1 Background 1
1.2 Historical Development of the Power Train 2
1.2.1 Steam-Engine Powered Vehicle 2
1.2.2 Electric Vehicles 3
1.2.3 Internal Combustion Engine Powered Vehicles 3
1.3 Transportation New Alternatives 4
1.3.1 All-Electric Vehicles (EVs) 4
1.3.2 Hybrid Electric Vehicles (HEVs) 5
1.3.2.1 Series Hybrid 6
1.3.2.2 Parallel Hybrid 7
1.3.2.3 Series-Parallel Configurations 8
1.3.2.4 Complex Hybrid System 9
1.4 Motivation of the Thesis 10
1.5 Scope and Objectives of the Thesis 11
1.6 Contributions 14
1.7 Thesis Outlines 19
2 Chapter 2. Literature Review 21
2.1 Introduction 21
2.2 Approaches of Dynamical Powertrain Modeling 22
2.3 Transmission Systems Used in Electric Vehicles 24
2.4 Electric Motors for HEV/EV Applications 30
2.4.1 Induction Machines in EV/HEV Applications 32
2.4.1.1 Torque-Speed Capabilities 33
2.4.1.2 Modelling and Control Implementation 34

2.5 Hardware in the Loop Technology 38
2.6 Characteristics and History of WBG Devices 39
2.6.1 Advantages of GaN over SiC: 40
2.7 Chapter Summary 41
3 Chapter 3. Dynamical Modeling of HEV/EV Powertrain 42
3.1 Introduction 42
3.2 Vehicle Model 44
3.2.1 Mechanical Modeling 44
3.2.1.1 Vehicle Dynamics 44
3.3 Intelligent Driver Model 52
3.3.1 Transmission System Modeling 53
3.3.2 Gearshift Model 54
3.3.2.1 First Gear 55
3.3.2.2 Second Gear 56
3.4 Electrical Modeling 57
3.4.1 Motor Modeling 57
3.4.2 Battery Modeling 64
3.4.3 DC-DC Converter Modeling 67
3.4.4 Inverter 70
3.4.5 Controllers 70
3.4.6 Low Level Controllers 71
3.4.6.1 DC Link Controller 71
3.4.6.2 Inverter Controller 71
3.4.6.3 Traction Motor Controller 73
3.4.7 High Level Controllers 76
3.4.7.1 Power Divider Controller 76
3.4.7.2 Main Vehicle Controller 76
3.5 Chapter Summary 76
4 Chapter 4. Simulation Results and Hardware in-the-Loop Implementation 78
4.1 Introduction 78
4.2 Validation of Simulation Results 81
4.3 Impact of Transmission Gear Selection 82
4.4 General Performance Investigation 88

4.5 Hardware in-the Loop (HIL) Experimental Verification 96
4.6 Chapter Summary 105
5 Chapter 5. Comparative Studies for HEV/EV System Efficiency Improvement 107
5.1 Introduction 107
5.2 Wide Band Gap Devices in HEV/EV 107
5.3 Performance Comparison 109
5.3.1 Efficiency and Size Reduction Evaluation 111
5.3.2 Simulation Results 113
5.3.3 Regenerative Braking to 1% of Regular Speed 115
5.3.4 Components Size Reduction 116
5.3.5 Experimental Results 116
5.4 Motor Selection 119
5.4.1 Finite Element Analysis 120
5.4.2 Discussion 128
5.5 Chapter Summary 130
6 Chapter 6. Conclusions and Future Work 132
6.1 Conclusions 132
6.1.1 Developing a Generic Versatile Modeling Approach for HEVs/EVs 132
6.1.2 Integration of a Two-Speed Transmission System 133
6.1.3 Hardware in-the-Loop Implementation 133
6.1.4 Integration of Wide Band Gap Devices 134
6.1.5 Electric Motors Selection 135
6.2 Future Work and Recommendations 136
6.2.1 Analyze Further Transmission Designs 136
6.2.2 Testing New Transportation Systems 136
6.2.3 Further Investigation of the Cascaded Doubly-fed Induction Motor in HEV/EV Applications 136
Appendix A: Modeling Parameters 137
A.1 Nissan Leaf Electric Vehicle 137
A.2 GM Chevrolet Volt 138
References 140

LIST OF TABLES

Table 3-1: Comparison between different modelling approaches 43

Table 4-1: Comparison between single and two-speed transmission 88

Table 4-2: Vehicle speed vs. transmission efficiency 105

Table 5-1: NLEV powertrain's DC/DC converter efficiencies for 50 kHz 111

Table 5-2: Comparison of efficiencies of NLEV's DC/DC converter incorporated with different semiconductors at different frequencies 111

Table 5-3: NLEV powertrain's DC/DC converter efficiencies at 25 ºC 111

Table 5-4: NLEV powertrain's DC/DC converter efficiencies at 150 ºC 111

Table 5-5: Difference in efficiencies at 25 ºC and 150 ºC 112

Table 5-6: Difference in efficiencies from pure Si MOSFET at different frequencies 112

Table 5-7: Reduction in SiC efficiency from GaN 113

Table 5-8: 25 ºC average regenerated power 115

Table 5-9: Percentage of the reduction in the heat sink and filtering components size 116

Table 5-10: Experimental Efficiencies of the Wide-Band Gap 119

Table 5-11: Simulation results comparison of the three motors drive systems 128

Table A-1: Details of 2012 Nissan Leaf machine [121] 137

Table A-2: Battery Parameters [121] 138

Table A-3: CVHEV Battery Parameters [17] 138

Table A-4: Motor parameters [17] 138

Table A-5: Chevy Volt parameters [17] 139

LIST OF FIGURES

Fig. 1.1. Series topology of hybrid electric vehicle [3] 6

Fig. 1.2. Fuel cell topology of hybrid electric vehicle [4] 6

Fig. 1.3. Parallel pre-transmission topology of hybrid electric vehicle [3] 7

Fig. 1.4. Parallel post-transmission topology of hybrid electric vehicle [3]..... 8

Fig. 1.5. Complex topology of hybrid electric vehicle [3]..... 9

Fig. 2.1. Dual cutch transmission layout [54]..... 26

Fig. 2.2. Multi-speed dual clutch transmission schematic diagram [36] 27

Fig. 2.3. Torque/Power – speed characteristics of a motor drive. [78]..... 30

Fig. 2.4. Generic classification of EV/HEV electric motors [79]..... 31

Fig. 2.5. Drive system of singly fed induction motor used in EV/HEV applications [86]..... 34

Fig. 2.6. Drive system of doubly-fed induction motor used in EV/HEV applications [86] 35

Fig. 2.7. Drive system of cascaded doubly fed induction motor used in EV/HEV applications [86]..... 35

Fig. 2.8. Torque/Power - speed characteristics of the three induction motors [86]..... 36

Fig. 2.9. Control scheme of the singly fed induction motor [87]..... 36

Fig. 2.10. Control scheme of the doubly fed induction motor [87] 37

Fig. 2.11. Control scheme of the cascaded doubly fed induction motor [87]..... 37

Fig. 3.1. Sprung mass free body diagram [109]..... 47

Fig. 3.2. Free body diagram of the tire (un-sprung mass) [108]..... 47

Fig. 3.3. Trailing arm free body diagram [108] 48

Fig. 3.4. Driver model schematic..... 53

Fig. 3.5. Transmission system..... 55

Fig. 3.6. Phasor diagram of the PMSM 58

Fig. 3.7. Stationary and rotating reference frames [116] 64

Fig. 3.8. The non-linear model of the battery 65

Fig. 3.9. Design of the GM Chevrolet Volt 66

Fig. 3.10. The V-I characteristics of Li-Ion battery 67

Fig. 3.11. Bidirectional DC-DC converter 68

Fig. 3.12. DC-DC converter in the boost (step-up) mode 69

Fig. 3.13. DC-DC converter in the buck (step-down) mode 69

Fig. 3.14. Schematic diagram of the inverter 70

Fig. 3.15. DC link controller 71

Fig. 3.16. Inverter SVPWM modulation scheme 72

Fig. 3.17. PI controller for MTPA 75

Fig. 3.18. Speed control loop with unity feedback 75

Fig. 3.19. Main vehicle controller 76

Fig. 4.1. Efficiency map of NLEV 2012 motor [121] 80

Fig. 4.2. Efficiency map of NLEV 2012 inverter [121] 80

Fig. 4.3. Combined efficiency map of NLEV 2012 of motor and inverter [121] 81

Fig. 4.4. Powertrain schematic diagram of the NLEV 83

Fig. 4.5. Schematic diagram of the traction motor 83

Fig. 4.6. Three phase currents of the traction motor 84

Fig. 4.7. Direct and quadrature axes currents 84

Fig. 4.8. Power losses inside the DC-DC converter 85

Fig. 4.9. Power losses in the inverter 85

Fig. 4.10. Input and output power in case of lossless Transmission system 86

Fig. 4.11. Input and output power in lossy transmission system 86

Fig. 4.12. Transmission system losses 87

Fig. 4.13. Output power in transmission system 87

Fig. 4.14. Powertrain schemtatic of the GM Chevrolet Volt [107] 90

Fig. 4.15. Schematic diagram of the of the HEV in PSIM [107] 90

Fig. 4.16. 3-ph current waveforms for the stator of the PMSM 91

Fig. 4.17. Speed controller response 91

Fig. 4.18. Torque produced in the PMSM 92

Fig. 4.19. Torque-speed characteristics of the PMSM 92

Fig. 4.20. State of charge graph of the battery 93

Fig. 4.21. Waveform of the battery voltage 93

Fig. 4.22. Waveform of the battery current 94

Fig. 4.23. Waveform of the DC bus voltage 94

Fig. 4.24. Waveform of the current passing through the DC bus 95

Fig. 4.25. Waveform of the pulse width modulation for the IGBTs 95

Fig. 4.26. Topology of the HIL controller 97

Fig. 4.27. Power and control schematics implemented on the HIL platform 97

Fig. 4.28. Power circuit schematic implemented on HIL platform 98

Fig. 4.29. Interface between PSIM simulation and HIL controller 99

Fig. 4.30. Test bench setup of the hardware-in-the loop 100

Fig. 4.31. Real time values of the HIL simulation dashboard 100

Fig. 4.32. 3-phase waveforms of the PMSM currents (5A/div) (HIL Scale 1:8) [Value: 38A] 100

Fig. 4.33. Waveform of the battery voltage (2V/div) (HIL Scale 1:100) [Value: 379V]..... 101

Fig. 4.34. Waveform of the DC bus voltage (2V/div) (HIL Scale 1:100) [Value: 630V]..... 101

Fig. 4.35. PMSM produced torque (200 N.m/div) (HIL Scale 1:100) [Avg. Value: 57 N.m] .. 102

Fig. 4.36. Speed of the permanent magnet synchronous motor (5 rpm/div) (HIL Scale 1:200) [Value: 2010 rpm]..... 102

Fig. 4.37. Pulse-width modulation waveform of the IGBTs..... 103

Fig. 4.38. Motor torque in N.m measured from simulation and HIL 104

Fig. 4.39. Engine speed in rad/sec measured from simulation and HIL..... 104

Fig. 5.1. Power losses in watts for the switch..... 109

Fig. 5.2. Switch losses of in watts at 400 kHz 110

Fig. 5.3. Efficiencies for various devices..... 112

Fig. 5.4. Waveform of battery current (A)..... 113

Fig. 5.5. Waveform of the DC bus voltage (V) 114

Fig. 5.6. Speed of the vehicle in rpm 114

Fig. 5.7. Torque of the vehicle in newton meter..... 115

Fig. 5.8. GaN E-HEMT test bench board 117

Fig. 5.9. SiC ACCUFET test bench board..... 117

Fig. 5.10. PMSM of the test bench 118

Fig. 5.11. Powertrain test bench components (High-power rectifier, DC/DC converter) 118

Fig. 5.12. Turn-on and turn-off instants of zero voltage switching 119

Fig. 5.13.SFIM cross section 121

Fig. 5.14. DFIM cross section..... 121

Fig. 5.15. No-load magnetic flux density of SFIM @1475 rpm..... 122

Fig. 5.16. No-load magnetic flux density of DFIM 122

Fig. 5.17. No-load flux intensity of SFIM 123

Fig. 5.18. No-load flux intensity of DFIM..... 123

Fig. 5.19. Ohmic losses of SFIM 124

Fig. 5.20. Ohmic losses of DFIM 124

Fig. 5.21. 3-Phase currents in SFIM 125

Fig. 5.22. 3-Phase currents in DFIM..... 125

Fig. 5.23. 3-Phase currents of the CDFIM..... 126

Fig. 5.24. Torque speed capability of SFIM 126

Fig. 5.25. Torque in SFIM 127

Fig. 5.26. DFIM torque production..... 127

Fig. 5.27. SFIM assessment from different factors..... 129

Fig. 5.28. DFIM assessment from different factors 129

Fig. 5.29. CDFIM assessment from different factors 130

Nomenclature

Symbol	Meaning	Unit
m_c	Mass of the vehicle	kg
a_c	Acceleration	m/s2
F_T	Traction force	Newton
F_{dr}	Aerodynamic drag force	Newton
F_R	Rolling resistance force	Newton
g	Gravitational acceleration	m/s^2
δ	Road slope	degrees
P_d	The car wheels power demand	Watt
V_c	Car velocity	m/s
ρ	Air density	Kg/m3
A_f	Car frontal area	m^2
C_{dr}	Aerodynamic drag coefficient	-
m_{sm}	Mass of the sprung mass	kg
$\ddot{x}_{sm}$	Longitudinal acceleration of the sprung mass.	m/s^2
F_{j_x}	Longitudinal force	Newton
F_{aer}	Aerodynamic force	Newton
$F_{RG,x_{sm}}$	Sprung mass resistive force	Newton
$\ddot{z}_{sm}$	Vertical acceleration of the sprung mass	m/s^2
$F_{RG,z_{sm}}$	Sprung mass weight force	Newton

J_{sm}	Sprung mass moment of inertia	kg.m2
$\ddot{\theta}_{sm}$	Rotational acceleration of the sprung mass	rad/s2
$H_{CG,sm}$	Center of gravity height	m
x_{us_f}	Longitudinal displacement of the un-sprung mass	m
x_{sm}	Vertical displacement of the sprung mass	m
z_{us_f}	Wheel vertical displacement	m
γ_f	Trailing arm angle	degrees
R_w	Radius of the wheel	m
α	Road angle	degrees
P_t	Tire stiffness coefficient	-
Z_{in_F}	Vertical displacement of the road	m
Z_{us_F}	Unsprung mass vertical displacement	m
C_p	Tire damping coefficient	-
$\dot{Z}_{in_F}$	Road vertical displacement rate change	m/s
$\dot{Z}_{us_F}$	Unsprung mass vertical displacement rate change	m/s
K_f	Suspension stiffness coefficient	-
R_s	Phase winding resistance	Ω (Ohm)
i_s	Phase current	A
L_s	Phase synchronous-inductance	H
y_{PM}	PM flux space phasor	-
A	Voltage drop during the exponential zone	V
a_c	Car acceleration	m/s^2

B	Charge at the end of exponential zone	Coulomb
C_b	The battery Capacity	Ah
F_{dr}	Aerodynamic drag force	Newton
i_b	The battery current	A
K	Polarization Voltage	V
R_{batt}	Series resistance	Ω (Ohm)
SOC	State of Charge	-
V_{qs}	quadrature axis component of stator voltage	V
V_{ds}	direct axis component of stator voltage	V
L_d	direct axis inductance	H
L_q	quadrature axis inductance	H
R_s	stator phase resistance	Ω (Ohm)
i_{ds}	direct axis component of stator current	A
i_{qs}	quadrature axis component of stator current	A
λ_{pm}	flux amplitude established in stator phases by rotor permanent magnets	weber-turn
λ_{ds}	Direct axis component of stator flux	weber-turn
λ_{qs}	Quadrature axis component of stator flux	weber-turn
ω_r	rotor electrical speed	Rad/s

Abbreviations

FOC	Field Oriented Control
DFIM	Doubly-Fed Induction Motor
SFIM	Singly-Fed Induction Motor
CDFIM	Cascaded Doubly Fed-Induction Motor
SVPWM	Space Vector Pulse Width Modulation
CHIL	Controller Hardware in the Loop
PMSM	Permanent Magnet Synchronous Motor
HEV	Hybrid Electric Vehicle
BEV	Battery Electric Vehicle
SiC	Silicon Carbide
GaN	Gallium Nitride

Chapter 1. Introduction

1.1 Background

The anticipated lack of petroleum supply all over the world and the increasing concerns regarding the global warming problem have shifted the industry future plan as well as the universities research laboratories to pay more attention on electric and hybrid electric vehicles. Using this kind of green vehicles, lower greenhouse gas emissions will be much reduced as well as reaching higher energy efficiency levels [1], [2]. The EV/HEV consists of many parts that can be classified in general to electrical and mechanical systems. The propulsion system of the EV/HEV has a great importance due to its main function as the link between the electric system and the mechanical system. Big industrial corporation invest lot of money to better enhance the design of the propulsion system in addition to the battery management system to improve the efficiency and make the design more compact [3], [4].

In this research, we try to model the power train in such a way to follow the industry desires and address the several design challenges in the power stage and the control stage as well. Firstly, we started with modeling the hybrid electric metro car for the first time in Canada. Simulation was performed for propulsion with and without auxiliary power with the assumption of an average power of 40 kW. To size the system for the worst case scenario, the regeneration power will not be taken into account in case the propulsion cuts off during regenerative braking. The hydrogen consumption and storage is also calculated for each case with the tank options listed for each energy storage option Secondly, we moved to the automotive industry and the optimal of transmission gear ratios of a Nissan Leaf EV (NLEV) is investigated. The traditional single ratio gearboxes are replaced by multiple ratio ones. The selection of the gear ratio is proved to have a significant impact on electric vehicle's performance and range. A mathematical model of a NLEV

is developed for both single and multiple ratio transmission systems. The influence of different gear ratios is studied on Nissan Leaf performance. The simulation results reveal a significant effect on the overall efficiency due to integrating a transmission system with a NLEV. Comparisons are performed for both single and two-speed transmissions and results are quantified and discussed. The proposed design used for the automotive applications provides a generic platform to successfully model any electric vehicle. The model is mathematically developed and simulated using PSIM software package.

1.2 Historical Development of the Power Train

1.2.1 Steam-Engine Powered Vehicle

History of the automobile dates back to 1769 when the first steam-engine powered vehicle was introduced in Britain [4]. Steam-engine powered vehicles became more popular and widely accepted in the late 1780's. Stanley Steamer was a steam-engine powered vehicle with an outstanding success. This vehicle could reach speeds of more than 200 km/h and was easy to operate [5]. Although internal combustion engine vehicles and even primitive electric ones existed, they had poor performance and could not compete with steam-engine vehicles.

Despite its relative success and popularity, the steam-engine powered vehicle had several disadvantages. The steam-engine took a while to warm up and there were always concerns of boiler explosions. Moreover, carrying enough water for long trips was virtually impossible, which implied short operating range and therefore limited use in long-haul transportation. These disadvantages pushed engineers to develop more convenient and reliable vehicles.

1.2.2 Electric Vehicles

Electric vehicles have a history as long as other types of vehicles. In fact, they appeared in early 1890's; they however disappeared quickly because they were not able to compete with their competitors in terms of performance.

The first electric vehicle was built by Gustave Trouvé in 1881. It was a tricycle powered by a small dc motor fed by lead–acid batteries [6]. The creation of this vehicle was then followed by the development of more electric vehicles using larger electric motors and battery packs. Improvements in batteries and electric motors made electric vehicle one of the vehicles of choice between 1900 and 1905. However, the limited speed and travel range of these vehicles failed the attempts to keep them in the market. Immature battery technology contributed the most to the failure of electric vehicles.

1.2.3 Internal Combustion Engine Powered Vehicles

In 1806 François Isaac de Rivaz built an internal combustion engine (ICE) powered by an oxygen and hydrogen mixture. More engines were developed after that and they all used gas fuel rather than the liquid fuel commonly used today [5].

Around 1870, Siegfried Marcus built a simple vehicle using a liquid-fueled ICE. This was the first vehicle that used gasoline as the fuel. The ICE was then perfected by Gottlieb Daimler, Karl Benz, Wilhelm Maybach, and Rudolf Diesel during 1870's; but this engine was still noisy, shaky and difficult to start and could not compete with steam-engine powered vehicles and electric vehicles. More developments and marked improvements in ICE-powered vehicles finally shifted the market towards these vehicles, and inevitably led to the demise of other technologies that had a much slower rate of improvement. ICE-powered vehicles set out to dominate the market for almost a century [5].

1.3 Transportation New Alternatives

A potential solution to address both the emissions and fuel consumption due to vehicles is to reduce, or ideally entirely eliminate, the amount of fuel consumed by road vehicles. Several alternative drive-train topologies are proposed to achieve improved efficiency and to reduce or eliminate fuel consumption of conventional vehicles. Electric, hybrid and plug-in hybrid vehicles are the most prominent alternatives proposed for conventional vehicles. These drive-train topologies are briefly described in the following sub-sections [6].

1.3.1 All-Electric Vehicles (EVs)

Electric vehicles use electricity as the only source of energy for their propulsion. An All-electric vehicle is therefore the ultimate solution for elimination of the dispersed pollution caused by vehicles. An all-electric drive-train will have superior efficiency to a conventional gas-powered vehicle, due to the higher efficiency of electrical components such as electric motors and converters, and will have no emissions. However, even with all-electric vehicles, the primary source of energy will likely continue to be, at least for some time, fossil fuels, until renewable sources are developed to fully take over their place. This is because the battery storage of an all-electric vehicle needs to be charged through electricity that will be supplied by power plants using predominantly fossil fuels [7].

In an all-electric drive-train the electrical energy is stored either in batteries or ultra-capacitors. So far the battery industry has not been able to offer suitable batteries to the automotive industry to allow complete adoption of all-electric vehicles. Batteries for electric vehicles need to provide high power to meet the vehicle demand (e.g. during acceleration and deceleration) and they should have high energy density to give the electrical vehicle enough range1. Today, batteries are able to meet the power demand of vehicles but their low energy density is still a bottleneck for electric vehicles [6]. This implies that a current all-electric vehicle will be able to match the acceleration of a conventional vehicle but will not have a comparable range. For example, a recently developed all-electric vehicle,

Nissan Leaf, has a top speed of 144 km/h, which is comparable to a conventional ICE-powered vehicle in the same class. However, its range is limited between 75km to 220km (depending on driving condition) [10]. Conventional ICE-powered vehicles have a range of 500-1000 km. The time required to re-fill the energy storage is another important characteristic of a vehicle. While the gas-tank of a conventional ICE-powered vehicle can be filled within minutes, charging the battery storage of an electric car requires significantly longer periods. For example, charging the batteries of the Nissan Leaf takes 30 minutes using fast chargers (50 kW charger) in dedicated charging stations and 6 hours using an ordinary power outlet (5 kW charger).

1.3.2 Hybrid Electric Vehicles (HEVs)

An intermediate solution during transition from conventional vehicles to all-electric vehicles is a hybrid drive-train. Particularly, a hybrid-electric vehicle (HEV) combines an electric drive system with a conventional gas or diesel engine to provide propulsion [11]. Improved fuel economy is obtained by eliminating wasteful engine idling, recapturing the kinetic energy of the moving vehicle through regenerative braking, and by using the conventional gas engine in operating points where it is more efficient [12]. This leads to less fuel consumption and less reliance on non-renewable sources of energy for transportation, although it does not lead to its ideal elimination.

One of the most common ways to classify HEV is based on configuration of the vehicle powertrain. In this section, three major hybrid vehicle architectures introduced are series, parallel and series-parallel. Until recently, many HEV in production are either series or parallel. In terms of mechanical structure, these two are primitive and relatively simple. A series-parallel powertrain brings in more degrees of freedom to vehicle engine operation with added system complexity [7]–[16].

1.3.2.1 Series Hybrid

One of the basic types of HEV is series hybrid. In this configuration, as shown in Fig. 1.1, the ICE is used to generate electricity in a generator. Electric power produced by the generator goes to either the motor or energy storage systems (ESS). The hybrid power is summed at an electrical node, the motor.

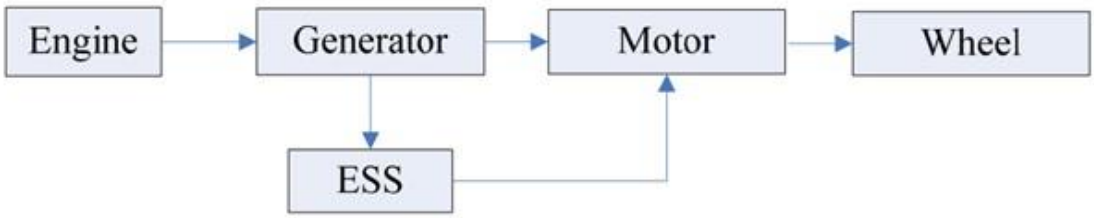

Fig. 1.1. Series topology of hybrid electric vehicle [3]

The series hybrid configuration tends to have a high efficiency at its engine operation. The capacity for the regenerative braking benefits from the full size motor. However, the summed electrical mode has tied up the size of every component. The weight and cost of the vehicle is increased due to the large size of the engine and the required addition of two electric machines. The size of the power electronic unit is also excessive [17]–[21].

The configuration of fuel cell HEV is also technically in series as shown in Fig. 1.2. Since fuel cell generate electric, rather than mechanical power, it functions as a power generator replacing both of the engine and the electric generator. This is the uniqueness of fuel cell powered HEV.

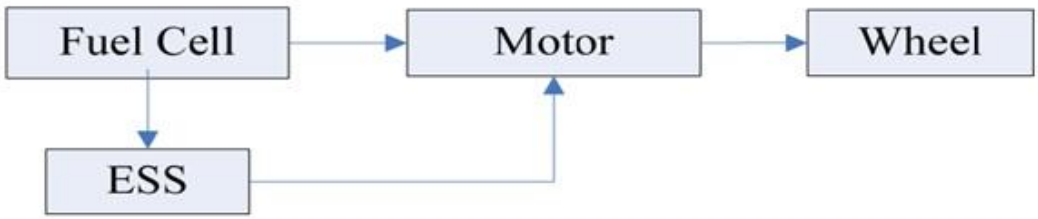

Fig. 1.2. Fuel cell topology of hybrid electric vehicle [4]

1.3.2.2 Parallel Hybrid

The parallel hybrid is another HEV type that has been closely studied. In parallel configurations, both the engine and the motor provide traction power to the wheels, which means that the hybrid power is summed at a mechanical node to power the vehicle. As a result, both of the engine and the motors can be downsized, making the parallel architecture more viable with lower costs and higher efficiency [22]–[30].

The parallel hybrid vehicles usually use the same gearboxes of the counterpart conventional vehicles, either in automatic or manual transmissions. Based on where the gearbox is introduced in the powertrain, there are two typical parallel HEV architectures, named pre-transmission parallel and post-transmission parallel, as shown in Fig. 1.3 and Fig. 1.4, respectively. In a pre-transmission parallel HEV, the gearbox is located on the main drive shaft after the torque coupler. Hence, gear speed ratios apply on both the engine and the electric motor. The power flow is summed at the gearbox. On the other hand, in a post-transmission parallel hybrid, the gearbox is located on the engine shaft prior to the torque coupler. The gearbox speed ratios only apply on the engine. A continuous variable transmission (CVT) can be used to replace conventional gearbox to further improve the engine efficiency.

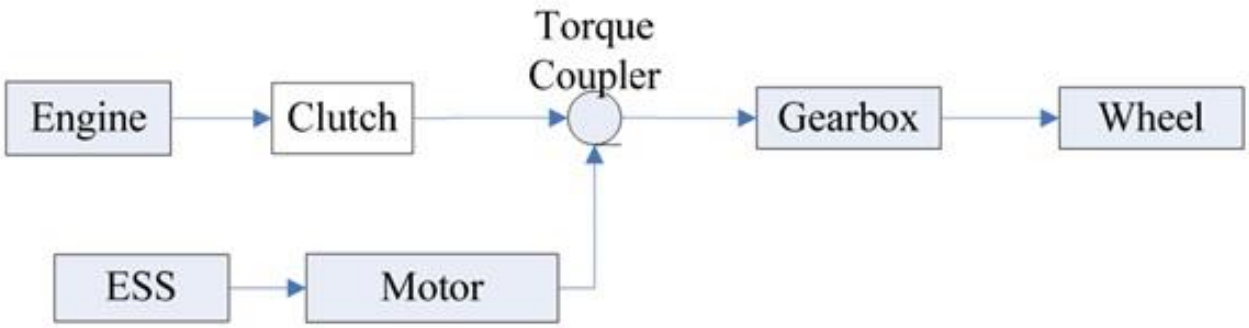

Fig. 1.3. Parallel pre-transmission topology of hybrid electric vehicle [3]

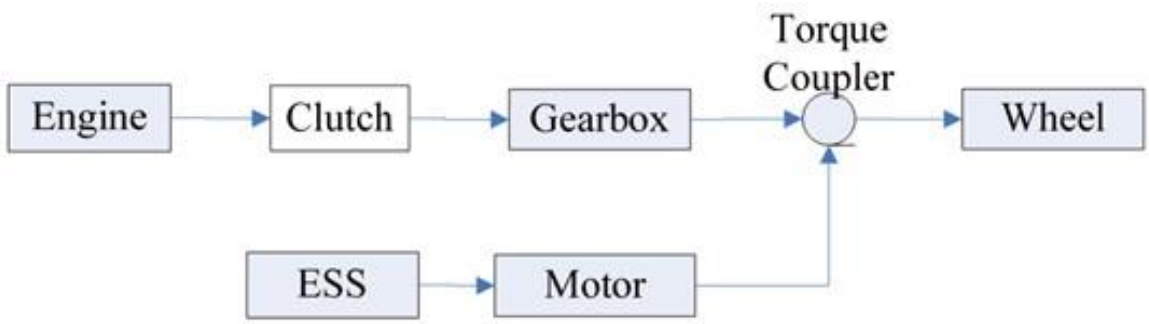

Fig. 1.4. Parallel post-transmission topology of hybrid electric vehicle [3]

In a pre-transmission configuration, torque from the motor is added to the torque from the engine at the input shaft of the gearbox. Contemporary mild parallel hybrid vehicles employ this strategy exclusively. In a post-transmission, the torque from the motor is added to the torque from the engine delivered on the output shaft of the gearbox. A disconnect device such as a clutch is used to disengage the gearbox while running the motor independently [31].

Post-transmission electric hybrids can also be used in hybrid vehicles with a higher degree of hybridization. Hydraulic power can be used in launch-assist devices in heavy-duty trucks and commercial vehicles. There are attempts from different perspectives to improve the operation of a parallel HEV. One possibility is to run the vehicle on electric machine alone in city driving while running engine power alone on highways. Most contemporary parallel vehicles use a complex control system and special algorithms to optimize both vehicle performance and range. The flexibility in powertrain design, in addition to the elimination of the need for a large motor, of parallel hybrids has attracted more interest in HEV development than the series hybrids.

1.3.2.3 Series-Parallel Configurations

In the series-parallel configurations, the vehicle can operate as a series hybrid, a parallel hybrid, or a combination of both. This design depends on the presence of two motors/generators and the connections between them, which can be both electrical and mechanical. The mechanical

connections between the engine and electric machines are usually accomplished by planetary gears known as power-splitting devices (PSDs). One advantage of a series-parallel configuration is that the engine speed can be decoupled from the vehicle speed. This advantage is partially offset by the additional losses in the conversion between mechanical power from engine and electrical energy [32].

1.3.2.4 Complex Hybrid System

The complex hybrid is similar to the series-parallel hybrid since the generator and electric motor is both electric machines. However, the key difference is due to the bi-directional power flow of the electric motor in complex hybrid and the unidirectional power flow of the generator in the series-parallel hybrid. The major disadvantage of complex hybrid is higher complexity [3].

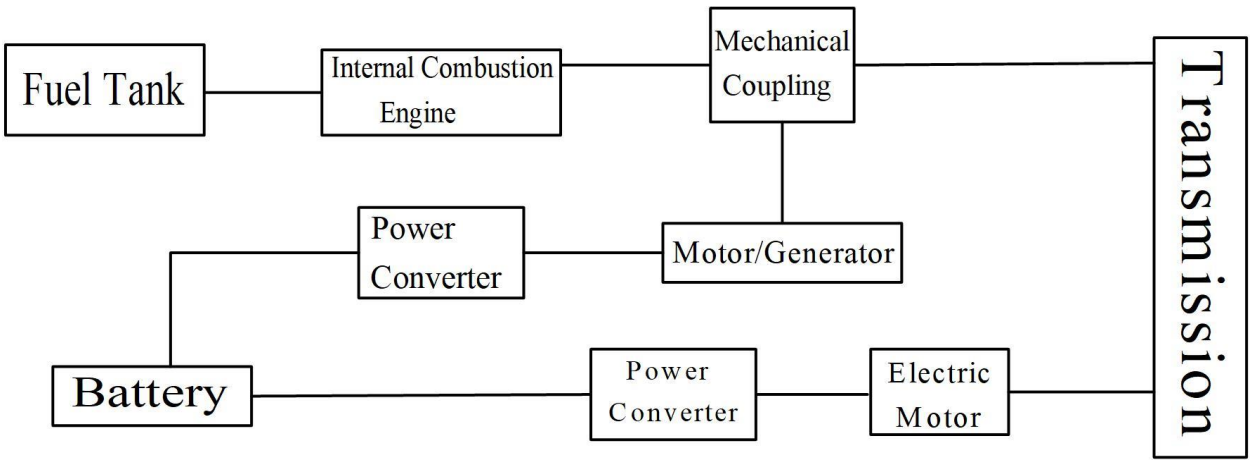

Fig. 1.5. Complex topology of hybrid electric vehicle [3]

With high power density, high energy efficiency over wide torque-speed range, permanent magnet (PM) machines provide a very competitive solution for HEVs/EVs tractions [5]-[8]. They have two types of rotor topologies: the interior permanent magnet (IPM) and the surface-mounted PM (SPM). The magnets are mounted on the rotor surface in the SPM topology while they are buried within the rotor body in the IPM topology [18]. Among various PM machine topologies,

Interior permanent magnet machines (IPM) which benefit from high torque and wide field weakening capability contributed by both PM torque and reluctance torque are particularly attractive [9],[10]. IPM machines are widely used in most of electric and hybrid electric vehicles such as Nissan Leaf and Toyota Prius due to many reasons among which their light magnet mass and their high torque production resulted from the saliency torque contribution.

However, unlike the applications in industrial traction, hybrid/electric vehicles bring highly demanding requirements on performances of electric traction machines particularly for permanent magnet machines, thus raising challenges in many aspects of developing an accurate and effective modeling.

1.4 Motivation of the Thesis

As discussed earlier in this chapter, an accurate powertrain modeling of HEVs/EVs is essential to study the vehicle performance under different operating scenarios and to enhance the vehicle performance.

Using the state of charge (SOC) of the battery as the only state variable to prevent any possible problems arising from having algebraic loops, the author of [33] has constructed his simulation model and his main focus was on developing a new battery model. However, in [34], the author investigates the hybrid electric vehicle performance from a different angle which was the fuel consumption. The author introduced a novel method by which it becomes possible to reduce the fuel consumption. As a different perspective in modeling improvement, the author in [35] developed a new method for controlling the permanent magnet synchronous motor based on a closed-loop current control regulation that is used in the full six-step mode as well as the space vector pulse width modulation. In [36], the author develops an average modeling for the hybrid electric vehicles, however, he was not able to test the power electronics converters dynamics and

transient response using such this modeling technique. Different modeling methodologies have been discussed in the literature and some researchers have applied some techniques like steady-state modeling, average modeling, and transient modeling. However, there was no much research about modeling Electric Vehicle incorporating with a transmission system that guarantees working for the optimum efficiency in a wide range of operation.

Also, comprising a transient modeling with a real time Hardware-in-the Loop has not been implemented in the literature due to the small simulation step time needed for it. However, thanks to the new technology, the Typhoon HIL, this became possible to be implemented.

Being aware of the challenges in the literature to come up with a new transient modeling of HEVs/EVs that consider all of the system dynamics including the mechanical parts and incorporating a two-speed transmission system to operate the motor around the optimum efficiency point and simultaneously being able to implement it using hardware-in-the-loop experimental verification, the author was motivated to conducted this work.

1.5 Scope and Objectives of the Thesis

Motivated by the need of the revolutionary changing traction packages' research and development, identified in the literature review in Chapter 2, to provide a complete and a comprehensive dynamic modelling approach for electrified vehicles' powertrain, the overall aim of this research is to develop, at system level, a versatile fully-detailed transient model for electrified vehicles' powertrain. This proposed system includes both electrical and mechanical subsystems with all corresponding parasitic elements and incorporated with a novel two-speed transmission gear system. Also, it can adopt the use of traditional silicon-based converters or SiC-based or state of the art GaN-based power electronic converters for modern passenger car applications. This will contribute to the technology development and powertrain modelling of

electrified vehicles by explicitly accounting for fast dynamics occurred within the powertrain electrical components. The methodology adopted here depends on providing a detailed mathematical dynamic model of each component of the electric powertrain which then integrated together to offer a platform to investigate the dynamics of the overall system in a way that can be easily tested and verified in terms of control robustness especially for high switching frequencies.

Unlike average dynamic models that approximate system dynamics by neglecting switching details, this model depends on mathematically representing each element by its partial differential equations to develop an equivalent circuit model for each component that accurately simulate its dynamic behavior. Verification of the proposed model using a new Controller Hardware in the Loop technology (Typhoon CHIL) is being used, for the first time in automotive applications, to verify the validity of the transient response of the proposed modeling in real-time. The CHIL is advantageous due to its ultra-high fidelity and very small step time suitable for capturing such transient behavior owing to its unique FPGA dependent design. The novelty of the model is its versatility and flexibility for being applied on a wide range of electrified vehicles that includes only one battery pack on one hand. It can also model futuristic power trains with new components.

Most importantly, it can be experimentally evaluated and verified without the need to build a whole physical test bench. Therefore, using this design technique to saves time, manpower and cost for industrial-based automotive applications.

Therefore, the main objectives can be summarized as follows:

1- The first objective is to determine the optimal sizing of different components of the powertrain. This can be performed by implementing a conventional steady-state modeling

approach. This gives also a deep understanding on how the energy flows within the powertrain in both forward and backward directions.

2- The second objective is to develop and integrate all the powertrain components being simulated on PSIM platform based on their fully-detailed transient mathematical modeling in order to investigate the dynamics of any electrified vehicle and detect any anomalies especially those due to high-frequency switching of power electronic converters. The simulation results are then verified and results are compared with real results of two benchmark electrified cars that are being used as two separate case studies for verification and validation of the proposed model. Those two cars are 2016 Second Generation GM Chevrolet Volt Plug-in Hybrid Electric Vehicle (PHEV) and 2012 Nissan Leaf Battery Electric Vehicle (BEV).

3- The third objective is to incorporate a novel two-speed transmission gear system (inMotive inGear) developed by inMotive company in Toronto. This transmission system is to be integrated with its dynamic modeling into the entire model of the powertrain in order to obtain the optimal gear ratio based on the first and second gear acceleration equations that results in improving the efficiency of the overall system by shifting the operating region of the motor to be always working within the best efficiency region and provides a seamless transition shift between gears without having a blind spot operation.

4- The fourth objective is to substitute the conventional silicon based converters by SiC-based converters and GaN-based converters; one at a time. The three topologies are to be compared in terms of their impacts on improving the car mileage and the powertrain overall efficiency. Also, for studying the effects on applying high switching frequencies on the gain and system disturbance and their impacts on sizing magnetic components.

5- The fifth objective is to verify the robustness of the control algorithm and the whole fully-detailed transient model by using a CHIL technology. The hardware in the loop technique uses the same real controller used in hardware implementation and builds its own power circuit model in the Typhoon environment. Furthermore, the CHIL provides a virtual vehicle technique to emulate the same environment exactly as the physical hardware test bench.

1.6 Contributions

To the knowledge of the author, the main contribution of this thesis for engineers and researchers in the efforts of addressing the challenges on the modeling of HEVs/EVs can be illustrated as follows:

[1] Developing steady-state and transient models for an HEV/EV powertrain

The first contribution is to construct a versatile steady state power flow modeling approach for HEVs/EVs powertrain. This model allows for properly sizing main components such as battery, DC-DC converter, DC-AC converter, and Electric motor. However, the power flow model gives a good understanding of the operation of the drive-train but it does not simulate transients of the system. In order to have a better understanding of the powertrain and also to develop a hardware-in-loop setup for the powertrain, a transient model for the transmission system powertrain has been established on PSIM platform. This model simulates the vehicle powertrain including power-electronic converters with a high level of details and is suitable for PSIM based real-time simulators such as Typhoon HIL.

This part of the thesis is presented in 2018 IEEE Applied Power Electronics Conference and Exposition (APEC), in a paper titled " A novel platform for power train model of electric cars with experimental

validation using real-time hardware in-the-loop (HIL): A case study of GM Chevrolet Volt 2nd generation,", San Antonio, TX, 2018, pp. 3510-3516.

Also, Part of this section of the thesis is published in IEEE Transactions on Transportation Electrification, in a journal titled: "Hybrid Fuel Cell/Battery Rail Car: A Feasibility Study," vol. 2, no. 4, pp. 493-503, Dec. 2016.

[2] Developing a HIL system using transient modeling approach

The transient model was used to develop a hardware-in-loop setup for the first time. The HIL system developed in this research is based on a transient model for the powertrain. This setup uses Typhoon HIL simulator to run the simulation in real-time. The transient model is selected due to its accuracy because the available real-time simulator is capable for simulating the transient model in real-time. Also, the effect of fast switching transients can be studied using the detailed model for the power electronic converters. This setup can be used to study the behavior of the battery in the vehicle. The chemical nature of battery makes it difficult to derive a complete model for the battery. Effect of temperature, especially sub-zero temperatures, and also aging of the battery cannot be easily modeled mathematically. Therefore, it is common practice to use real batteries to study the battery behavior under different conditions. The hardware-in-loop setup developed in this research can be used to study the behavior of real battery under different driving conditions.

Part of this section of the thesis is presented in IEEE Transactions on Power Electronics, in a journal titled " A Novel Platform for Power Train Modeling of Electric Cars with Experimental Validation Using Real-Time Hardware in-the-Loop (HIL): A Case Study of GM Chevrolet Volt 2nd Generation,", vol. PP, no. 99, pp. 1-1.

[3] Incorporating a two-transmission system to improve the motor efficiency

A two-speed inMotive inGear transmission system has been integrated with the proposed modeling. It has been investigated towards obtaining the optimum gear ratio on its performance. Therefore, the influences of single transmission and two-speed transmission have been compared. The results have shown that the two-speed transmission gives better performance in both dynamic and economic performance. Also, the two-speed transmission extends the vehicle's range. Additionally, the two-speed transmission increases the efficiency of the motor compared with the single-speed transmission.

This part of the thesis is presented in 2017 IEEE Energy Conversion Congress and Exposition (ECCE), in a paper titled " Optimal Gear Ratios Selection for a Nissan Leaf: A Case Study of InGear Transmission System," Cincinnati, OH, 2017, pp. 2079-2085.

[4] Wide Band Gap (WBG) devices implementation

The system has been investigated through replacing the conventional converter (Si based converter) with the new fast response wide band gap semiconductor switches [Gallium Nitride GaN and Silicon Carbide (SiC)]. The efficiency has been improved by 2.2% in case of a GaN HEMT based inverter whilst it has been improved by 2% in SiC Trench based inverter. It can be also observed that there is a constant efficiency margin ranges from 0.6%-0.7% for all tested cases under normal load. At higher frequencies, the merits of using WBG devices become obvious in terms of less passive elements and size reduction of magnetic elements and in turn leads to power density improvement and car mileage extension. As a result of operating at higher frequencies, the converter weight is reduced by 30% in comparison with the conventional converters.

This part of the thesis is published in Canadian Journal of Electrical and Computer Engineering, in a journal titled: "Wide Bandgap Devices in Electric Vehicle Converters: A Performance Survey," vol. 41, no. 1, pp. 45-54, winter 2018.

Also, Part of this section of the thesis is presented in 2018 20th European Conference on Power Electronics and Applications (EPE'18 ECCE Europe) in a paper titled "Performance of Wide Band Gap Devices in Electric Vehicles Converters: A Case Study Evaluation," Riga, Latvia, 2018, pp. P.1-P.9.

Further, Part of this section of the thesis is presented in 2016 IEEE Transportation Electrification Conference and Expo, Asia-Pacific (ITEC Asia-Pacific) in a paper titled " SiC devices performance overview in EV DC/DC converter: A case study in a Nissan Leaf,", Busan, 2016, pp. 214-219.

[5] Electric machines based induction motors selection for HEV/EV

The performance of the three topologies of induction motor, SFIM, DFIM and CDFIM is compared. For a fair comparison, the inverter size and the specifications of the motors are the same. Each motor is accurately simulated and the results obtained from the three simulations are quantified and analyzed. The CDFIM allows for easier flux detection especially at low and zero speeds, however, his this quite difficult in SFIM. Moreover, the CDFIM is a fault tolerant configuration due to having two inverters so it is easy to work as a SFIM in case of any failure that may happen to any inverter. Furthermore, the DFIM and the CDFIM are capable of achieving wider speed range and higher torque and power density. We can conclude that each motor has some advantages and some other drawbacks and in some applications we may sacrifice the machine weight in exchange for better efficiency and better power consumption.

Several parts of the work of the thesis have been reported by the author during the course of his doctoral study in international IEEE conferences and journals. The publications are listed as follows:

Journal papers:

J1. **A. Abdelrahman**, K. Algarny and M. Youssef, "A Novel Platform for Power Train Modeling of Electric Cars with Experimental Validation Using Real-Time Hardware in-the-Loop (HIL): A Case Study of GM Chevrolet Volt 2nd Generation," in *IEEE Transactions on Power Electronics*, vol. PP, no. 99, pp. 1-1.

J2. **A. S. Abdelrahman**, J. Sayeed and M. Z. Youssef, "Hyperloop Transportation System: Analysis, Design, Control, and Implementation," in *IEEE Transactions on Industrial Electronics*, vol. PP, no. 99, pp. 1-1.

J3. **A. S. Abdelrahman**, Y. Attia, K. Woronowicz and M. Z. Youssef, "Hybrid Fuel Cell/Battery Rail Car: A Feasibility Study," in IEEE Transactions on Transportation Electrification, vol. 2, no. 4, pp. 493-503, Dec. 2016.

J4. **A. S. Abdelrahman**, Z. Erdem, Y. Attia and M. Z. Youssef, "Wide Bandgap Devices in Electric Vehicle Converters: A Performance Survey," in *Canadian Journal of Electrical and Computer Engineering*, vol. 41, no. 1, pp. 45-54, winter 2018.

Conference papers:

C1. **A. Abdelrahman**, Z. Erdem, Y. Attia and M. Youssef, "Performance of Wide Band Gap Devices in Electric Vehicles Converters: A Case Study Evaluation," *2018 20th European Conference on Power Electronics and Applications (EPE'18 ECCE Europe)*, Riga, Latvia, 2018, pp. P.1-P.9.

C2. Jawwad Sayeed, **Ahmed Abdelrahman** and Mohamed Youssef, “Active Levitation and Propulsion System: Design, Analysis, Control and Prototyping” accepted for publication in 2018 IEEE Energy Conversion Congress and Exposition (ECCE), Portland, Oregon, USA.

C3. K. Algarny, **A. S. Abdelrahman** and M. Youssef, "A novel platform for power train model of electric cars with experimental validation using real-time hardware in-the-loop

(HIL): A case study of GM Chevrolet Volt 2nd generation," *2018 IEEE Applied Power Electronics Conference and Exposition (APEC)*, San Antonio, TX, 2018, pp. 3510-3516.

C4. **A. S. Abdelrahman**, K. S. Algarny and M. Z. Youssef, "Optimal Gear Ratios Selection for a Nissan Leaf: A Case Study of InGear Transmission System," 2017 IEEE Energy Conversion Congress and Exposition (ECCE), Cincinnati, OH, 2017, pp. 2079-2085.

C5. Jordan Henry, **Ahmed Abdelrahman**, and Mohamed Youssef "Modeling and Simulation of the 2016 Chevy Volt in Dual PMSM EV Mode" in Smart Energy Grid Engineering (SEGE), 2015 IEEE International Conference on , vol., no., pp.1-8, 14-17 Aug. 2017.

C6. Y. Attia, **A. Abdelrahman**, M. Hamouda and M. Youssef, "SiC devices performance overview in EV DC/DC converter: A case study in a Nissan Leaf," 2016 IEEE Transportation Electrification Conference and Expo, Asia-Pacific (ITEC Asia-Pacific), Busan, 2016, pp. 214-219.

Under Review

U1 **Ahmed S. Abdelrahman**, Khalil Algarny and Mohamed Z. Youssef "A Survey Study of Performance and Control of Singly-Fed, Doubly-Fed and Cascaded Doubly-Fed Induction Machines for EV/HEV Applications", the Journal of Emerging and Selected Topics in Power Electronics (Under review)

1.7 Thesis Outlines

This thesis is organized as follows:

Chapter 1 Presents an overview of the major classifications of HEV/EVs in addition to research objectives and thesis outlines.

Chapter 2 Provides a detailed literature review regarding different motor types, different transmissions, and different modelling methods used in Electric vehicles

Chapter 3 Explains and describes the mathematical modeling in details and provides the necessary equation for each module.

Chapter 4 Shows the simulation results obtained from PSIM software and provides the experimental verification real-time results and compare it with the simulation results through the Hardware-in the loop (Typhoon HIL) new technology.

Chapter 5 Introduces a unique quantified study about using low losses fast switching wide band gap (WBG) devices, i.e. Gallium Nitride (GaN) and Silicon Carbide (SiC), over traditional Silicon (Si) devices in the switching of DC/DC converters; focusing on electric vehicles' (EV) machine drive. Also, it provides a comprehensive comparison between different induction motors to determine the optimum motor for HEV/EV.

Chapter 6 Concludes the topic presented in this thesis and the areas for future research work. Lastly reference list is added.

Chapter 2. Literature Review

2.1 Introduction

The BLDC permanent magnet synchronous machines are now a major element of the electric vehicle propulsion system due to their high efficiency along with high torque density [37]. They have two types of rotor topologies: the interior permanent magnet (IPM) and the surface-mounted PM (SPM). The magnets are mounted on the rotor surface in the SPM topology while they are buried within the rotor body in the IPM topology [38]. IPM machines are widely used in most of electric and hybrid electric vehicles such as Nissan Leaf and Toyota Prius due to many reasons among which their light magnet mass and their high torque production resulted from the saliency torque contribution. The electric vehicle propulsion system shown in Figure 1.7 has basic components that can be classified to storage devices which can be batteries or ultra/super capacitors; power electronics elements that consist of DC/DC converters and inverter; electric motor; gear box and control system. The DC/DC converter is necessary to be used right after the energy source to control the power flow at the DC bus. The traction motor and the power converters ratings are determined by the magnitude of DC-link voltage.

When it comes to modelling the propulsion system of electric vehicles, we have to consider different modelling cases. If we need to study the steady-state performance of electric vehicles, then the proper modelling will be based on the steady-state modelling which is relatively simple and inexpensive in terms of the computational tools used for it. Also, this kind of modelling allows for a fast simulation due to the required small time step. However, the steady state modelling can be only useful when used in determining the size of major components and the selection of the

control strategy. On the other hand, the transient model can be highly beneficial when studying the dynamics of the electric vehicle and the fast switching of the power electronics devices. One of the major benefits of transient models they can be used in real time hardware in-the-loop (HIL) simulators which will be the main focus of this research. In [39], the main concentration was on the propulsion system, however, it neglected any change that may occur in the battery dynamics.

In [34], the performance of the EV focused mainly on the battery model and the simulation model uses only the battery state of charge (SOC) as the only state variable to avoid any algebraic loop problems. In [34], the performance based on fuel consumption was investigated and a new method has been proposed to reduce it. In [40], a novel method for PMSM control algorithm with a closed-loop current control regulation that can be used in both the SV-PWM and full six-step mode was demonstrated. To examine the dynamical behaviour of all the subsystems of electric vehicles, the transient modelling is a must as the steady-state modelling is not suitable for the fast dynamics of the vehicle. Most of studies that used hardware in-the-loop high levels simulators to study the performance of electric vehicles are not suitable for hardware in-the-loop simulations.

2.2 Approaches of Dynamical Powertrain Modeling

In order to design a robust control system and to implement the state estimation technique, a profound powertrain dynamical model of the vehicle. A solid understanding of the system responses can be provided through a detailed and accurate mathematical modelling which paves the way for analysing the system response in terms of different control inputs, driver's commands and various road disturbances. The mathematical modeling of the powertrain is derived from the basic equations of vehicle dynamics using many different approaches such as the Hamilton principle, the d'Alembert-Lagrange principle, Euler-Lagrange equations, the Newtonian method and graphical techniques [41].

The first method of modeling depends mainly on the modular technique which was first introduced by [42]. In this approach, the main components such as a diesel engine, a torque converter, a clutch, shafts, etc. were programmed using EASY 5 simulation language [42]. However, [43] showed that the same approach has been utilized but adopted MATLAB/SIMULINK as the simulation software. Both of them avoided the existence of algebraic loops, which in turn slow down the simulation, and emphasize mainly on the cause and effect relationship between input and output variables in modular modeling. Therefore, the powertrain model can be established by connecting theses independent modules. This approach is used later in improving the dynamical model of the powertrains especially the ones associated with the automated manual transmissions (AMTs) [44], [45] and for developing a detailed dynamical model for internal combustion engine vehicle with a dual-clutch transmission [46], [41]. Vectorial dynamics approach or also sometimes is being referred to as the Newtonian approach is often used with modular approach as it depends on the free-body diagram of multibody systems where the applied forces and torques can be graphically visualized. Newton-Euler equations are employed to calculate the accelerations of the isolated bodies for a given torque or force.

The Newtonian approach is found to be inappropriate when being used with multi-body systems with multiple constraints due to the complexity appears in determining the constraint torques or forces [41]. However, other approaches such as Euler-Lagrange equations, the Hamilton principle, and the d'Alembert Lagrange principle can be used to solve the multiple constraint systems. These methods are typically used when dealing with the overall system dynamics not with the individual components dynamics. Moreover, they best fit with the powertrain systems that utilize planetary gear-based transmissions whilst the transmission overall dynamics are sought instead of the intermediate gears dynamics [41].

Graphical methods such as bond-graph and lever analogy can be also used for developing the dynamical models of powertrains [41]. The main feature of this approach is its capability to examine the power flow in different fields. This method is also used to improve the control systems design in transient and steady state dynamical methods of hybrid electric vehicle powertrains [47]. Furthermore, it was used to optimize the simulation and design control procedures for the dynamical model of powertrain of an internal combustion engine vehicle equipped with automated transmission [48], [49]. In [50], the lever analogy method is adopted. This method in particular is very beneficial especially in the mathematical modeling of hybrid electric vehicle powertrains for which a planetary gear sets are being exploited to connect different power sources such as electric motors, internal combustion engines...etc.

2.3 Transmission Systems Used in Electric Vehicles

A transmission system is used mainly to transfer the power from the power source (internal combustion engine, electric motor, or both) to the wheels in different combinations of torque and speed. The whole system efficiency is greatly affected by the transmission as well as the dynamic performance and drivability [51]. We can classify the main types of the vehicle transmissions: 1) Manual Transmission (MT) 2) Automated Manual Transmission (AMT) 3) Automatic Transmission (AT) 4) Dual Clutch Transmission (DCT) 5) Continuously Variable Transmission (CVT).

We can classify the manual transmissions into two main types 1) single-stage countershaft 2) two-stage countershaft. In this type, the driver has the freedom to select the appropriate gear shift based on the speed and torque required. The input and output shafts of the transmission are non-coaxial in single-stage countershaft and coaxial in the two-stage countershaft [Naunheimer et al

2010]. A synchronizer is used for manual transmissions to perform the gear shifts by matching the speed of the gears and driveline by using the friction surfaces between the gear cone and the synchro ring of the mechanism [52], [53], and [54].

The lack of automatically controlled gear shifts in MTs is addressed in automated manual transmissions (AMTs) in order to improve drivability, efficiency, and lifetime of the system. The mechanical layouts of AMTs are identical with those of MTs but instead of the driver, external actuators execute the gear selection, gear shift, and vehicle launch [52], [53], and [54]. These actuators are typically controlled together with the traction unit in an integrated gear shift algorithm [44], [46], and [41]. Dual clutch transmissions (DCTs), regarding the mechanical design, were almost developed almost 75 years ago with the intention of providing seamless gear shifts. Porsche and Audi retrofitted this type of transmission to their racing cars. However, due to intricacies of controlling gear changes, they could not be commercialized until 2003 [55]. The mechanism of DCTs is made of two sub-gearboxes wherein the structure of each sub-gearbox is equivalent to that of the manual transmission. One of the sub-gearboxes provides the odd gears and the other one the even gears. Each sub-gearbox is coupled with a separated clutch to the traction unit and the output shaft of each sub-gearbox is connected to the driveline [56], [55]. Fig. 2.1 conceptually illustrates the mechanical layout of DCTs.

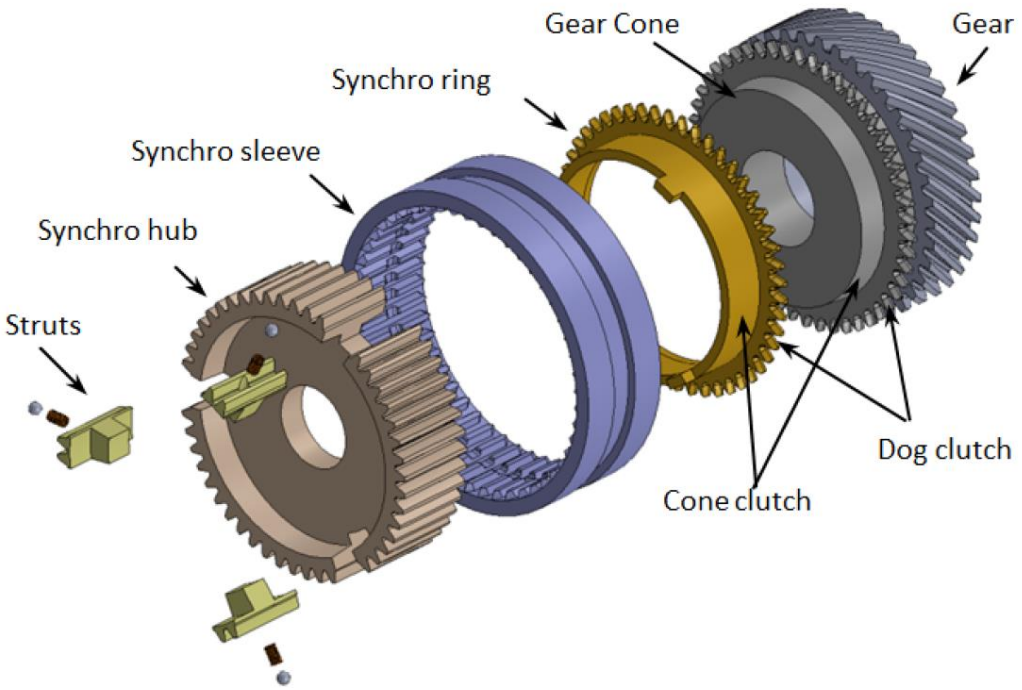

Fig. 2.1. Dual cutch transmission layout [54]

Continuously variable transmissions (CVTs) provide continuous and step less gear ratios. The principle typically used by CVTs is to keep the traction unit in the most efficient point while changing the gear ratio in order to obtain different combinations of the torque and speed [55]. There are many types of CVTs with various characteristics such as belt, chain, toroidal, and spherical [57], [58], [59], among which, chain and belt are the most common types in automotive applications. The most important mechanism in chain/belt CVTs is a variable diameter pulley (VDP). These variable diameter pulleys change the diameter of the belt/chain on the drive and driven sides by adjusting the gap between tapered disks which consequently changes the gear ratio of the transmission [55].

Automatic transmissions (ATs) typically consist of multi-stage planetary gear sets, a torque converter, multi-plate clutches, and band brakes. Engaging and disengaging clutches and brakes provide different gear ratios. The torque converter is located between the traction unit and the

transmission in order to improve drivability. Moreover, the torque converter releases the mechanical coupling between the traction unit and the transmission and allows the traction system to rotate independently from the transmission while transferring torque via a hydraulic coupling.

Similar to DCTs, planetary-gear-based ATs have the ability to eliminate output torque interruptions during gear shift operations [55], [60], [61], [62], [63]. The vehicle driveline, which transmits the transmission output power to the wheels, typically encompasses a final drive and differential assembly, half shafts, and wheels. The differential transfers the torque of the final drive to the wheels via the half shafts while providing independent rotation of the wheels. Therefore, the differential provides required speeds of the wheels for the vehicle maneuvers [64], [65].

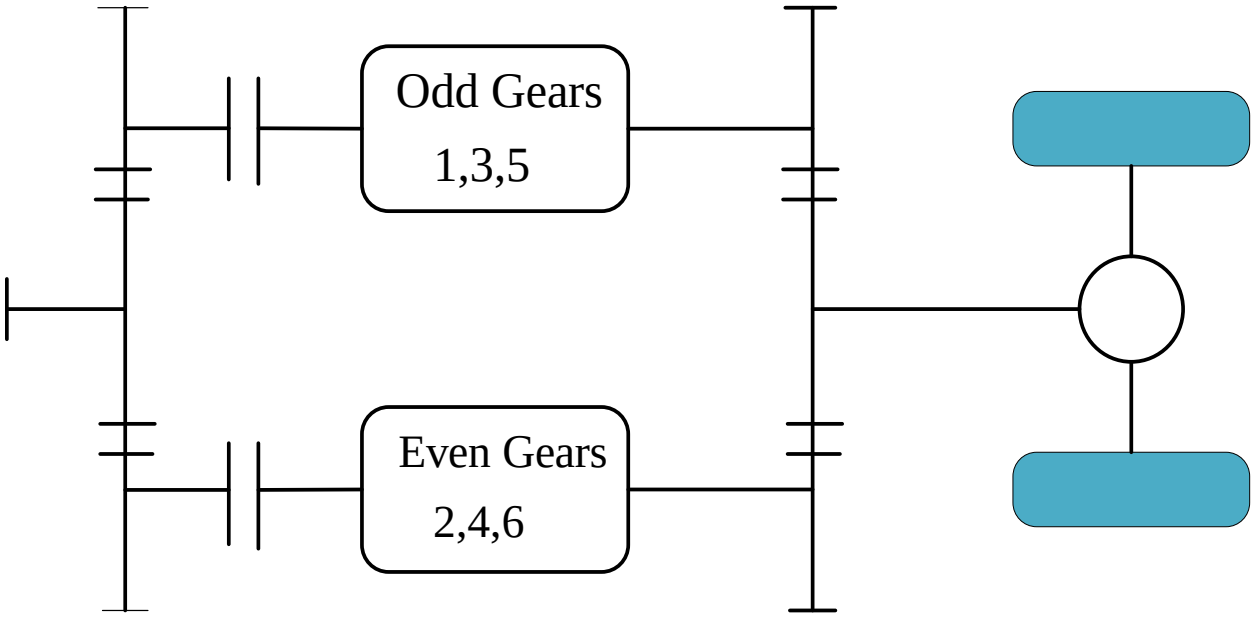

Fig. 2.2. Multi-speed dual clutch transmission schematic diagram [36]

Automated manual transmissions (AMTs) are of great interest for EVs because of their lower weight and higher efficiency in comparison with other types of transmissions such as ATs, CVTs, and DCTs [44], [46], [66]. Specifically, clutchless automated manual transmissions (CLAMTs) wherein the clutch is eliminated from the powertrain to further improve efficiency. Although these

transmissions are highly efficient, the torque interruption during the gear shift operation, which comes from the disengagement and re-engagement of the transmission synchronizer reduces passenger comfort (i.e., drivability) and the lifetime of the synchronizers. In fact, this type of transmissions suffers from the fundamental trade-off between efficiency and drivability [67], [68]. In contrast to AMTs, DCTs have the special feature of eliminating the output torque interruption during gear shifts by controlling the pressure of the clutches together with the torque of traction unit. However, they have higher weight and lower efficiency, particularly DCTs with wet clutches [55], [46], [69], [70].

The chain and belt CVTs are the most prevailing types of continuously variable transmissions adopted in the automotive industry. In chain/belt CVTs, the tension of the chain/belt plays a crucial role in the performance of the transmission. Excessive tension reduces the efficiency of the system and in- creases stress on the transmission. However, the tension should be adequate to avoid slippage [55]. In addition to these intricacies, the set of efficient operating points of electric motors is rich enough, and thus, the multiplicity of gear ratios or a continuously variable transmission may not be necessary for EVs [71].

Similar to DCTs, planetary-gear-based ATs have the ability to eliminate the output torque interruption during the gear shift operation. However, due to the existence of torque converters and hydraulic systems in ATs, they have lower efficiency in comparison with other types of transmissions, and they are not of great interest for EVs. Furthermore, the provided power in the output of the transmission is decreased due to the power loss inside the torque converter when it is not completely engaged [55], [60], [61].

There is no substantial literature supporting the application of manual transmissions (MTs) in EVs. This is due to the fact that in MTs the driver is the sole controller of the transmission system

that performs the gear selection and gear shifts. Therefore, efficiency and drivability of the vehicle highly depend on the driver's skills. Consequently, there remains little opportunity for implementation of optimal control algorithms related to the transmission control. Hence, efficiency, drivability, and lifetime improvements could not be addressed systematically [72], [73], [74], [75]. In addition to the above-mentioned systems, there has been a considerable re- search effort aimed at introducing transmissions specifically designed for EVs by considering the characteristics of electric motors and their advantages in comparison to ICEs. A novel two-speed lay shaft type transmission for EVs is proposed in [76] in which the power is transferred via a one-way clutch in the first gear ratio and by a frictional clutch in the second one. A similar concept is adopted by [68] in order to propose a novel AMT transmission for EVs called inverse automated manual transmission (I-AMT). In this system, the dry clutch is placed at the rear of the transmission in order to keep the tractive torque and eliminate the torque hole by means of a slipping sleeve. Further, a two-speed planetary gear-based transmission for EVs is patented by [77] in which the electric motor is connected to the sun gear of the first planetary gear set whose ring gear is grounded. The carrier of the first planetary gear set transfers the power to the trans- mission output shaft via either the sun or ring gears of the second planetary gear set depending on the state of the clutches. Given the fact that ICEs cannot operate below a certain speed and controlling their speed is not an easy task, the presence of frictional and hydraulic couplings is inevitable for vehicle launching and gear shifting. This, however, is not the case for EVs as electric motors are speed controllable in terms of speed and torque in a wide range of operating. Therefore, the presence of clutches and torque converters is not necessary for the transmission designed for EVs [71].

2.4 Electric Motors for HEV/EV Applications

Although there are many different variants of fully electric vehicle layouts, or even hybrid electric vehicles, the key component in each is the electric motor. Electric motor torque/power characteristics differ from an internal combustion engine, the main difference being that the generic electric motor can provide maximum torque from zero speed. The typical torque curve of an electric motor, as shown in Fig. 2.3, is made up of a constant torque range from zero to base speed [78], where the torque is electronically limited by the controller as the controller has a current limit. Theoretically the torque can be infinite at zero speed due to no back EMF (Electro-Magnetic Field) being present. The constant torque region is followed by a constant power region, in first approximation, where the available torque reduces (due to the increasing back EMF and by reducing the field flux of the motor) as the motor speed increases up to the maximum speed. Although in reality the torque reduces at a faster rate across the motors speed range reducing the power below a constant power.

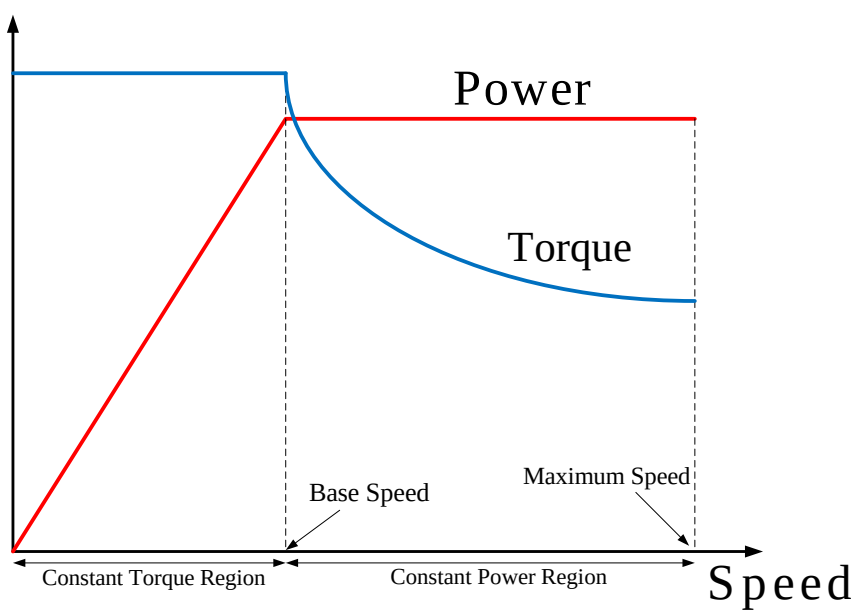

Fig. 2.3. Torque/Power – speed characteristics of a motor drive. [78]

The main characteristics of an electric drive for a motor vehicle, as described in [79] should be a high torque density and power density, very wide speed range, high efficiency over wide torque and speed ranges, wide constant power operating capability, high reliability, robustness, low torque ripples and finally a low acoustic noise. Paper [80] discusses the main options for the electric motor in an electric powertrain which fall into two main categories, the brushed and the brushless. These two main groups of electric motors can be further categorized by subgroups as shown in Fig. 2.4.

The main designs of motor being considered for electric powertrains are the direct current (DC) motor, the induction motor (IM), the permanent magnet (PM) synchronous motor (SM), and the switched reluctance motor (SRM).

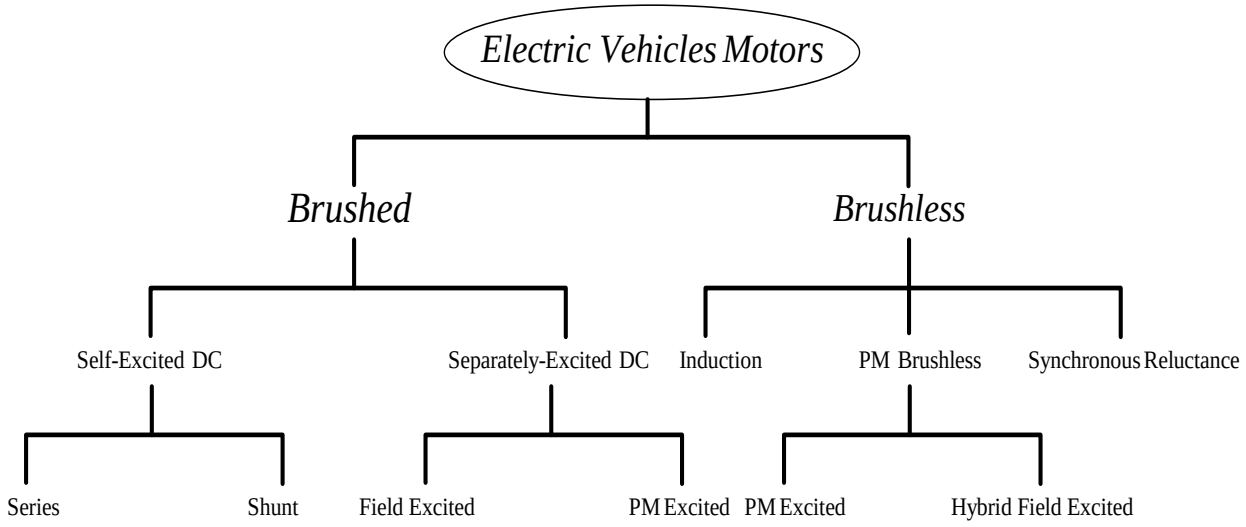

Fig. 2.4. Generic classification of EV/HEV electric motors [79]

This brief overview of electric motors has been included as it is relevant to the subject, but due to transmissions being the main focus of this thesis no further detail will be included. The PMSM was predominantly adopted for the electric powertrains used in research covered in the later chapters.

2.4.1 Induction Machines in EV/HEV Applications

After many years of the dominance of permanent magnet synchronous machines, currently, inductions motors are making a comeback in the electric vehicle (EV) industry [81], [82]. The selection process of a certain type of motor for using in EV applications depends on many factors such as compact size, low cost in both manufacturing and maintenance, high efficiency for a wide range of speeds, high torque density, high power density, reliability and robustness [83], [84].

Using induction motors in EV/HEV applications is a way to reduce the demand on rare-earth magnets which, in comparison with the iron used in IMs, are very expensive and their flux is so strong that make it difficult to be diminished in the flux-weakening region [85]. Hence, as a way of replacing the rare-earth magnets and cost saving, many topologies of induction motors are being adopted nowadays. The most common topologies are the conventional cage singly-fed IM, the doubly-fed induction motor, and the cascaded doubly fed induction motor [86], [87]. The main disadvantage of the SFIM is its low torque density and low efficiency due to the high losses appears in the stator as well as the losses in the slip ring and carbon brushes. However, its field oriented control (FOC) is quite easy to be implemented [88].

The SFIM is quite different from DFIM especially in high speed operation. For a DFIM, working in high speeds beyond the synchronous speed (i.e. in the super-synchronous mode of operation), the DFIM is capable of keeping the same operating frequency for the stator winding, however, boosting the rotor winding frequency [89]. Fig. 2.6 shows the DFIM drive system that has two inverters on the rotor and stator sides. On the other hand, a SFIM operating at high speeds above the synchronous speed will force the IM operation to go in a flux weakening region which dictates the I_d components to decrease its value to weaken the air-gap flux [90]. Increasing the frequency will in turn decrease the I_d and increase the total losses and decrease the torque

drastically. Doubling the torque-speed capability in case of using DFIM has no effect on the stator and rotor copper losses and it will remain constant as of the SFIM. The only difference will be in the rotor core losses which will be higher than the conventional SFIM. However, the advantages of doubling the torque-speed capability outweigh the increase in losses since increasing the energy efficiency due to the wide range of speed will enhance the fuel consumption and consequently increase the EV mileage. The CDFIM, as shown in Fig. 2.7, eliminates the use of carbon brushes and slip rings. Therefore, the maintenance cost will be reduced and the energy efficiency will be increased with a higher torque/speed capability.

In [89], a comparison study has been performed between SFIM and DFIM. However, it concentrated mainly on the control algorithms of the two machines rather than the whole performance.

2.4.1.1 Torque-Speed Capabilities

In doubly-fed induction motor, the torque remains the same, however, the speed is doubled since it is being fed through the rotor and the stator windings. On the other hand, the SFIM torque is limited by the allowable current fed into the windings without excessive heat [83], [91]. Moreover, the speed of the SFIM is constrained by the available voltage supply. As mentioned earlier, the CDFIM has two main methods of control, named single-electrical port (SEP) and double-electrical port (DEP). In DEP control scheme, the torque and power speed characteristics are the same as the SFIM since both the power winding and the control winding contribute in the resultant torque/power components. As the SFIM is SEP, it is better and more realistic to compare the SFIM to the DFIM and CDFIM with a SEP control scheme. Hence, in SEP CDFIM, it is worth mentioning that, the overall mechanical power can be doubled if the power winding machine and the control winding machine has the same frequency. However, this cannot be achieved in reality

because the torque will decrease drastically with the decline in the slip frequency. So it can be concluded that the CDFIM can achieve 80 % more in the torque/speed capabilities of the SFIM. The torque/power speed characteristics are summarized in Fig. 2.8. The three motors that have the same HP rating are compared under the same loading and the performance of each motor is investigated in details.

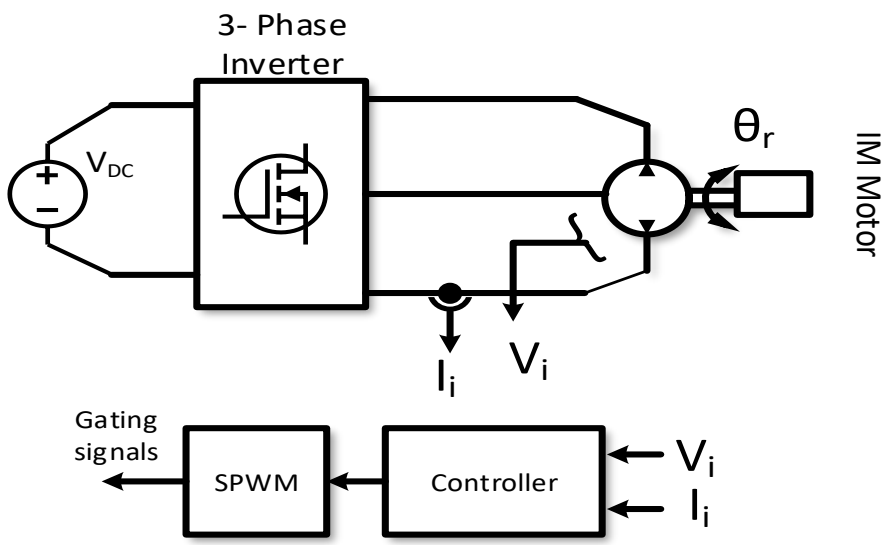

Fig. 2.5. Drive system of singly fed induction motor used in EV/HEV applications [86]

2.4.1.2 Modelling and Control Implementation

The DFIM unlike IM allows for controlling four variables the stator current direct and quadrature axes and the rotor current direct and quadrature currents. Thus, we can achieve many control targets such as controlling the torque, maximum torque per ampere (MPTA) and the air gap flux. A modified DTC for the IM and DFIM is adopted in this study as depicted in Fig. 2.9 and Fig. 2.10 respectively. However, in the CDFIM, a non-standard FOC is performed; the control is performed only from the stator side a the rotor side of both machines is connected together in a reverse manner. The control of CDFIM can be performed using a single-electrical port (SEP) that uses the input current to the inverter or dual-electrical port (DEP) that uses both the input current

and voltage. However, the DEP is quite complex in comparison with the SEP as shown in Fig. 2.11. The main advantage of the CDFIM is that in case of failure of any of the two inverters, the two DFIMs can be operated as a cascaded SFIM by short-circuiting the stator winding.

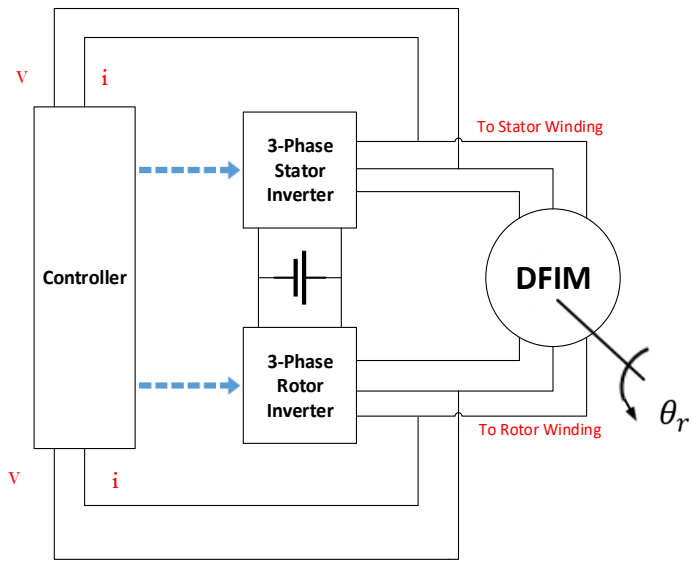

Fig. 2.6. Drive system of doubly-fed induction motor used in EV/HEV applications [86]

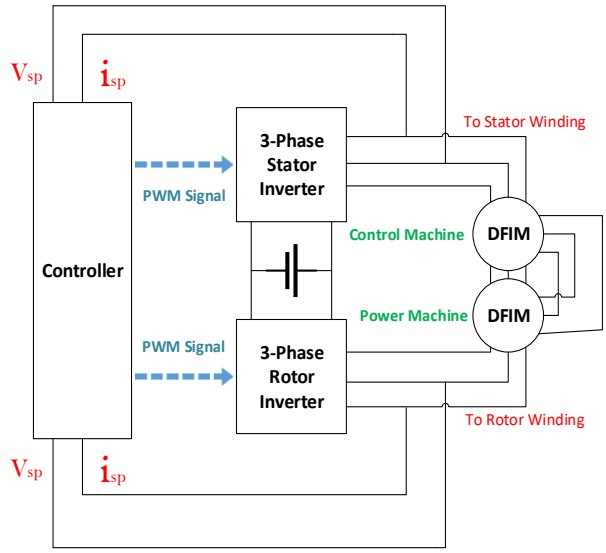

Fig. 2.7. Drive system of cascaded doubly fed induction motor used in EV/HEV applications [86]

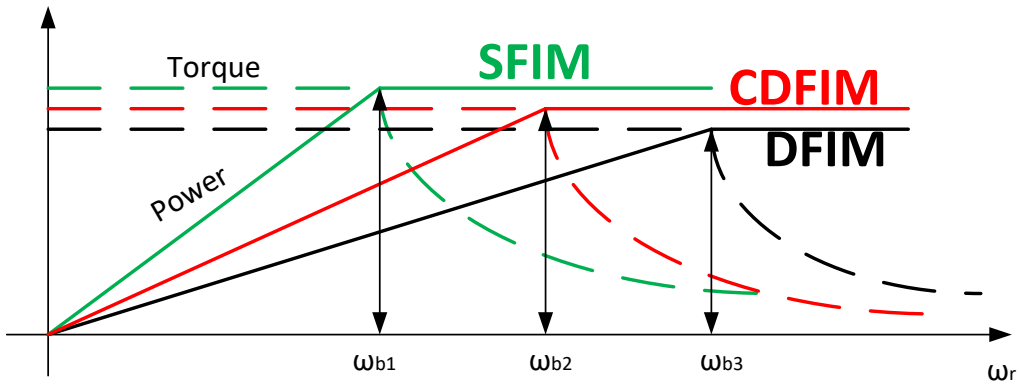

Fig. 2.8. Torque/Power - speed characteristics of the three induction motors [86]

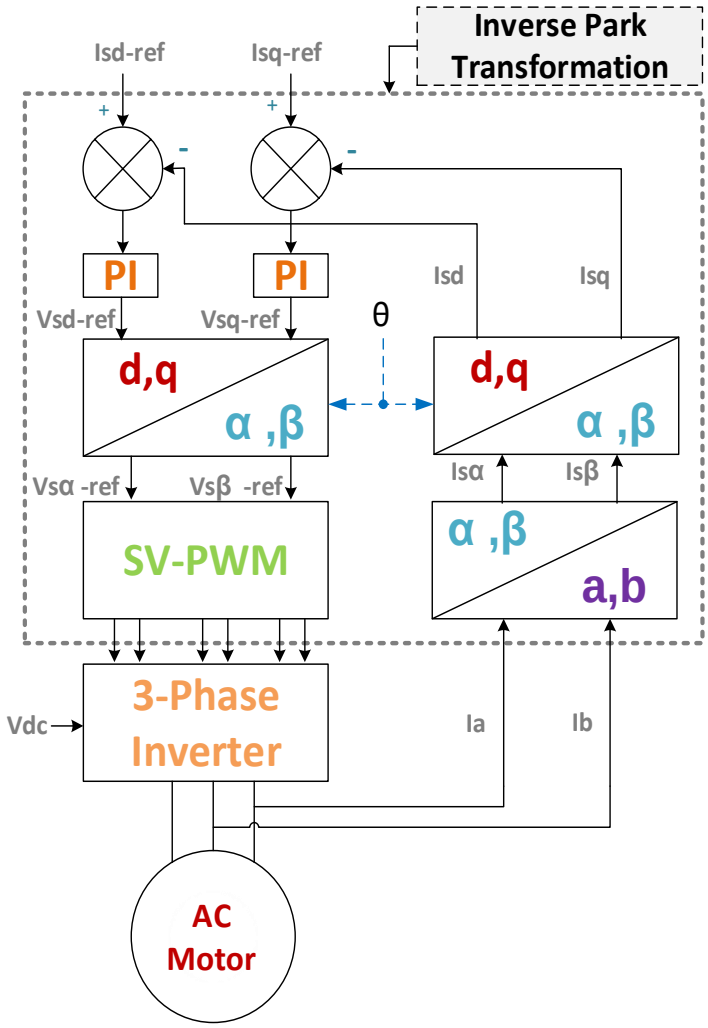

Fig. 2.9. Control scheme of the singly fed induction motor [87]

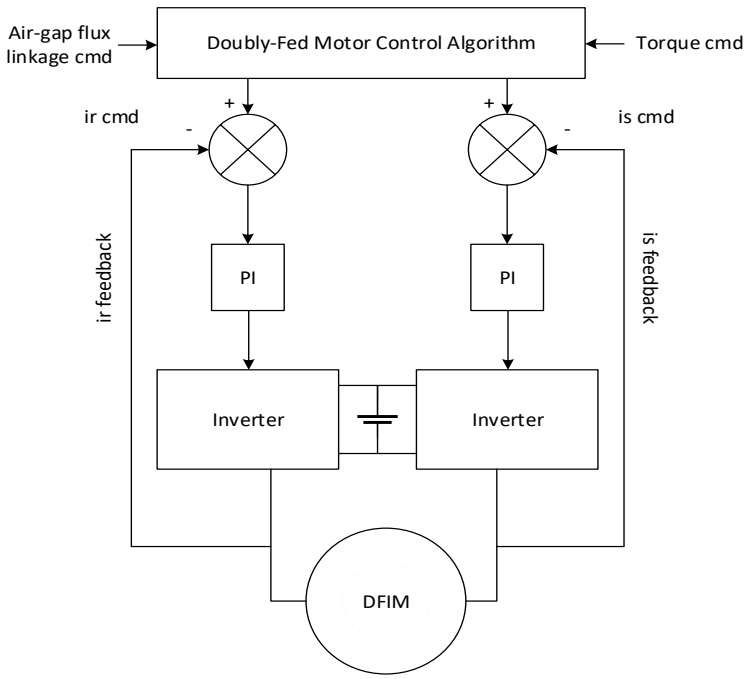

Fig. 2.10. Control scheme of the doubly fed induction motor [87]

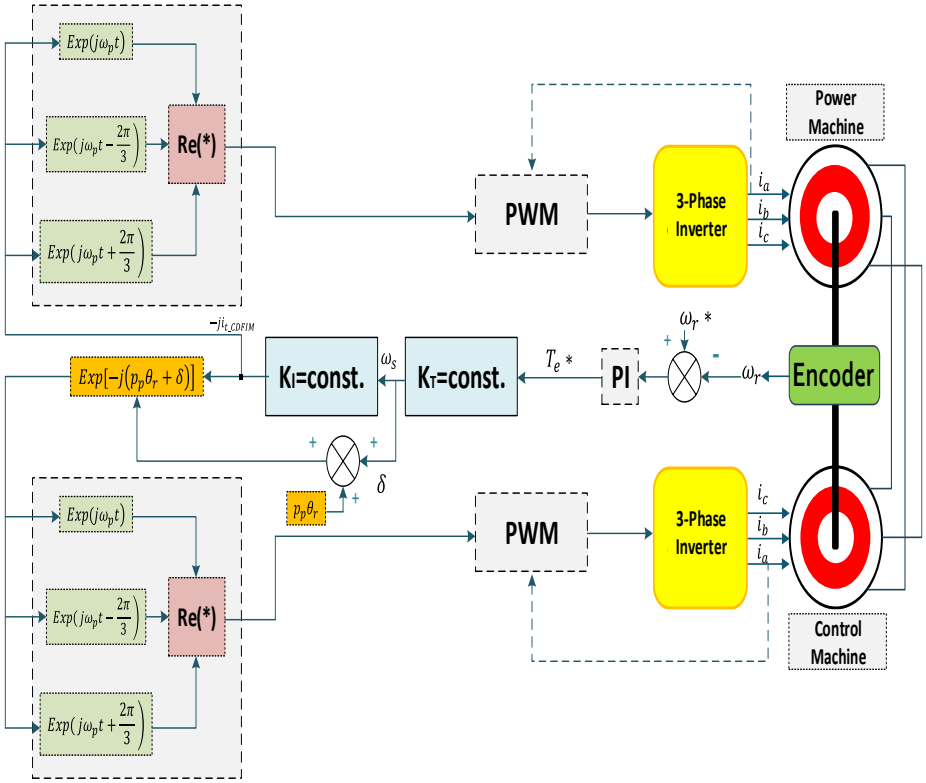

Fig. 2.11. Control scheme of the cascaded doubly fed induction motor [87]

2.5 Hardware in the Loop Technology

Wind energy is one of the most developed energies in the world. In Europe, the capacity of the wind energy grows 30% more in one year. However, this development needs a strong platform to be tested on. A combination between Programmable Logic Controller (PLC) and a plant dynamics both formed a HIL system that can effectively with a high efficiency test in real-time wind energy where the operation power and the maximum power extracted have been considered [92]. Thus, HIL gave the advantage of knowing the behavior of such a system before investing in it.

HIL applications can be extended to agricultural self-work machinery. In South America market, a case study of MF6690 hybrid combine agricultural self-work machinery has been conducted. By knowing the fact that there is a considerable amount of electronics in this large-size machines, safety is a serious matter in the process of building and testing the agricultural self-work machinery. It’s not similar to the old mechanical agricultural machines where the software was tested directly during the building phase. In agricultural self-work machinery, the testing of the software cannot be conducted during the building phase because it could damage the electronics the machine equipped with. So, HIL system is achieved to test agricultural self-work machinery without risking to damage the machine [93].

HIL systems can be more narrowed to test and utilize power electronics circuits. A fuel cell case study was presented to study the operation of Multi Device Interleaved Boost Converter (MDIBC). The outcomes of this study shows a number of advantages of using HIL system such as; HIL system can test the entire system while some component are not present. Second, the HIL system can test the entire system before inserting it in the actual system. Finally, HIL produce a superior platform for testing with a high efficiency in real-time applications. However, it can be expensive when it comes to the controller equipment such as dSPACE controller board [94].

According to [95], it is endorsed to experiment in real-time rather than a computer simulation. This real-time experiment can be utilized using deferent types of HIL such as eMEG Asim, RT-Lab, RTDS, Typhoon-HIL, HRTSim and dSPASE.

One of the drawbacks of using an HIL system is that when the HIL device doesn't have enough processing power such as FPGAs to run in real-time a resonant converter. In [96], the LLC resonant converter operation frequency is between 10 kHz to 500 kHz or even extend more which might need a CPU frequency up to 10 THz. However, that can be overcome using the right type HIL with the right configurations.

The HIL verifies and tests the control algorithms in real time through virtualizing the vehicle hardware. Saving cost and time with high fidelity, the HIL technology affords a method by which the vehicle model can be investigated under a variety of realistic potential scenarios [97], [98].

The HIL, used in this work, consists of the main module HIL402 and the Digital Signal Processor (DSP 100) and the TI controller (TMS320F28335). The processing power of the DSP controller allows the accurate control of power converters. Therefore, it provides an appealing solution for design validation. It is important to mention that this is the first time that the Typhoon HIL is used in automotive design research applications. This adds more depth to the novelty of the proposed work. Typhoon HIL is widely used for smart grid applications but this work proves its capacity to include new areas of research.

2.6 Characteristics and History of WBG Devices

The basic idea of semiconductors started with the introduction of the point contact germanium transistor in 1950. After that, silicon has become commonly used due to its excellent characteristic. Although silicon devices was the dominant ones for a long period since the late 1950s, its material could not cope with the rapid advancements in the area of power electronics and became an

obstacle for researchers and manufactures to apply new optimization features in the production process [99]. Also, the high losses of the Si devices. The relatively high loss and limited switching speed of the Si devices also limit further improvement on power density, mainly due to the cooling system need for removing loss and passive components need for smoothing and filtering switching ripples.

GaN and SiC have gained much attention recently where they were called the "Next Generation of Semiconductor devices". The major difference between GaN and SiC in comparison with conventional Si is that they have a wider band. Also, the mapping characteristics of Si, GaN and SiC which reveal clearly their wide band gap that's why they were given that name "Wide Band Gap Semiconductors" [99], [100], [101].

A cascade structure is used to turn the GaN-HEMT in the circuit design. This structure consists of a low-voltage Si-MOSFET with the GaN-HEMT in order for easing the process of turning on [102]. The Cascade structure technology has been extensively discussed in [103]. The structure has been evaluated in terms of the device performance, the total cost and the product reliability.

This has been applied on two commercially devices afterwards. It has been shown that this technology contributes in improving the performance of this kind of transistors compared with their silicon counterparts.

2.6.1 Advantages of GaN over SiC:

Theoretically, GaN power devices is suitable for power supplies operate at 200-900 V. whereas SiC can be used in the applications of a higher voltage range typically from 900 to 15000 V [102]. While SiC devices can withstand higher temperatures, GaN has the following advantages:

1. Low threshold gate voltage. Therefore, a higher gate voltage for SiC will be required to obtain the same current in GaN devices.

2. Higher rate of voltage changes with respect to time which accordingly means fast switching in both on and off periods.

It is worth mentioning that as EMI design is done system wide and shielding and grounding are done successfully, Higher ruggedness and switching frequencies will not cause EMI issues.

2.7 Chapter Summary

This chapter discusses the literature review established to start working on the proposed system and provide the necessary analysis and simulation for it. The literature review discusses the different modeling approaches, different motors used in HEV/EVs applications which built a solid foundation for the author to start his research in the area of HEV/EV modeling. This chapter also discusses the characteristics of wide band gap devices as well as their advantages. As a comparison between different motor topologies, the DFIM provides approximately double the torque-speed characteristics for the EV application. The new CDFIM topology introduces a new topology that exploit the advantage of reducing the total losses by replacing the slip rings and carbon brushes of the DFIM and simultaneously have a wide torque-speed operation. Simulation schematics for the three motors have been setup using PSIM software and a profound performance comparison, for the same inverter size and power ratings, among the three topologies has been conducted along with pointing out the merits and demerits of each topology. Moreover, the three designs are FEA evaluated in terms of magnetic quantities and Ohmic losses.

Chapter 3. Dynamical Modeling of HEV/EV Powertrain

3.1 Introduction

In order to find and explore the optimal sizing of the Electric vehicle components, a detailed modeling of the Powertrain is essential. Based on the objective, the modeling approach adopted varies. Modeling techniques are so many in the literature such as steady-state modeling, average modeling, transient modeling…etc. Each modeling technique differs from the others in the level of details it takes into consideration Unlike other modeling techniques, steady-state modeling is fast as it does not need small time steps. Therefore, sizing of major components or fuel consumption prediction rely relies mainly on steady state modeling [49]. On the other hand, transient modeling deals with the components dynamics by providing more details on the powertrain. Small time steps are being applied for transient modelling which in turn slow down the simulation and leads to time-consuming simulations [104]. This type of modelling is essential in modeling Hybrid and Electric vehicles to examine the power electronic circuits fast response.

Also, it can be used to design converters controllers [105]. Moreover, it allows for easier implementation on real time simulators. Table **3-1** explains the merits, demerits and function of the three aforementioned approaches of modelling electrified vehicles. If the steady-state behavior is to be investigated, then the steady state modeling is the suitable one for this. In this thesis, a versatile transient model for a Hybrid/Electric Vehicle is developed and then later tested on a Hardware in the loop (Typhoon HIL) in real time to verify the simulation results. Nissan Leaf Electric Vehicle and GM Chevrolet Volt are both adopted as Benchmarks for our study. The powertrain of a Hybrid/Electric Vehicle can be categorized into two main subsystems; the mechanical subsystem which includes modeling the vehicle body, the tire modeling and the

transmission system modeling and the Electrical subsystem which includes modeling of electric motor, power electronics converters (the inverter and the DC-DC converter), the battery and the controllers. A driver model is also established to control the vehicle in a way that follows a certain driving cycle. Investigating the multiple-speed transmissions for electric vehicles was considered as a major part of this thesis. This work relies more on simulations to develop an accurate model that takes into consideration all the variations during the transients of the vehicle components.

Table 3-1: Comparison between different modelling approaches

	Merits	Demerits	Function
Steady-state Model	- Low computational intensity - Large step time	- Very simple model - No dynamics behaviors are considered. - Needs an accurate losses table.	- Study of power flow within the powertrain. - Determine the optimal sizing for the powertrain components.
Average Dynamic Model	- Gives a quite accurate results for the system dynamics especially for mechanical components.	- It does not consider power electronics dynamics especially in high switching frequencies. - Needs an accurate loss model.	- Design a robust control system and allow for fine tuning it.
Fully-detailed Transient Model	- Show detailed transient behavior especially for high switching frequencies.	-High computational intensity. - Very small step time	- Obtaining accurate and precise results when implemented on controller hardware-in-the-loop (HIL).

Power simulation software (PSIM) is adopted in this work to build the whole model due to its rapid processing of power converters schematics. Moreover, it is easy to be interfaced with Hardware in-the-loop technology which used to obtain experimental results. The control system

of the simulation schematic can be easily converted into a C-code through using a Code Composer Studio software and then downloaded on the DSP board [106], [107].

3.2 Vehicle Model

The vehicle model is almost the same for any powertrain in terms of the governing equations. However, parameters such as mass, wheel radius, dimensions, etc. are different for various case study vehicles. We can divide the vehicle model to the vehicle body itself and the various forces acting on to it and the modeling of the components inside the vehicle such as motors, converters and transmission system. In other words, the vehicle model can be classified to electrical modeling and mechanical modeling [76]. The vehicle mass can be deemed as sprung mass which includes the body of the car and the un-sprung mass which includes the wheels and the suspension system.

Through considering different forces acting on the vehicle body, the longitudinal and vertical acceleration can be calculated.

3.2.1 Mechanical Modeling

3.2.1.1 Vehicle Dynamics

Modeling the vehicle dynamics is so crucial to calculate the required power demand by the wheels to meet the instantaneous driving conditions. Also, calculating the forces acting on the vehicle while moving, such as the aerodynamic drag force, the rolling resistance and the grading resistance which are classified under the resistive forces category as well as the propelling force, is of great importance to accurately and precisely determine the required wheel power demand. The longitudinal vehicle dynamics can be modeled based on the generic equation (3.1) [105], [108]:

$$m_c\, a_c = F_T - (F_{dr} + F_R + m_c\, g \sin\delta) \tag{3.1}$$

Equation (3.2) is used to obtain the power demand of the vehicle wheels:

$$P_d = V_c\, F_T = V_c (m_c\, a_c + F_{dr} + F_R + m_c\, g \sin\delta) \tag{3.2}$$

Where

$$a_c = \frac{v(t+\Delta t) - v(t)}{\Delta t}$$

$$F_R = m_c\, g\, C_r \cos\delta$$

The aerodynamic drag force results from the car body moving through air is deemed one of the resistive forces acting on the car body. Equation (3.3) shows how to calculate the drag force F_{dr} in terms of the frontal area A_f , the air density ρ, the aerodynamic drag coefficient C_{dr} and the vehicle speed V_c [108].

$$F_{dr} = \frac{1}{2} \rho V_c^2 A_f C_{dr} \tag{3.3}$$

Rolling resistance force is the other type of the resistive forces acting on the car. It results from the constant contact between the car tire and the road. The heat comes up from the deformation of the tire under compression and recovering so that the energy is dissipated as heat. The rolling resistance force can be calculated as shown in equation (3.4) [108], where f_0,f_1 and f_2 are the rolling resistance coefficients.

$$F_R = f_o + f_1 V + f_2 V^2 \tag{3.4}$$

Based on the road surface material and the road conditions, the constant f_0 varies. However, the other two constantsf_1, and f_2 that are dependent on the vehicle speed have to be accurately adjusted to match the vehicle characteristics.

The suspension model is being represented by an equivalent trailing arm. This layout is deduced from an equivalency procedure comes from a three dimensional suspension geometry. A look-up table is being used within the model to account for the variation of the pivot point characterized by the dimensions C, d, e, f of the trailing arm. Therefore, using this methodology, the sprung mass dynamics is being taken into consideration.

A schematic diagram of the free body diagram of a HEV/EV is shown and explained in Fig. 3.1 whilst the free body diagram of the tire and the trailing arm are shown in Fig. 3.2 and Fig. 3.3 respectively. Fig. 3.1 shows the different tire torques and resistive forces acting on the body of the vehicle as well as the dimensions of the vehicle.

Using this schematic diagram of the vehicle free body diagram and the equivalent trailing arm, we can deduce the balance equations combining the different masses, accelerations and acting forces together using Newton's second law. In terms of the longitudinal direction, the sprung mass, longitudinal acceleration $\ddot{x}_{sm}$, and the tires tractive forces transmitted to the vehicle body through the suspension system F_{jx} are related by equation (3.5) [108].

$$m_{sm}\ddot{x}_{sm} = \sum_{k=L,R} F_{j_{x_{f,k}}} + \sum_{k=L,R} F_{j_{x_{r,k}}} - F_{aer} - F_{RG,x_{sm}} \tag{3.5}$$

Regarding the vertical direction, we can relate the vertical acceleration $\ddot{z}_{sm}$ with the vehicle mass and the acting forces in equation (3.6) [108].

$$m_{sm}\ddot{z}_{sm} = \sum_{k=L,R} F_{j_{z_{f,k}}} + \sum_{k=L,R} F_{j_{z_{r,k}}} + \sum_{k=L,R} F_{j_{s_{f,k}}} + \sum_{k=L,R} F_{j_{s_{r,k}}} + \Delta F_{RG,z_{sm}} \tag{3.6}$$

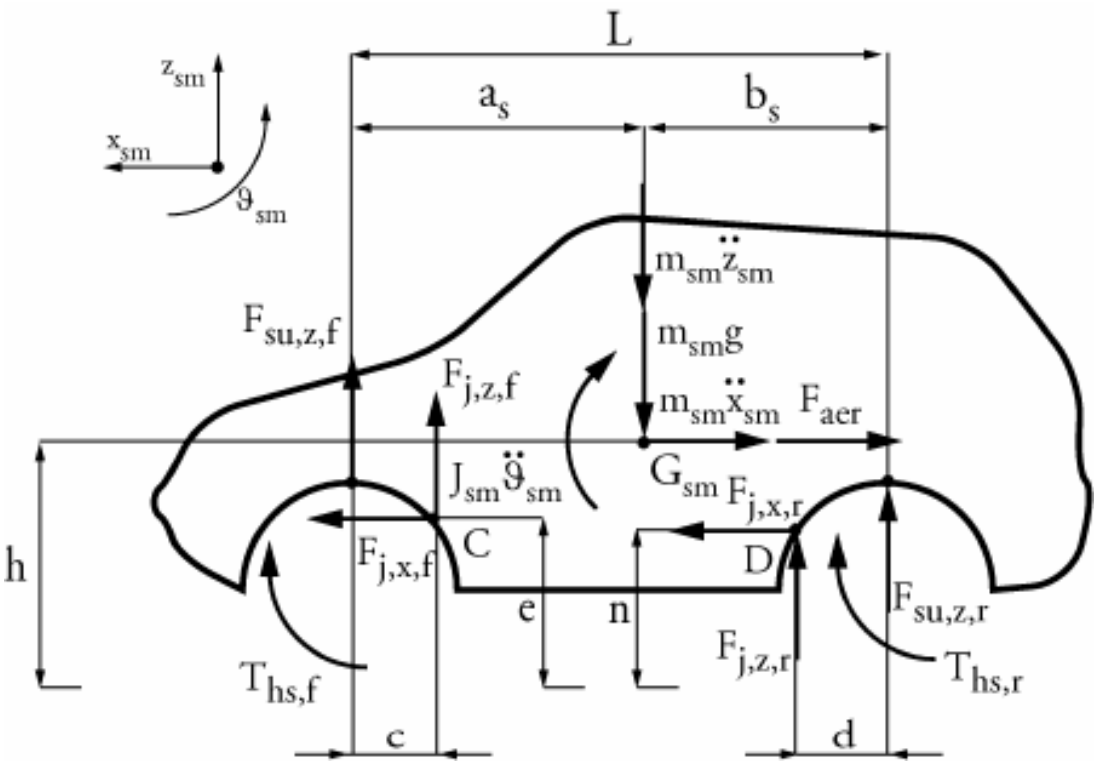

Fig. 3.1. Sprung mass free body diagram [109]

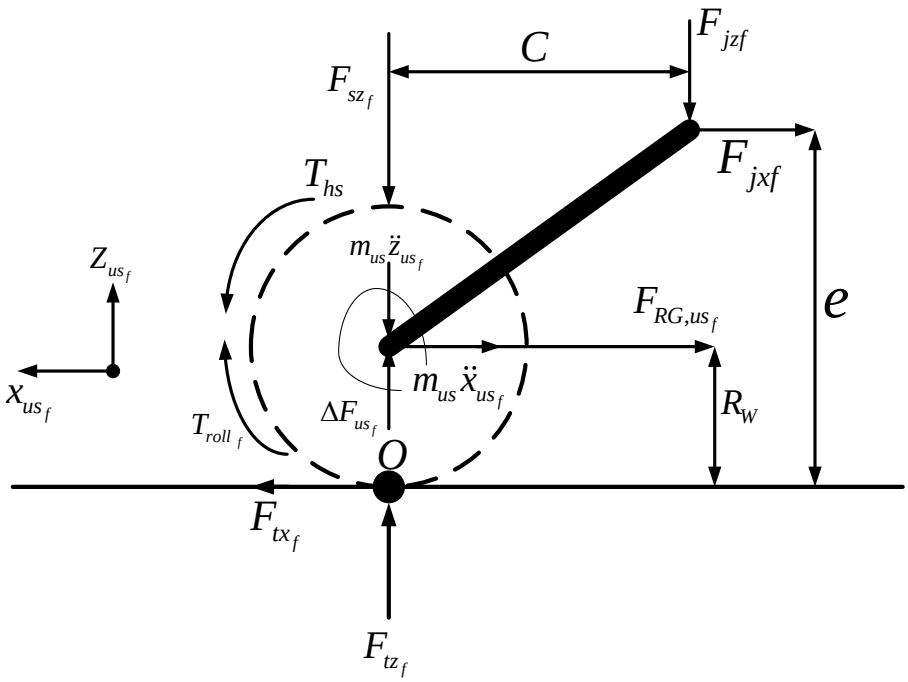

Fig. 3.2. Free body diagram of the tire (un-sprung mass) [108]

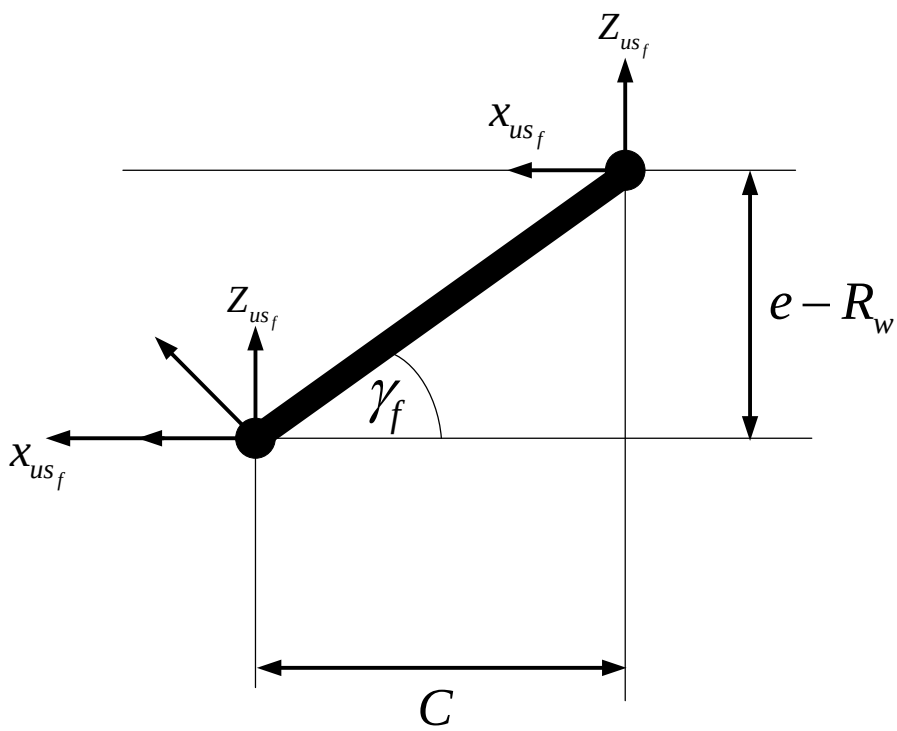

Fig. 3.3. Trailing arm free body diagram [108]

Furthermore, the relationship between vehicle dimensions, rotational acceleration $\ddot{\theta}_{sm}$ and forces can be described by equation (3.7) [51], [108] .

$$\begin{aligned} J_{sm}\ddot{\theta}_{sm} &= -(F_{j_{s_{f,R}}} + F_{j_{s_{f,L}}})a - (F_{j_{z_{f,R}}} + F_{j_{z_{f,L}}})(a-c) \\ &-(F_{s_{z_{r,R}}} + F_{s_{z_{r,L}}})b - (F_{j_{z_{r,R}}} + F_{j_{z_{r,L}}})(b-d) \\ &-(F_{j_{x_{f,R}}} + F_{j_{x_{f,L}}})(H_{CG,sm} - e) + (F_{j_{x_{r,R}}} + F_{j_{x_{r,L}}})(H_{CG,sm} - f) \\ &-F_{roll,f} - F_{roll,r} \end{aligned} \tag{3.7}$$

The un-sprung mass longitudinal displacement x_{us_F}, the displacement of the un-sprung mass x_{sm} resulted from the sprung mass vertical displacement, the angle of the trailing arm, and the vertical displacement of the wheels are related to each other using equation (3.8) [74], [108].

$$x_{us_f} = x_{sm} + z_{us_f} \tan\gamma_f = x_{sm} + z_{us_f}\left(\frac{e - R_w}{c}\right) \tag{3.8}$$

In the longitudinal direction, the balance equation combines the vehicle mass, the tire longitudinal force, the resistive force of the un-sprung mass due to road steepness described by equation (3.9) [108].

$$m_{us_f} . \left[x_{sm} + z_{us_f}\left(\frac{e - R_w}{c}\right)\right] = F_{t_{x_f}} - F_{j_{x_f}} - F_{RG_{us_f}} \tag{3.9}$$

The un-sprung mass and the road angle inclination are related to the force resulted from weight variation by the following equation (3.10) [108]:

$$F_{RG_{us_f}} = m_{us_f}\, g \sin\alpha \tag{3.10}$$

The force balance equation in the vertical direction correlates the un-sprung mass m_{us_f} and its corresponding vertical acceleration $\ddot{z}_{us_f}$ with the vertical tire force $F_{t_{z_f}}$, the suspension vertical force $F_{j_{s_f}}$, the pivot point of the suspension system $F_{j_{z_f}}$, and the weight variation of the un-sprung mass ΔFw_{us_f} explained in equation (3.11) [108]:

$$m_{us_f} . \ddot{z}_{us_f} = F_{t_{z_f}} - F_{j_{s_f}} - F_{j_{z_f}} + \Delta Fw_{us_f} \tag{3.11}$$

In terms of the road inclination angle, the variation in the weight force can be calculated by equation (3.12) [108]:

$$\Delta Fw_{us_f} = m_{us_f}\, g\,(1 - \cos\alpha) \tag{3.12}$$

The force balance equation of the point of contact between the tire and the road can be represented by the following equation (3.13) [108]:

$$m_{us_f} R_w \left[\ddot{x}_{sm} + \ddot{z}_{us_f} \left(\frac{e - R_w}{c} \right) \right] = -F_{J_{z_f}} c - F_{J_{x_f}} e - F_{RG_{us_f}} R_w - T_{roll_f} + T_{hs_f} \tag{3.13}$$

This equation includes many factors such as the half-shaft torque which is considered as an amplification of the motor's output power multiplied by the gear ratio whereas the motor torque is open-controlled.

The angular acceleration can be determined using equation (3.14) [108]:

$$m_{us_f} R_w \left[\ddot{x}_{sm} + \ddot{z}_{us_f} \left(\frac{e - R_w}{c} \right) \right] = -F_{J_{z_f}} c - F_{J_{x_f}} e - F_{inc_{us_f}} R_w - T_{roll_f} \tag{3.14}$$

It can be deduced that there is no half-shaft torque as this equation is mainly for a non-driven wheel.

As a spring combined with a damper, the vertical tire force can be modeled. The tire stiffness force depends on the tire vertical displacement. However, the tire damping force depends on the tire velocity [110]. Equation (3.15) describes the relation between the vertical tire force, the stiffness coefficient P_t, damping tire coefficient C_p, the wheel vertical displacement and the vehicle speed [108].

$$F_{t_{z_f}} = P_t (Z_{in_F} - Z_{us_F}) + C_p (\dot{Z}_{in_F} - \dot{Z}_{us_F}) \tag{3.15}$$

The same modeling of a spring combined with a damper system is applied to the suspension system in equation (3.16). The vertical suspension force depends on the following variables, the suspension damping coefficient C_p, the suspension stiffness coefficient K_f, the vertical displacement of the wheel Z_{us_f}, the vertical displacement of the sprung mass Z_{sm}, vertical velocity of the wheel $\dot{Z}_{us_F}$, vertical velocity of the sprung mass $\dot{Z}_{sm}$ [110].

$$F_{j_{z_f}} = K_f\,(Z_{us_F} - Z_{sm}) + C_p\,(\dot{Z}_{us_F} - \dot{Z}_{sm}) \tag{3.16}$$

The vertical displacement of the sprung mass at the upper suspension point for the front end Z_{p_f} and the rear end Z_{p_r} is affected by the pitch of the vehicle, θ_{sm}, and is therefore calculated through equations (3.17) and (3.18) [108]:

$$Z_{p_f} = Z_{sm} - \theta_{sm} a \tag{3.17}$$

$$Z_{p_r} = Z_{sm} + \theta_{sm} b \tag{3.18}$$

In order to design an optimum suspension system, a considerable amount of attention should be given to the pitch angle θ_{sm} in studying the pitch dynamics. This angle represents the angle between the center of the vehicle wheel and the pivot point. In furtherance of obtaining a pitch equalization, the pitch angle should be high enough to concentrate the longitudinal forces in the wheel center.

To optimally design the pitch angle for the front and rear suspension, the resultant forces should be carefully considered. The front suspension pitch angle should be estimated in a way that makes the reaction forces pointing to the vertical direction and thus through the shock absorber whilst the rear one should be high as much as possible to keep the pitch equalization [108], [111].

The tire longitudinal force is considered as the propulsion force for the vehicle. Therefore, the vehicle speed which is the same as the sprung mass speed can be calculated once this force is determined.

The rotational velocity of the tire relative to the rotational velocity of the vehicle is defined as the slip ratio σ that ranges between -1 and +1. The higher the σ is, the greater the traction force

is. The slip σ can be calculated using equations (3.19) and (3.20) [108] in acceleration and deceleration in order,

$$\sigma = \frac{\dot{\theta}_{wf} R_w - V_{act}}{\dot{\theta}_{wf} R_w} = 1 - \frac{V_{act}}{\dot{\theta}_{wf} R_w} \tag{3.19}$$

$$\sigma = \frac{\dot{\theta}_{wf} R_w - V_{act}}{\dot{\theta}_{wf} R_w} = 1 - \frac{\dot{\theta}_{wf} R_w}{V_{act}} \tag{3.20}$$

As being a non-rigid body, the tire longitudinal force does not apply directly to the road. This is because the tire can be deformed and the torque resulted from the wheel hub is not applied momentarily and is subject to a delay τ_{RL} . Hence, the delayed slip ratio σ_d can be calculated using the following equations (3.23) and (3.24) where S_{RL} is considered as the relaxation length which is the distance the tire needs to generate 63% of the steady state longitudinal force

$$\sigma = \tau_{RL} \dot{\sigma}_d + \sigma_d \tag{3.21}$$

$$\sigma_d = \int \frac{V_{act}}{S_{RL}} (\sigma + \sigma_d) d_t \tag{3.22}$$

3.3 Intelligent Driver Model

In order to compensate giving a real torque command as happens in a real vehicle, an intelligent driver model is designed to emulate the accelerator and brake pedals. The desired torque is being generated using a Proportional-Integral (PI) controller that takes an input of the speed error as shown in Fig. 3.4. Therefore, the desired speed (the reference speed) whether increasing in case of accelerating the vehicle or decreasing in case of braking the vehicle when a negative torque is being applied can be easily reached. In order to limit the rapid changes in the acceleration/brake requests, a rate limiter is added at the output of the PI controller. Sudden changes in

acceleration/brake have not been considered as it will drive the system into the unstable region due to high speed changes $\frac{dv}{dt}$ which cannot be handled using the designed controller. In other words, a mild driving pattern is adopted and assumed in this study.

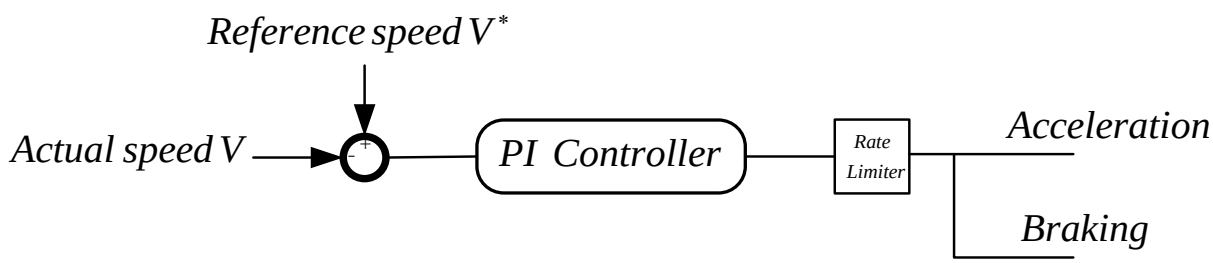

Fig. 3.4. Driver model schematic

3.3.1 Transmission System Modeling

The powertrain has to offer speed conversion between the wheel and the motor speeds enabling the vehicle to [106], [77]:

(1) Operate under different circumstances,

(2) Reach the required utmost velocity, and

(3) Operate within the stable regions of the motor performance chart.

The maximum ratio required, the maximum road-speed ratio, and the smallest powertrain ratio are being determined by the aforementioned conditions, respectively. The goal of general automotives transmissions is to provide the vehicle with best performance including both economic and dynamic performance via using several ratios.

a) Transmission ratios for single ratio EV

Single ratio transmissions are frequently applied in EVs to increase available torque at the wheels at a cost of top speed. At low speed, the maximum ratio can be defined by the requirement of the vehicle to achieve hill climbing capabilities. To evaluate this, the vehicle speed can be

considered as essentially a certain speed and aerodynamic drag is reduced to zero, with no acceleration.

b) Ratio selection for two speed transmission

For a two speed EV, the transmission is only two gears. Complementing the two speed transmission demands, a gear shift schedule to decide when it is necessary to change gears. Shifting is controlled based on a shift map designed to improve the operation of the electric motor in the higher efficiency region.

3.3.2 Gearshift Model

The gearshift model shown in Fig. 3.5 can be classified into two gears; first gear and second gear. The details for each one of them is explained in the following sections.

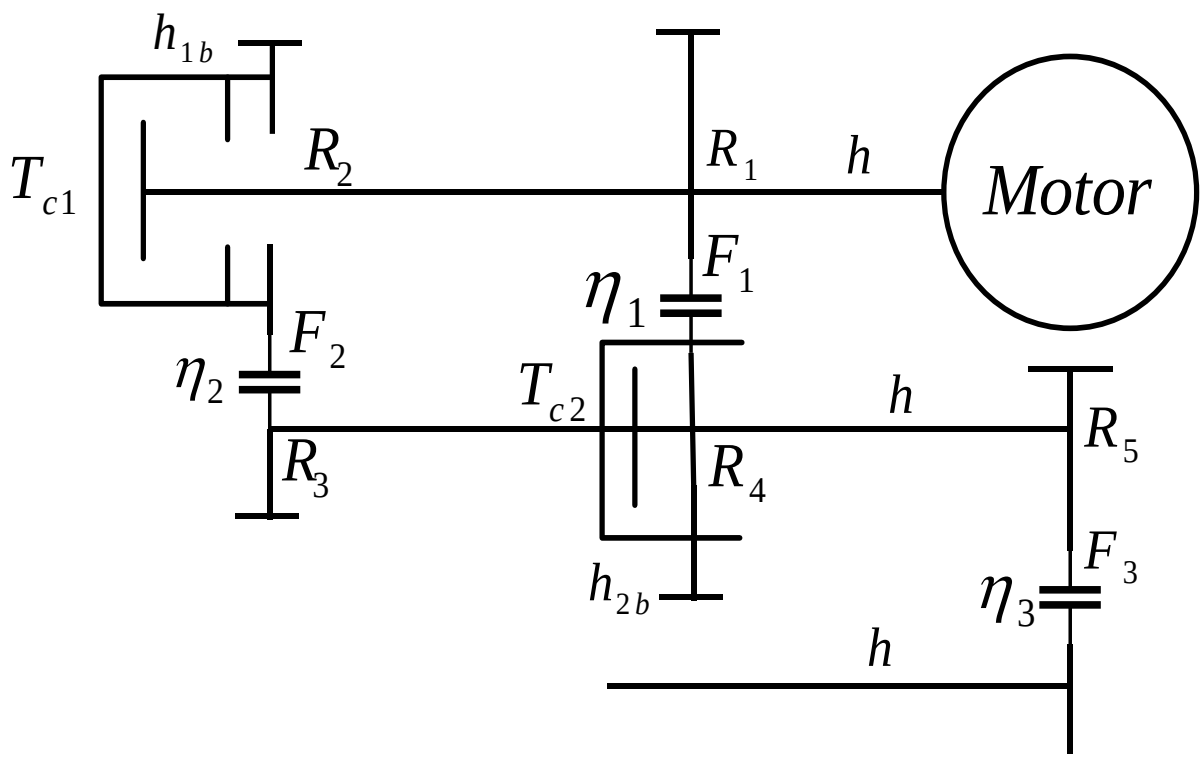

(a) Gear model schematic

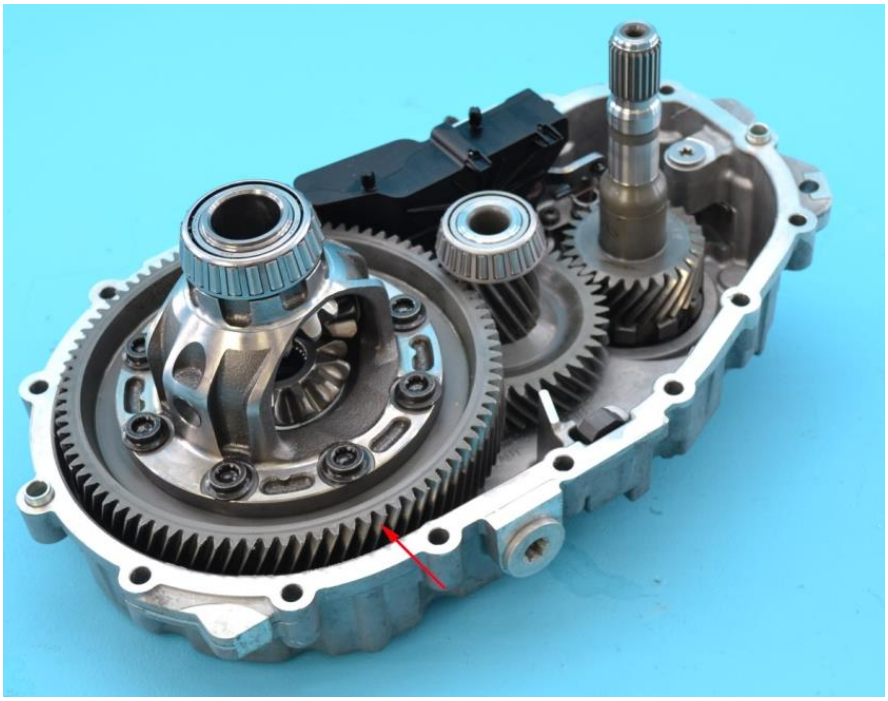

(b) inMotive two-speed transmission inGear (Courtesy of inMotive)

Fig. 3.5. Transmission system

3.3.2.1 First Gear

Equation (3.23) shows the torque balance equation of the primary shaft. $\ddot{\theta}_1$ is the angular acceleration of the primary shaft whilst J is its moment of inertia. F_1 is the force transmitted by the first gear and R_1 is the first gear radius [76], [112].

$$T_{m,del} - F_1 R_1 = (J_m + J_1)\ddot{\theta}_1 \tag{3.23}$$

However, the dry clutch torque balance explained by equation (3.24) in which F_2 is the force transmitted by the second gear, R_2 is the radius of the second gear, η_2 is the second gear efficiency, J_{1b} is the moment of inertia, and $\ddot{\theta}_{1b}$ is the rotational acceleration of the friction clutch output.

$$F_2 R_2 \eta_2 = J_{1b}\ddot{\theta}_{1b} \tag{3.24}$$

Regarding the sprag clutch shaft, equation (3.25) explains its torque balance equation. R_5 is the radius of the first gear, T_{c2} is the sprag clutch shaft, J_2 is the moment of inertia of the sprag clutch/gear assembly, and $\ddot{\theta}_2$ is the rotational acceleration of the sprag clutch/gear assembly [77].

$$T_{c2} - F_2 R_3 \eta_2 - F_3 R_5 = J_2 \ddot{\theta}_2 \tag{3.25}$$

The differential shaft torque balance equation is given in equation (3.26). R_6 is the value of the final drive gear, and η_3 is the final gear efficiency .

$$F_3 R_6 \eta_3 - T_{hs_L} - T_{hs_R} = J_3 \ddot{\theta}_3 \tag{3.26}$$

The final differential acceleration can be shown in the following equation (3.27):

$$\ddot{\theta}_{diff} = \frac{T_{m,del}\ \tau_1\ \tau_{diff}\ \eta_1 \eta_3 - T_{hs_L} - T_{hs_R}}{\left[\begin{array}{c} (J_{mot} + J_1)\tau_1^2 \tau_{diff}^2 \eta_1 \eta_3 + (J_2 + J_{2b})\tau_{diff}^2 \eta_3 + \\ J_3 + \frac{1}{2}(J_{hs_L} + J_{hs_R}) \end{array}\right]} \tag{3.27}$$

3.3.2.2 Second Gear

The torque balance for the primary shaft, is given in equation (3.28).

$$T_{m,del} - F_1\ R_1 - F_2\ R_2 = (J_m + J_1 + J_{1b})\ \ddot{\theta}_1 \tag{3.28}$$

The dry clutch shaft moment balance equation is not required as it is locked to and taken into account in the above calculation [76].

The torque balance equation about the secondary shaft, is given in equation (3.29):

$$F_2\ R_3\ n_2 - F_3\ R_5 = J_2\ \ddot{\theta}_2 \tag{3.29}$$

The torque balance equation about the sprag clutch which spins freely on the secondary shaft due to the over run, is given in equation (3.30):

$$F_1 R_4 n_1 = J_{2b} \ddot{\theta}_{2b} \tag{3.30}$$

The torque balance equation about the differential shaft, is given in equation (3.31).

$$F_3 R_6 \eta_3 - T_{hs_L} - T_{hs_R} = J_3 \ddot{\theta}_3 \tag{3.31}$$

The resultant differential acceleration in second gear is given by equation (3.32).

$$\ddot{\theta}_{diff} = \frac{T_e \tau_2 \tau_{diff} \eta_2 \eta_3 - T_{hs_L} - T_{hs_R}}{\left[\begin{array}{c} (J_{mot} + J_1 + J_{1b} + J_{2b_1}) T_2^2 T_{diff}^2 \eta_2 \eta_3 + J_2 T_{diff}^2 \eta_3 + \\ J_3 + \frac{1}{2}(J_{hs_L} + J_{hs_R}) \end{array} \right]} \tag{3.32}$$

3.4 Electrical Modeling

As mentioned before, the Electrical modeling includes the modeling of the permanent magnet motor, the DC-DC converter, the Voltage source converter, and the battery.

3.4.1 Motor Modeling

We can classify the Brushless permanent magnet (BLPM) machines into two main categories with respect to rotor topologies [79]:

a) Interior permanent magnet (IPM) rotor, where magnets are buried within the rotor iron.

b) The surface-mounted permanent magnet (SPM) rotor, where magnets are mounted on the rotor surface.

This mathematical model can be used for describing the dynamics of the permanent magnet synchronous machine with a salient rotor. The model assumes that the stator flux linkage established by the permanent magnets is sinusoidal, which implies that the electromotive forces are sinusoidal. The electrical part of the machine is represented by a second-order state-space model in a synchronously rotating dq reference frame, invariant to the electrical variable

amplitudes, as described in [113]. The dq reference frame is attached to the rotor, and the d-axis is aligned with the rotor magnets as shown in the phasor diagram in Fig. 3.6.

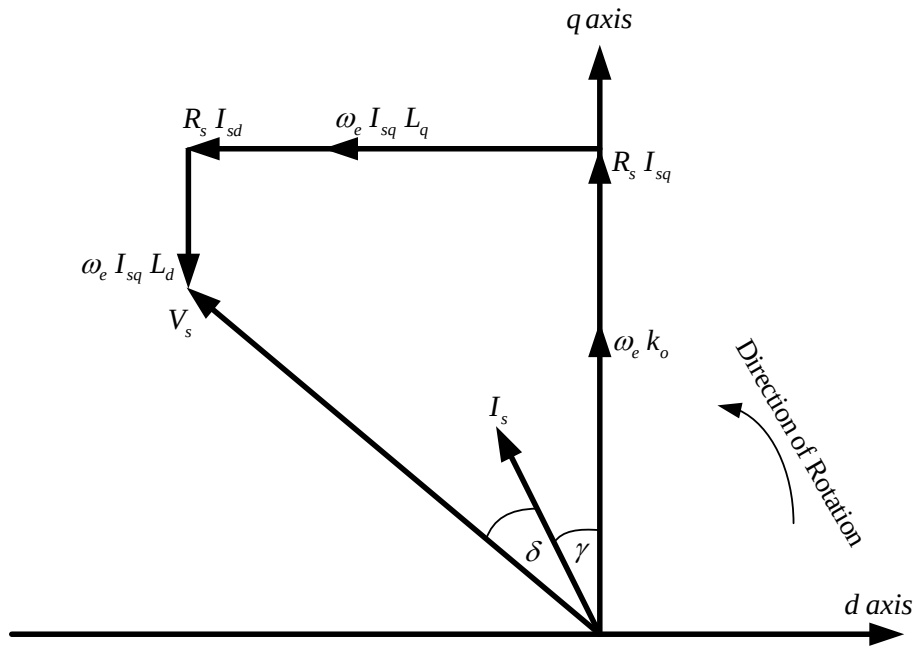

Fig. 3.6. Phasor diagram of the PMSM

The magnets, which have a relative permeability close to unity, appear as an air gap to the stator magneto-motive force. Therefore, for the IPM machine, since the magnets are on the rotor direct axis and the quadrature axis paths have a larger iron contents, the direct axis reactance is less than the quadrature axis reactance, which results in rotor saliency [64]; for SPM machine, the reluctance between the stator and the rotor is essentially uniform and hence the direct axis reactance and quadrature axis reactance can be regarded as the same.

It has been reported that BLPM machines have relatively high efficiency, high torque, and high power density for low speed operation because the excitation provided by PMs is current free and lossless, while PM machines inherently have a short constant power range since the fixed flux magnets limit its extended speed range [65-69]. However, the PM material is electrically resistive

(approximately 70 times that of copper) and hence the rotor PM segments in high performance machines are axially laminated to reduce eddy currents [114].

To investigate general machine operational characteristics, a linear electro-magnetic model of a BLPM machines can be considered. The model is implemented in a classical linear two axis approach and simplified with some assumptions. Firstly, the magnetic saturation is neglected, which results in constant equivalent circuit inductances and magnet flux-linkage. Then, both the stator winding distribution and machine inputs are assumed to be sinusoidal so that the air gap space harmonics and switching harmonics during power electronic converter are neglected. In this way, the machine parameters which have significant influence on the machine power capability over a wide speed range can be determined, which clearly identifies the machine design procedure [83]. These considerations are generally appropriate for the SPM, but need some care for the IPM, since the magnetic circuit and hence machine parameters are no longer linear due to magnetic saturation and cross-field effects. Notwithstanding this comment, thus analysis is still useful to develop the basic operational concepts and design ideas [18].

Since there are no electrical circuits on the rotor of BLPM machines, the machine per phase voltage equation comprises of the stator voltage equation (3.33):

$$V_s = R_s\, i_s + \frac{d}{dt}(L_s i_s + y_{PM}) \tag{3.33}$$

Where R_s is the phase winding resistance, L_s is the phase synchronous-inductance, i_s and y_{PM} are phase current and PM flux space phasor respectively.

The voltage equations in the synchronously rotating reference frame can be split into direct and quadrature parts as shown in equations (3.34) and (3.35):

$$V_{sd} = R_s\, i_{sd} + L_d \frac{di_{sd}}{dt} - \omega_e L_q\, i_{sq} - \omega_e \psi_{PMq} \tag{3.34}$$

$$V_{sq} = R_s\, i_{sq} + L_q \frac{di_{sq}}{dt} + \omega_e L_d\, i_{sd} + \omega_e \psi_{PMd} \tag{3.35}$$

For steady-state operation, the time derivative terms can be equated to be zero. The voltage equations explained in (3.36) and (3.37), based on the machine vector diagram shown in Fig. 3.6, are expressed as follows [115]:

$$V_s \sin\delta = R_s\, I_s \sin\gamma + \omega_e L_q\, I_s \cos\gamma \tag{3.36}$$

$$V_s \cos\delta = R_s\, I_s \cos\gamma - \omega_e L_d\, I_s \sin\gamma + \omega_e k_o \tag{3.37}$$

Therefore, the electrical angular speed can be calculated as shown in equation (3.38):

$$\omega_e = \left(\frac{-b + \sqrt{b^2 + 2ac}}{2a} \right) \tag{3.38}$$

Where:

$$a = (k_o - L_d I_s \sin\gamma)^2 + (L_q I_s \cos\gamma)^2$$

$$b = 2R_s I_s (k_o \cos\gamma + \frac{L_q - L_d}{2} I_s \sin 2\gamma)$$

$$b = 2R_s I_s (k_o \cos\gamma + \frac{L_q - L_d}{2} I_s \sin 2\gamma)$$

$$c = (R_s I_s)^2 + V_s^2$$

Rotor speed can be calculated using equation (3.39):

$$\omega_r = \frac{\omega_e}{p} \tag{3.39}$$

The total power, including copper loss and electro-mechanical power, is calculated using equation (3.40):

$$P = 3(V_{sq}\, I_{sq} + V_{sd}\, I_{sd}) \tag{3.40}$$

By neglecting copper loss, which is reasonable for highly efficient machines, the electro-mechanical power as a function of the machine parameters, phase current magnitude and current excitation angle can be expressed in equation (3.41):

$$P_e = 3\omega_e (k_o\, I_s \cos\gamma + \frac{L_q - L_d}{2} I_s^2 \sin 2\gamma) \tag{3.41}$$

Hence, the electro-magnetic torque is derived as depicted in equation (3.42):

$$T_e = 3\, p\, (k_o\, I_s \cos\gamma + \frac{L_q - L_d}{2} I_s^2 \sin 2\gamma) \tag{3.42}$$

This excitation torque equation (3.43) illustrates the main torque combinations in BLPM machines, one arising from the interaction of current and permanent magnet excitation [81]:

$$T_{excitation} = 3\, p\, k_o\, I_s \cos\gamma \tag{3.43}$$

and one arising from the interaction of machine phase current and the variation winding reluctance expressed in terms of the direct- and quadrate-axis inductance, the saliency or reluctance torque in equation (3.44):

$$T_{reluc\tan ce} = 3\, p \left(\frac{L_q - L_d}{2} \right) I_s^2 \sin(2\gamma) \tag{3.44}$$

In constant torque region, for any magnitude of stator phase current, there is an optimum current excitation angle which leads to maximum electro-magnetic torque. As the speed increases, this angle is chosen for maximum torque operation until the maximum phase voltage constrained by

the DC link is reached and then machine enters to the field-weakening region. At the maximum voltage constraint with the increment of machine speed, the current excitation angle rises from the optimum value to 90 degrees. Hence, for BLPM machines where there is no physical field current excitation, field weakening is achieved by supply of a negative component of d-axis stator current vector, which is progressively increased to reduce the machine flux. Therefore, for SPM machine, L_d equals to L_q, hence the torque is maximized when the current excitation angle equals to zero and the current excitation angle progressively increased to field weaken the machine. For IPM machines, the optimum current excitation angle is obtained by differentiating the electro-magnetic torque with respect to the current excitation angle and equating the result to zero as depicted in equation (3.45):

$$\frac{dT_e}{d\gamma} = 3p[(L_q - L_d)I_s^2 \cos(2\gamma) - k_o I_s \sin\gamma] = 0 \qquad (3.45)$$

Solving for the differentiating equation yields the optimum torque angle as shown in equation (3.46):

$$\gamma_{opt} = \sin^{-1}\left(\frac{-C + \sqrt{C^2 + 8}}{4}\right) \qquad (3.46)$$

Where:

$$C = \frac{k_o}{(L_q - L_d)I_s}$$

In terms of the flux linkage rate of the change in the direct axis and the quadrature axis, equation (3.47) describes the correlation between the flux linkage and the voltages. Equations (3.48) ,(3.49), (3.50) and (3.51) describe the transformation between abc and dq frames.

$$\begin{bmatrix} \dot{\lambda}_{ds} \\ \dot{\lambda}_{qs} \end{bmatrix} = \begin{pmatrix} -\frac{R_s}{L_d} & \omega_r \\ -\omega_r & -\frac{R_s}{L_q} \end{pmatrix} \begin{pmatrix} \lambda_{ds} \\ \lambda_{qs} \end{pmatrix} + \begin{pmatrix} 1 & 0 & \frac{R_s}{L_d} \\ 0 & 1 & 0 \end{pmatrix} \begin{bmatrix} V_{ds} \\ V_{qs} \\ \lambda_{PM} \end{bmatrix} \tag{3.47}$$

$$\begin{bmatrix} i_{ds} \\ i_{qs} \end{bmatrix} = \begin{pmatrix} \frac{1}{L_d} & 0 \\ 0 & \frac{1}{L_q} \end{pmatrix} \begin{pmatrix} \lambda_{ds} \\ \lambda_{qs} \end{pmatrix} + \begin{pmatrix} 0 & 0 & -\frac{1}{L_d} \\ 0 & 1 & 0 \end{pmatrix} \begin{bmatrix} V_{ds} \\ V_{qs} \\ \lambda_{PM} \end{bmatrix} \tag{3.48}$$

$$\begin{bmatrix} V_a \\ V_b \\ V_c \end{bmatrix} = \begin{pmatrix} \frac{2}{3} & \frac{1}{3} \\ -\frac{1}{3} & \frac{1}{3} \\ -\frac{1}{3} & -\frac{2}{3} \end{pmatrix} \begin{bmatrix} V_{ab} \\ V_{bc} \end{bmatrix} \tag{3.49}$$

$$\begin{bmatrix} V_\alpha \\ V_\beta \end{bmatrix} = \frac{2}{3} \begin{pmatrix} \cos\theta_{ab} & \cos(\frac{2\pi}{3} - \theta_{ab}) & \cos(\frac{2\pi}{3} + \theta_{ab}) \\ -\sin\theta_{ab} & \sin(\frac{\pi}{3} - \theta_{ab}) & -\sin(\frac{\pi}{3} - \theta_{ab}) \end{pmatrix} \begin{bmatrix} V_a \\ V_b \\ V_c \end{bmatrix} \tag{3.50}$$

$$\begin{bmatrix} V_{ds} \\ V_{qs} \end{bmatrix} = \begin{pmatrix} \cos\theta_r & \sin\theta_r \\ -\sin\theta_r & \cos\theta_r \end{pmatrix} \begin{bmatrix} V_\alpha \\ V_\beta \end{bmatrix} \tag{3.51}$$

As shown in Fig. 3.7, output stator current dq - components are transformed back to the stationary reference frame αβ-components using an inverse Park transformation in the following form in equation (3.52):

$$\begin{bmatrix} i_\alpha \\ i_\beta \end{bmatrix} = \begin{pmatrix} \cos\theta_r & -\sin\theta_r \\ \sin\theta_r & \cos\theta_r \end{pmatrix} \begin{bmatrix} i_{ds} \\ i_{qs} \end{bmatrix} \tag{3.52}$$

Stator current αβ-components are transformed to phase values using an inverse Clarke's transformation is shown in equation (3.53):

$$\begin{bmatrix} i_a \\ i_b \\ i_c \end{bmatrix} = \begin{pmatrix} \cos\theta_{ab} & \sin\theta_{ab} \\ -\cos(\frac{2\pi}{3}+\theta_{ab}) & \sin(\frac{2\pi}{3}+\theta_{ab}) \\ -\cos(\frac{2\pi}{3}-\theta_{ab}) & -\sin(\frac{2\pi}{3}-\theta_{ab}) \end{pmatrix} \begin{bmatrix} i_\alpha \\ i_\beta \end{bmatrix} \tag{3.53}$$

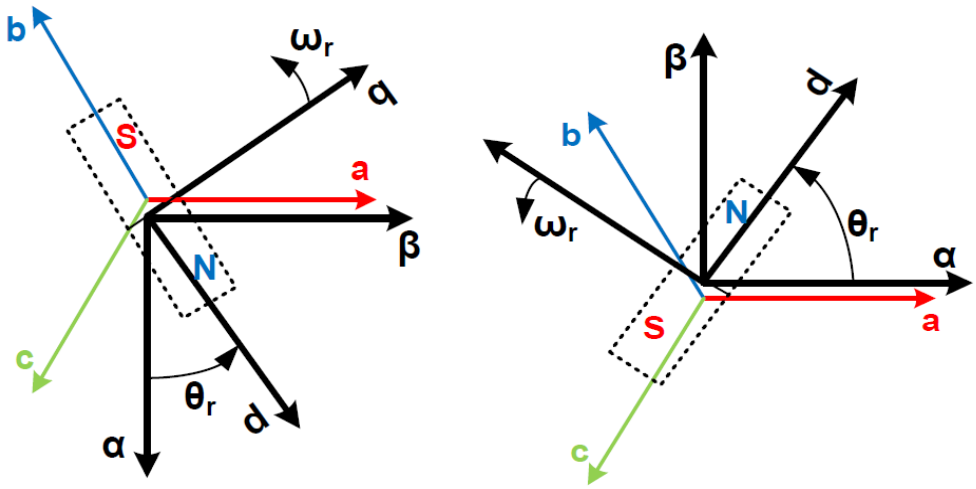

Fig. 3.7. Stationary and rotating reference frames **[116]**

3.4.2 Battery Modeling

The battery modeling is essential for a proper modeling of HEV/EV. The battery modeling can be classified into three main categories; the electromechanical model, the non-linear electric circuit-based model and the experimental model. Each model has its advantages and disadvantages. Because the behavior of the battery depends on chemical reactions that take place inside the battery, its modeling is quite complicated and has to consider these changes. That's why using look-up tables was introduced immensely in the literature to provide an accurate modeling solution for the battery under various operating conditions. However, during real-time simulation, this can be a tedious option to be implemented. Therefore, as we will focus in this thesis on the Hardware-in-the Loop implementation, non-linear electric-circuit based model shown in Fig. 3.8

is adopted. It shows the non-linear model of the Li-Ion battery where the E is the internal voltage, R is the internal resistance, v_b is the terminal voltage and i_{batt} is the battery current. The variations that may occur in the battery internal resistance are ignored and hence the battery internal voltage changes only according to the battery current and the state of charge. Despite not considering the SOC variations on the internal voltage, the electric-circuit based model is still deemed as an effective modeling method due to the fact that considering these effects does impact the performance investigation and it is a time-consuming operation as well. It can be considered as a sophisticated model and may add some complexity to the system. However, it is a fast and accurate representation of the battery [117]–[119].

As being used as a case study, the battery pack used in the GM Chevrolet Volt is composed of 197 Pouch Li-Ion cells, in a 96 series architecture - 3 parallel pack configuration. Each cell has a nominal capacity, Q_{nom}, of 15 Ah and nominal voltage of 3.85 V. The battery pack general schematic can be shown in Fig. 3.9.

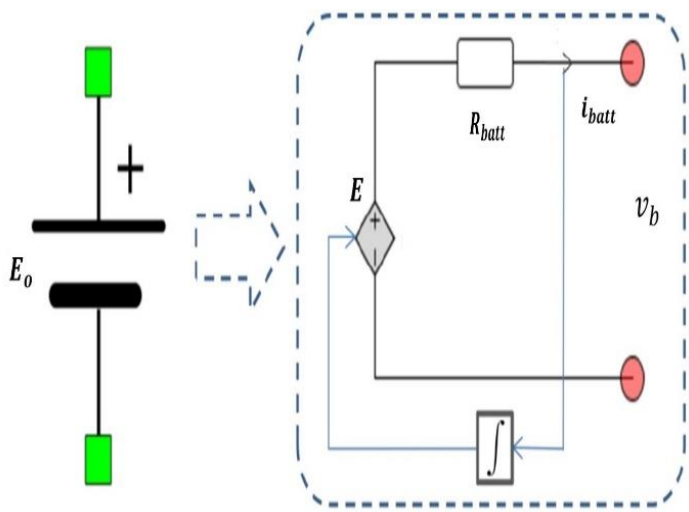

Fig. 3.8. The non-linear model of the battery

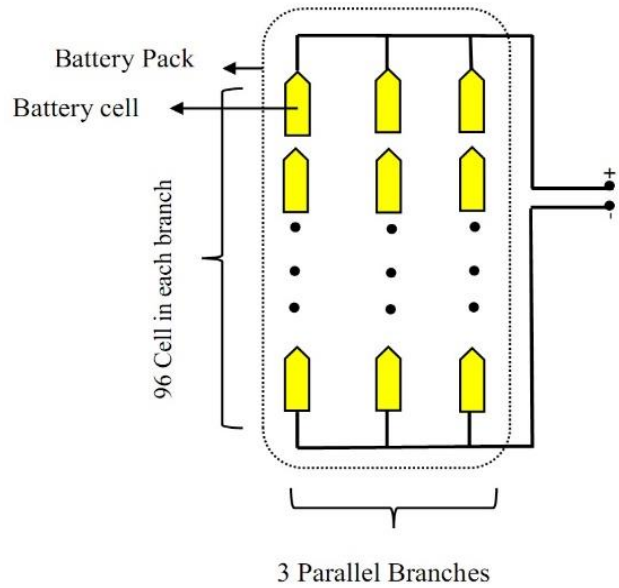

Fig. 3.9. Design of the GM Chevrolet Volt

The internal voltage for charge and discharge conditions can be expressed as a function of the discharge current (i_t) by the following equations [91]:

$Discharge$:
$$E = E_o - k\frac{Q}{Q - i_t} - Ae^{(-B*i_t)} \tag{3.54}$$

$Charge$:
$$E = E_o - k\frac{Q}{-0.1*Q + i_t} - k\frac{Q}{Q - i_t} - Ae^{(-B*i_t)} \tag{3.55}$$

And the discharge state of the battery can be calculated in terms of the battery current as

$$i_t = \int_0^t i_{batt}.dt \tag{3.56}$$

$$SOC = SOC(0) - \frac{1}{c_b}\int_0^t i_{batt}.dt \tag{3.57}$$

Fig. 3.10 shows the V-I characteristics of the Li-Ion battery. The nominal area shown in pink color is the area preferred to be working within.

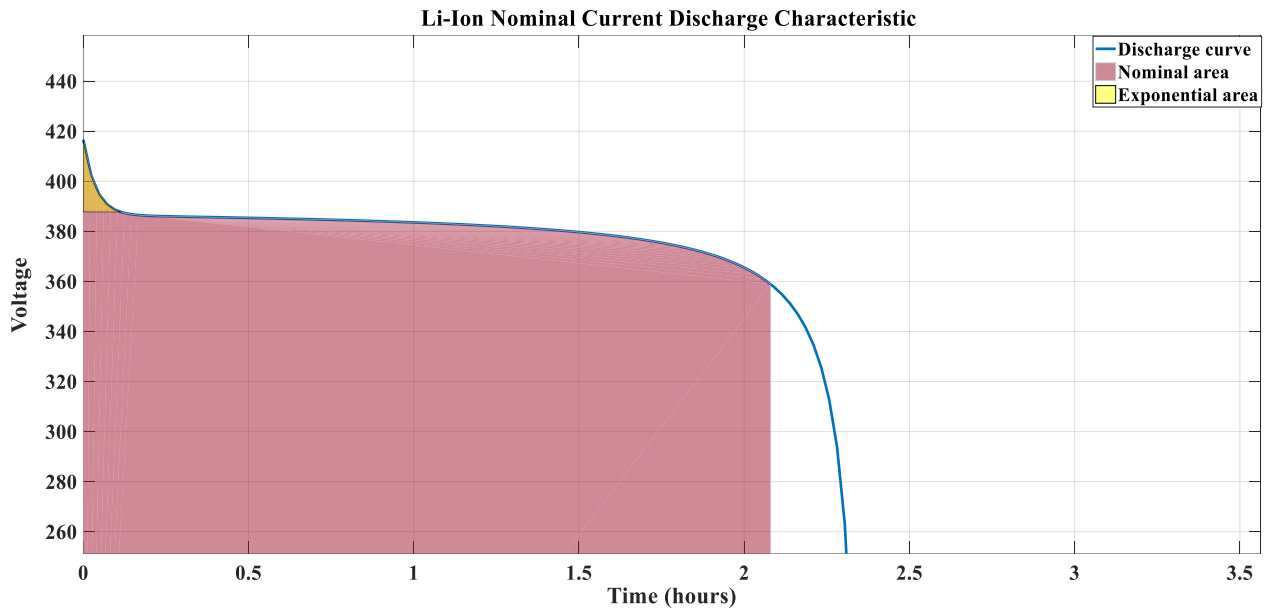

Fig. 3.10. The V-I characteristics of Li-Ion battery

3.4.3 DC-DC Converter Modeling

The DC-DC converter implemented is a Half-Bridge Bidirectional topology. This topology of converter is commonly used in HEV/EV applications. In our model, the DC-DC Converter operates as a boost converter when in dual PMSM EV mode. During this mode, the battery is discharging power to the DC-Bus via the DC-DC Converter. The boost provided during this period is from the battery's 360V to the 700V of the DC-Bus. An inductor of 0.8 mH was selected using equation (3.58) for the converter [120]. This size was selected to remain practical yet also maintain an acceptable ripple current of 4.4A. This ripple current is acceptable and less than 10% of the steady state output current.

$$\Delta I_L = \frac{V_{in}}{V_{out}} * \frac{V_{out} - V_{in}}{f_{sw} * L} \tag{3.58}$$

The implemented design is a controlled half-bridge that provides multi-directional power flow. For example, when the DC-Bus needs power Q1 is forced into commutating while Q2 is controlled to be open or conducting. These conditions imply the circuit is operating as a boost converter [116]. On the other hand, when the DC-Bus has a surplus of power during regenerative braking Q2 will be forced into commutating. It is analogous to realize that during this period the circuit is behaving as a buck converter.

The DC-DC converter shown in Fig. 3.11 is a bidirectional converter meaning that it can work as a boost as shown in Fig. 3.12 or as a buck as depicted in Fig. 3.13 depending on the power flow. Therefore, the power can go from the battery to the DC link and vice-versa. As the DC link voltage is assumed to have a higher voltage than the battery, the converter works a boost converter if the power flows from the battery to the DC link and works a buck converter when it delivers power from the DC link to the battery [116].

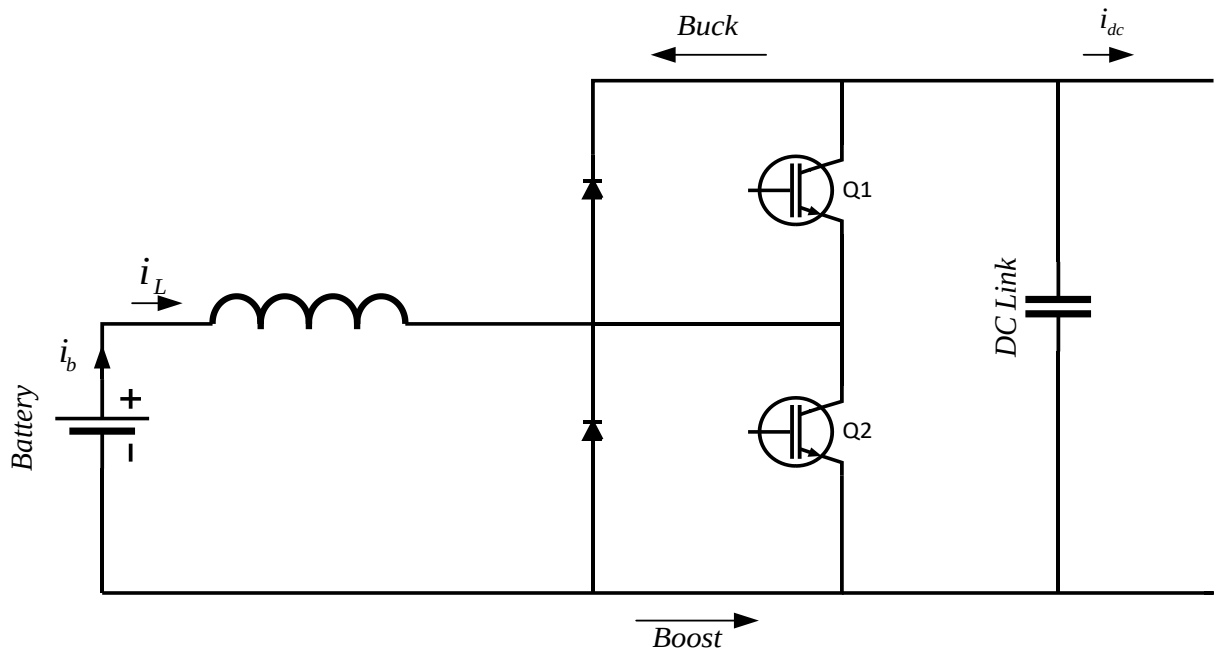

Fig. 3.11. Bidirectional DC-DC converter

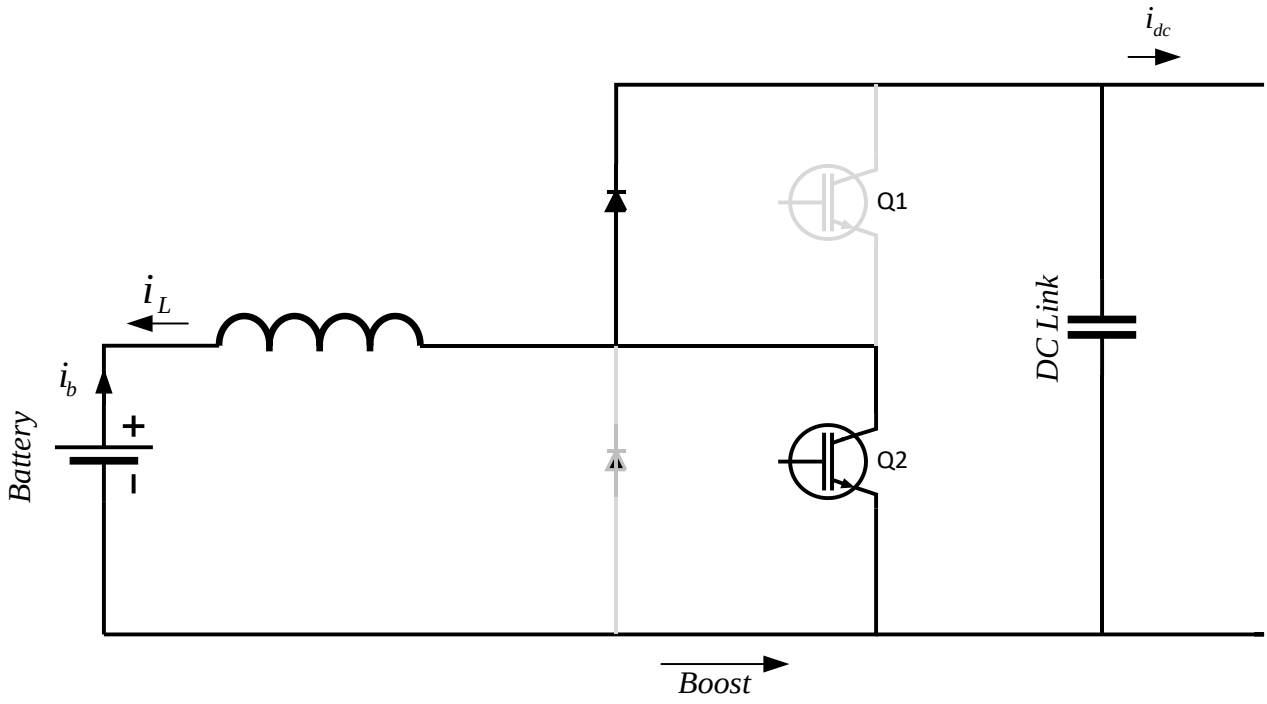

Fig. 3.12. DC-DC converter in the boost (step-up) mode

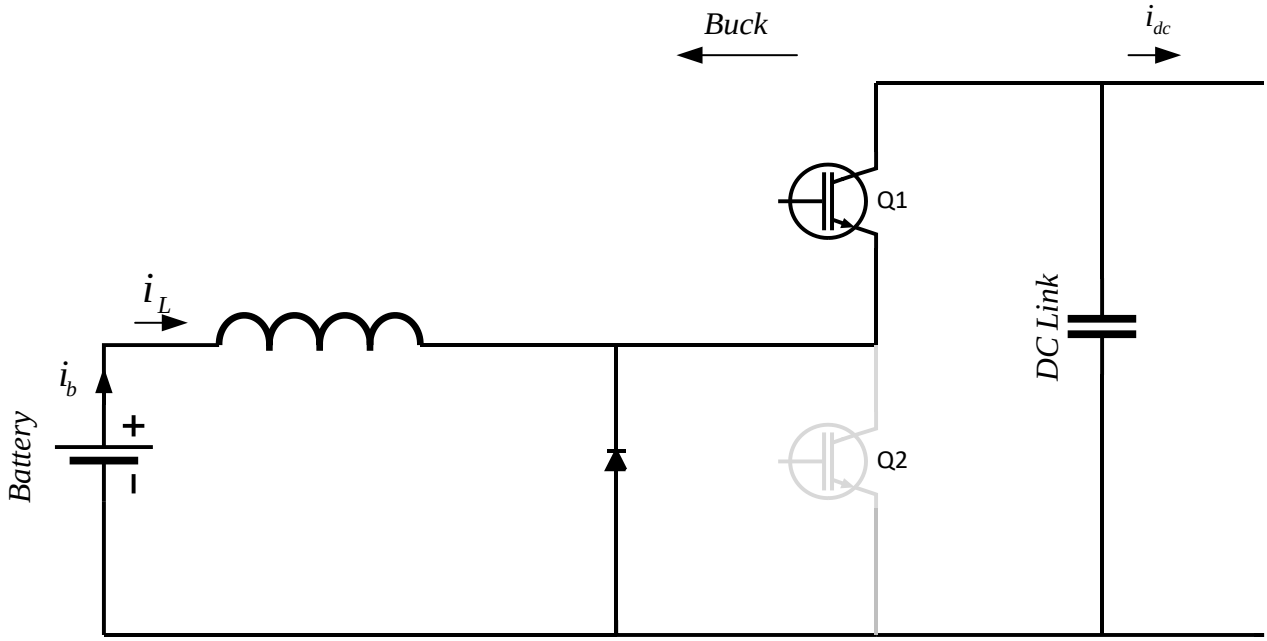

Fig. 3.13. DC-DC converter in the buck (step-down) mode

3.4.4 Inverter

Fig. 3.14 shows the schematic diagram of the inverter used in the powertrain. The inverter, which converts the DC power to AC power, is connected from one side to the DC bus and from the other side to the PMSM. The sinusoidal Pulse Width Modulation (PWM) technique is adopted here to provide the switching pattern for the inverter. The sinusoidal PWM is based on a comparison between the fundamental frequency sinusoidal waveform with a high frequency triangular carrier waveform.

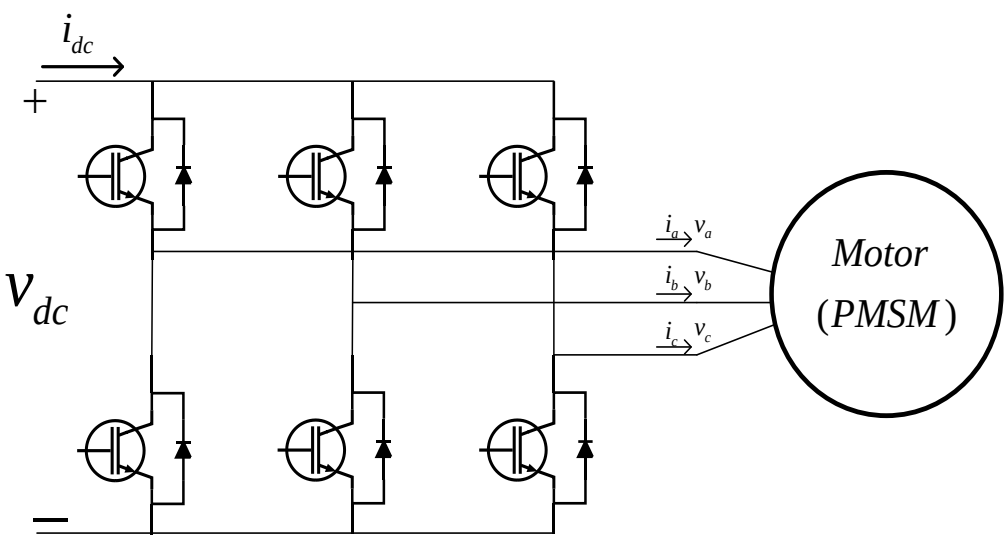

Fig. 3.14. Schematic diagram of the inverter

3.4.5 Controllers

The control scheme of the HEV is quite sophisticated, however, for simplicity we can break it down to four main controllers. Two out of the four controllers are deemed to be high level ones that control the power flow whilst the other ones are low level controllers like those which control the motors and the dc link voltage. The major difference of our model controllers compared with the PSIM library model, which is mainly based on the steady-state model, is the tuning of the

controllers based on the transient model which eventually allows for incorporation of actual hardware components in addition to investigating the behavior of each component in real-time.

3.4.6 Low Level Controllers

3.4.6.1 DC Link Controller

The ultimate goal of this controller is to keep always the dc link voltage constant. In the motoring mode of operation, the voltage of the dc link tends to decrease. Hence, the controller will transfer more power from the battery to the dc link. However, in the regenerative mode of operation, the voltage is more likely to increase so the controller will send the power back to the battery so that it maintains the voltage at the dc link constant for all modes of operation as shown in Fig. 3.15.

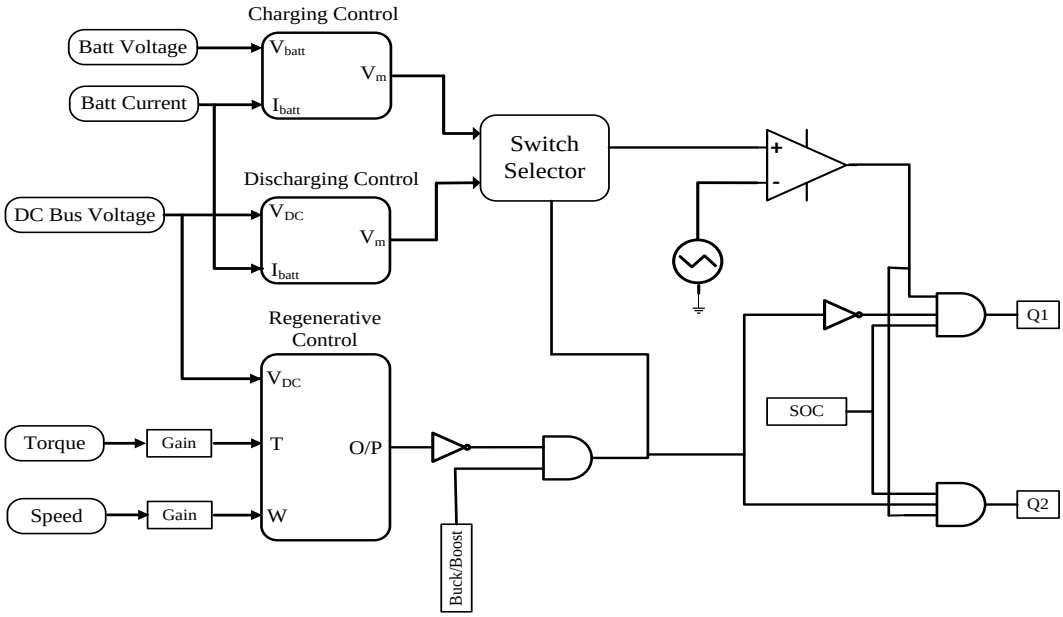

Fig. 3.15. DC link controller

3.4.6.2 Inverter Controller

The inverter controller main function is to provide the switching pattern for the three-leg six-switches inverter in a such a way that outputs the necessary voltage on the motor terminals based on demanded speed and torque as depicted in Fig. 3.16.

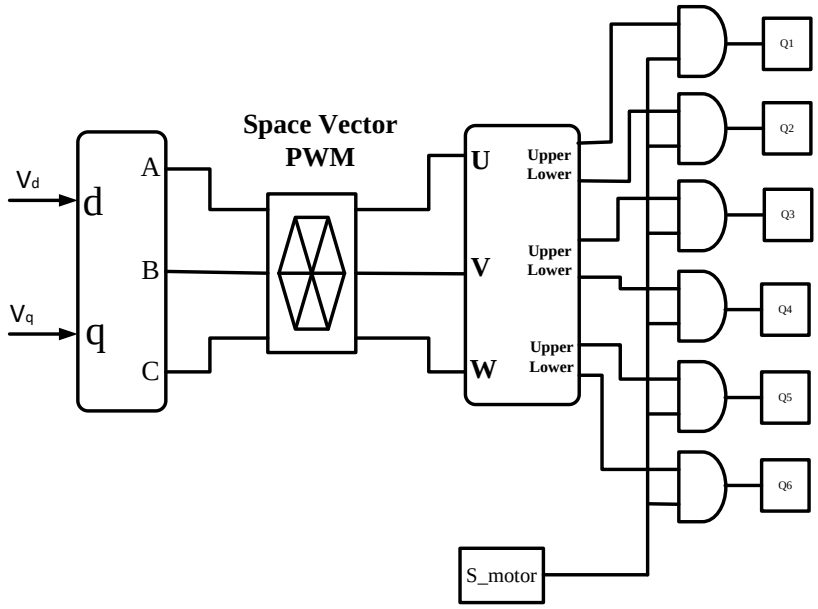

Fig. 3.16. Inverter SVPWM modulation scheme

The two-dimensional Space Vector Pulse Width Modulation (SVPWM) is the modulation scheme adopted for switching the VSI inverter. This technique has been chosen for its accurate switching over the traditional modulation techniques owing to its good utilization of the dc bus voltage as well as obtaining less current ripples and low switching frequency. It is also a simple technique to be applied in digital signal processing and hardware-in-the-Loop because it does not take much time to be executed compared with the conventional PWM techniques which is an important aspect to decrease the burden of huge computational intensity of the transient model. The zero sequence current is not considered following the assumption of a balanced system. Since the basic principle of SVPWM relies on a two-dimensional perpendicular vectors, the voltage vector can be expressed in $\alpha - \beta$ plane as shown in equation (3.59):

$$\vec{V} = \vec{V}_{\alpha} + j\vec{V}_{\beta} \tag{3.59}$$

Also, the transformation matrix used to convert the $a-b-c$ voltages to $\alpha - \beta$ voltages is expressed in equation (3.60):

$$\begin{bmatrix} V_\alpha \\ V_\beta \end{bmatrix} = \frac{2}{3}\begin{bmatrix} 1 & -0.5 & -0.5 \\ 0 & \sqrt{3}/2 & -\sqrt{3}/2 \end{bmatrix}\begin{bmatrix} V_a \\ V_b \\ V_c \end{bmatrix} \tag{3.61}$$

3.4.6.3 Traction Motor Controller

For traction motor control, the strategy adopted is the maximum torque per ampere (MTPA) control approach for any operating point below base speed and flux weakening control approach for any speed above base speed up to maximum speed. For interior permanent magnet motors (IPMs), the torque equation composed of two main components which are reluctance and excitation torques as shown in equation (3.61). The d-q components of the stator current can be expressed as a function of the stator current and the toque angle as depicts in equations (3.62) and (3.63). This MTPA method, as the name of the control methodology reveals, relies on maximizing the torque per unit value of the stator current. Therefore, it is deemed as an efficient control methodology for traction applications. In order to find the maximum torque, the d-q components of equations (3.62) and (3.63) are substituted into equation (3.61) and then the derivative of the resultant equation is obtained and equated to zero to determine the optimum value of I_d as shown in equation (3.64). In terms of the maximum permissible stator current, the values of I_d and I_q are calculated as shown in equations (3.65) and (3.66). It should be noted that the MTPA can only be applied for a speed range from zero to base speed of the motor. However, operating above base speed will increase the back emf which will maximize the output inverter voltage. Therefore, the other control approach which is flux weakening comes into effect by applying a negative d-axis current which will reduce the stator flux linkage that allows for operation at high speeds up to maximum allowable speed but with decreasing maximum available torque. Therefore, the drive

system consists of two main controller loops; current control loop (inner loop) and speed control loop (outer loop).. The inner loop has a faster response compared with the outer loop. A PI controller is used for regulating both the motor speed and the stator current d-q components as shown in Fig. 3.17.

$$T_e = \frac{3}{2}\frac{P}{2}[\lambda_{PM} I_q + (L_d - L_q) I_q I_d] \tag{3.62}$$

$$I_d = I_s \cos\delta \tag{3.63}$$

$$I_q = I_s \sin\delta \tag{3.64}$$

$$I_d = \frac{\lambda_{PM}}{2(L_d - L_q)} - \sqrt{\frac{\lambda_{PM}^2}{4((L_d - L_q)} - I_q^2} \tag{3.65}$$

$$I_{d\max} = \frac{\lambda_{PM}}{2(L_d - L_q)} - \sqrt{\frac{\lambda_{PM}^2}{16((L_d - L_q)^2} + \frac{I_{s\max}^2}{2}} \tag{3.66}$$

$$I_{q\max} = \sqrt{I_{s\max}^2 - I_{d\max}^2} \tag{3.67}$$

The PI controller transfer function is shown below where T_i is the integral time constant and K_{PI} is the tuned gain of the controller.

$$G_{PI}(S) = K_{PI}\frac{1 + T_i s}{T_i s}$$

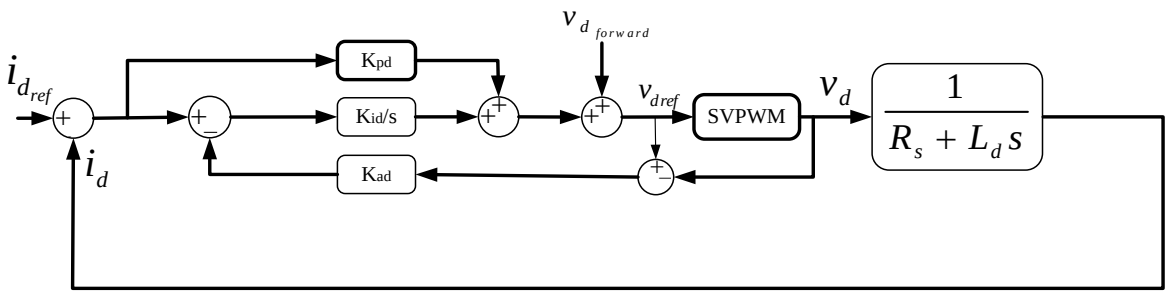

(a) D-axis current controller

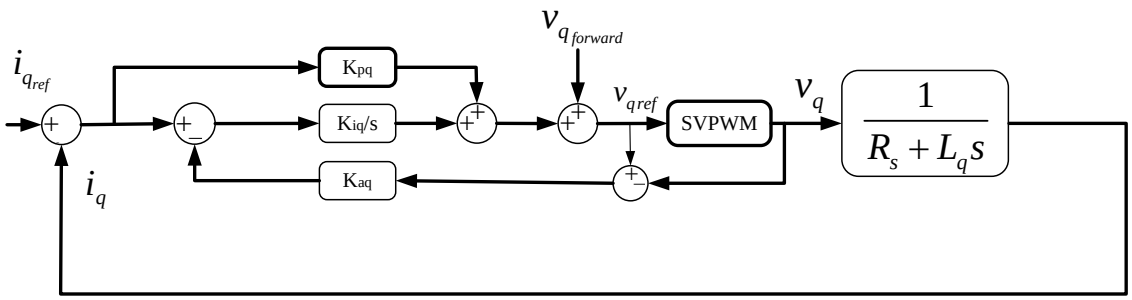

(b) Q-axis current controller

Fig. 3.17. PI controller for MTPA

The outer loop is the speed regulation for which a speed reference from the driving cycle is compared with the actual speed and then the error enters a PI controller to obtain the I_d and I_q reference currents that will be used for the previous current control loop. The speed control loop is shown below in Fig. 3.18.

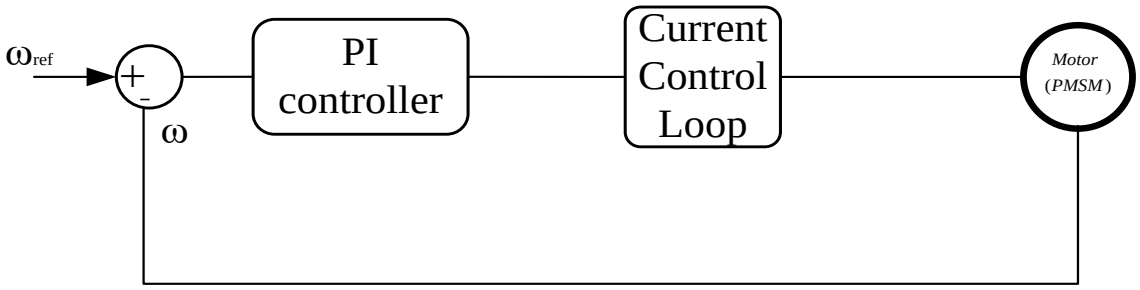

Fig. 3.18. Speed control loop with unity feedback

3.4.7 High Level Controllers

3.4.7.1 Power Divider Controller

This controller controls the power flow among the motor, generator and the combustion engine.

3.4.7.2 Main Vehicle Controller

This controller shown in **Fig. 3.19** is the one responsible for specifying the reference power for the Li-Ion battery and the combustion engine operating point as demanded by the wheel power to keep the speed constant.

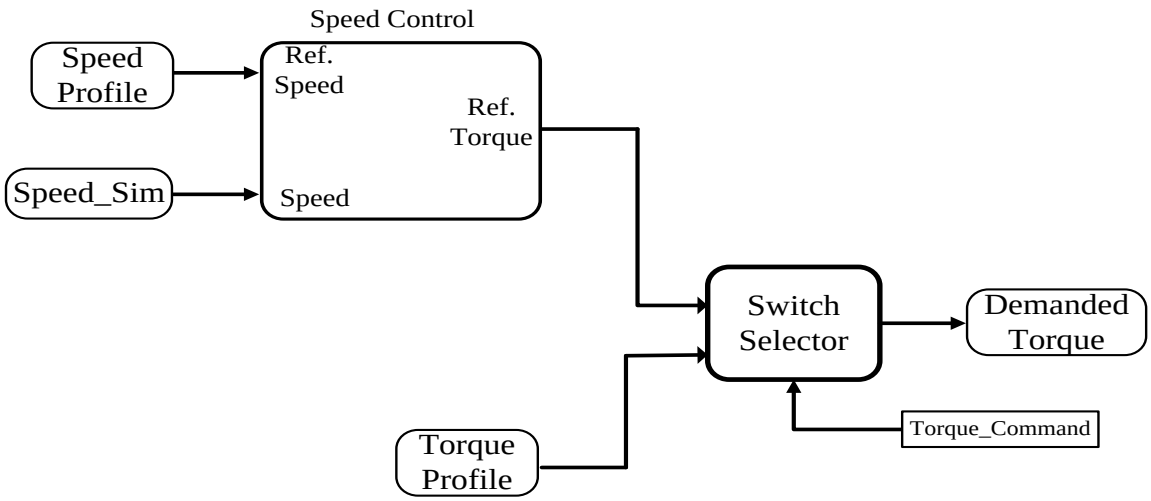

Fig. 3.19. Main vehicle controller

3.5 Chapter Summary

This chapter has explained the development of the vehicle and powertrain models. The models are built in the PSIM environment comprised of equations derived from analyzing the vehicle as a system. The base vehicle model consists of number of degrees of freedom, the vertical, longitudinal and rotational movement of the sprung mass and the vertical, longitudinal and rotational movement of each of the four unsprung masses (the wheels). The model considers the resistive forces due to the road grade, aerodynamic resistance and rolling resistance. The

suspension dynamics are modeled as spring and dampers and allow the analysis of the vehicle pitch and drivability. Moreover, the contribution of this work can be categorized into two approaches; first, each component of the powertrain is accurately modeled taking transient dynamics of all components of the electric vehicle (EV) into consideration. Further, a PSIM simulation platform is consequently developed in Chapter 4, to demonstrate the validity of this mathematical modeling.

The comprehensive vehicle model is a significant achievement in itself and goes well beyond the complexity of the models adopted in the literature to analyze HEV/EV powertrain architectures. The vehicle model was parameterized to match a prototype electric vehicle under development by the industrial partners including the two-speed transmissions. Performance tests and driving cycles were simulated to compare the benefits of the single-speed and two-speed transmissions.

Chapter 4. Simulation Results and Hardware in-the-Loop Implementation

4.1 Introduction

In this chapter, simulation results that verify the viability of the One-Fits-All modeling approach adopted in Chapter 3 are presented. Two benchmark vehicles are used as case studies to investigate the effectiveness of the model. The first one is Nissan Leaf 2012 (NLEV) which is characterized by its maximum torque 280 N.m., its motor power 80 kW and its maximum speed 10390 rpm. It is worth mentioning that NLEV is a pure EV that incorporates a powerful structure that includes an Electric Motor, an inverter, a DC/DC converter, Li-Ion battery. This compact design of the high voltage unit resulted in a high power density. The second benchmark vehicle is GM Chevrolet Volt 2nd Generation plug-in hybrid electric vehicle (PHEV) that is used as a case study to investigate the general performance and the implementation of Hardware in-the Loop (HIL) to demonstrate the obtained results experimentally. The last section of this chapter is about motor selection for EV/HEV applications. A comparison between three induction motor based machines has been investigated and a conclusion about the optimum motor performance is introduced.

The efficiency map of Nissan Leaf Machine are shown in **Error! Reference source not found.**. The dimensions of the machine are obtained from the Oakridge reports [91], as well as slot/pole number, number of turns per coil, number of strands per hand, torque, efficiency information and system DC link voltage. The materials for stator, rotor iron, and permanent magnet, are applied to make sure the Nissan Leaf machine model can match the published performance information. Many trial and error simulations have been undertaken to build a FEA model in commercial software that can satisfy all the published performance data within 5% error.

Based on the torque-speed information of the Nissan Leaf machine, four representative points are selected to capture the key features of the torque-speed specification, referring to **Error! Reference source not found.**, the first coordinate point is 0rpm, 280 Nm, which shows the maximum torque at low speed region. The second coordinate point is 2100 rpm, 280 Nm, which is the maximum speed point to achieve maximum torque. The position of the third coordinate point is 3000 rpm, 254.65 Nm, at which the specified nameplate power of 80 kW maximum is reached. The fourth coordinate point is 10000 rpm, 76.4 Nm, 80 kW, which is the top speed point requiring torque at maximum speed. Following the motor efficiency map, the inverter efficiency map and combined inverter and motor efficiency map are shown in Fig. 4.5 and **Error! Reference source not found.** respectively. We can see that the combined inverter and motor can acquire 90% efficiency and above in a large operation region.

The Nissan Leaf machine design adopts a full pitched integer slot, single layer, distributed winding with two neutral points joined via an interconnecting link. The detail winding connection is sketched according to the winding information and DC link voltage. For this three phase machine, there are 8 coils per phase and three possible connections, (i) 8 coils that are all serially connected, (ii) every 4 coils are serially connected to form a group and then the two groups are connected parallel, and (iii) every 2 coils are serially connected to form a group and the four groups are parallel connected. Combining the simulation results for each possible connection and the maximum 375V DC link voltage, it is deduced that the winding in the Nissan Leaf machine is connected every 2 coils in series and then the 4 branches connected in parallel to form each phase.

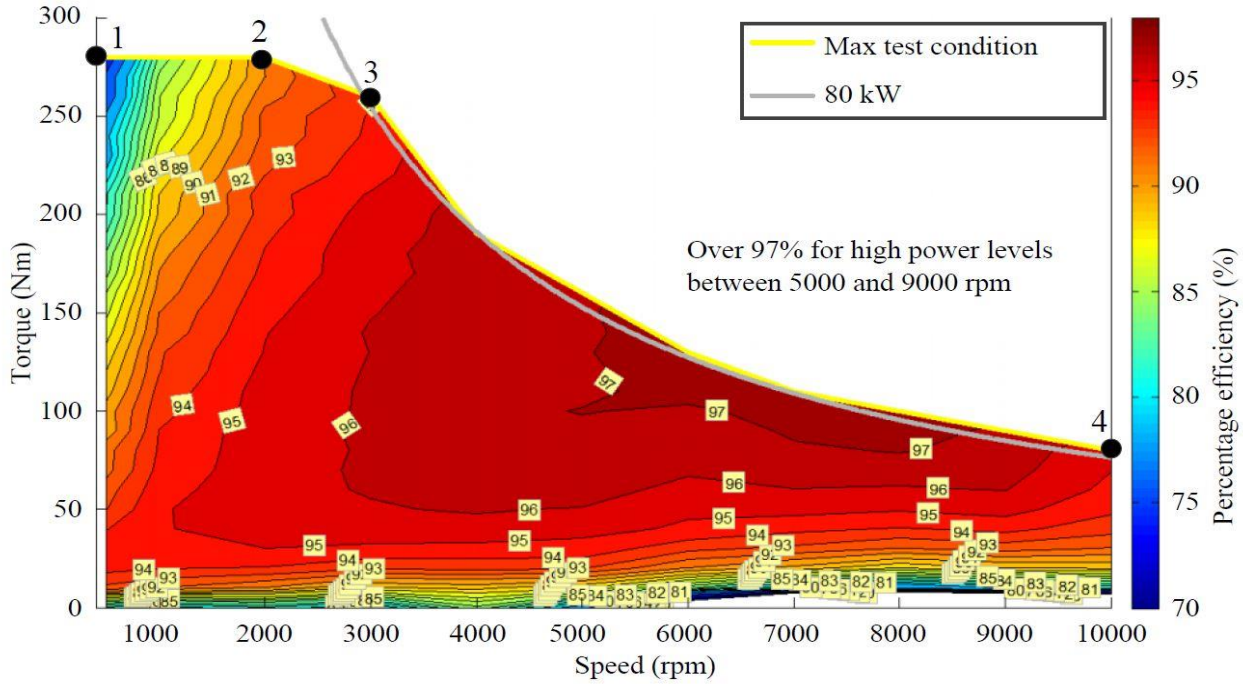

Fig. 4.1. Efficiency map of NLEV 2012 motor [121]

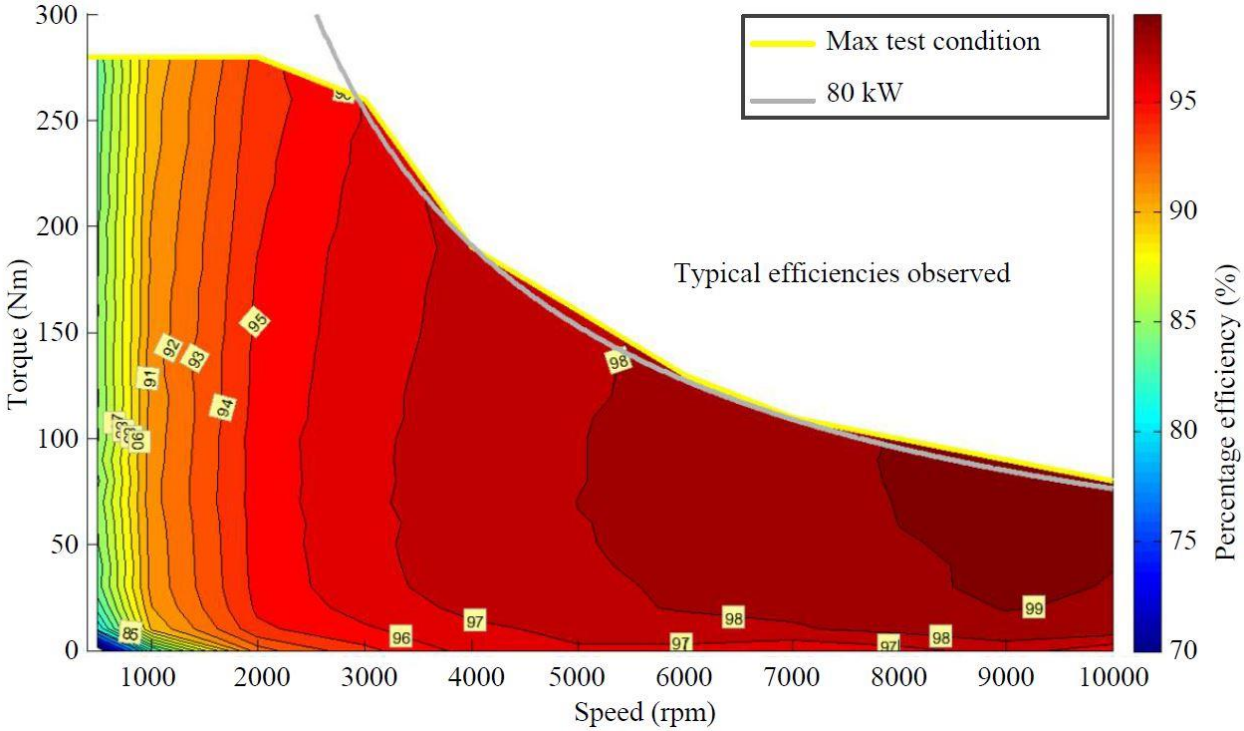

Fig. 4.2. Efficiency map of NLEV 2012 inverter [121]

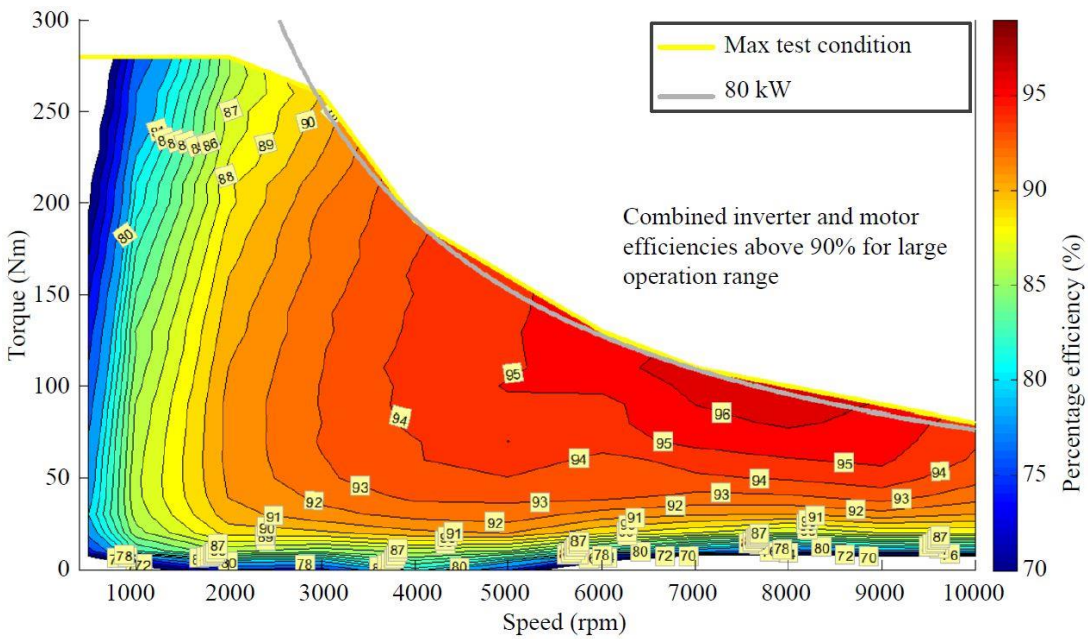

Fig. 4.3. Combined efficiency map of NLEV 2012 of motor and inverter [121]

A value of 200 N.m was considered as the load command on motor with no gears added; either for motoring or braking, per the assumptions section. This corresponds to a not fully loaded car, which is the normal operating case. At this loading, the motor efficiency is better than maximum torque. The curb weight of NLEV is 1500 kg whereas the Gross weight is 1945 kg.

4.2 Validation of Simulation Results

In order to validate the simulation results which are performed on PSIM platform, as a preliminary stage, an accurate data obtained from Oak Ridge National Laboratory and the US Environmental Protection Agency (EPA) has been compared with the simulation results to check the viability of the model. Then, as a main stage, a controller Hardware in the-Loop (Typhoon CHIL), which is the main focus here, is used to verify the results in real time since it provides a virtual vehicle that can emulate the same environment as a real passenger car. The host computer used for interfacing with the HIL system is a laptop of the following specs; Intel® Core ™ i7 – 6700 HQ CPU @2.60 GHz, 2592 Mhz, 4 Core(s). As the fully transient model adopted in this work requires a very small step time, the model

has been simulated on a 1-μs time-step initially to allow for operation at high switching frequency up to 400 kHz for testing wide band gap based power electronic converters adopted in this study.

4.3 Impact of Transmission Gear Selection

In this section, the impact of transmission gear ratios selection on a Nissan Leaf EV (NLEV) is investigated. The traditional single ratio gearboxes are replaced by multiple ratio ones. The choice of the gear ratio is proved to have a significant impact on electric vehicle's performance, range and chainage. Simulation model of a Nissan Leaf EV (NLEV) has been developed which is applicable for both single and multiple ratio transmissions to study this influence of different transmissions on Nissan Leaf performance. The simulation results reveal a significant effect on the overall efficiency due to integrating a transmission system with a NLEV. Comparisons are performed for both single and two-speed transmissions and results have been discussed.

Several literatures on EVs have focused on the batteries, energy management strategies, analysis [122] - [123]. However, there is a shortage in surveys which investigate the impact of transmission gear ratios design on EVs' motor performance. The usage of multi-speed transmissions for electric vehicles is expected to improve average motor efficiency and range capacity, or even can reduce the required motor size [124]-[125].

To study the influence of transmission ratios on electric vehicle (EV) performance, this study presents a detailed illustration of electric vehicle model, considering power flow through batteries, motor, transmission, and vehicle. The vehicle model can be used with single and two speed transmissions through a shifting mechanism, and the vehicle performance is studied for a range of drive cycle considerations. Simulation results will be used to evaluate the impact of ratio selection on useful motor torque, speed range, and vehicle performance [126],[127].

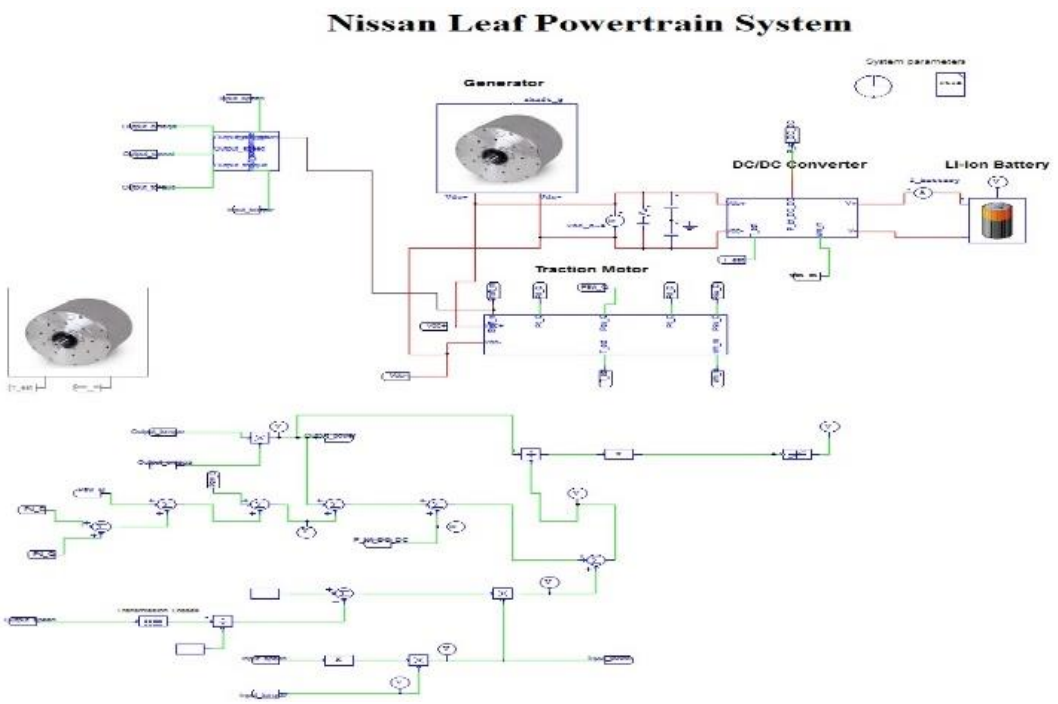

Fig. 4.4. Powertrain schematic diagram of the NLEV

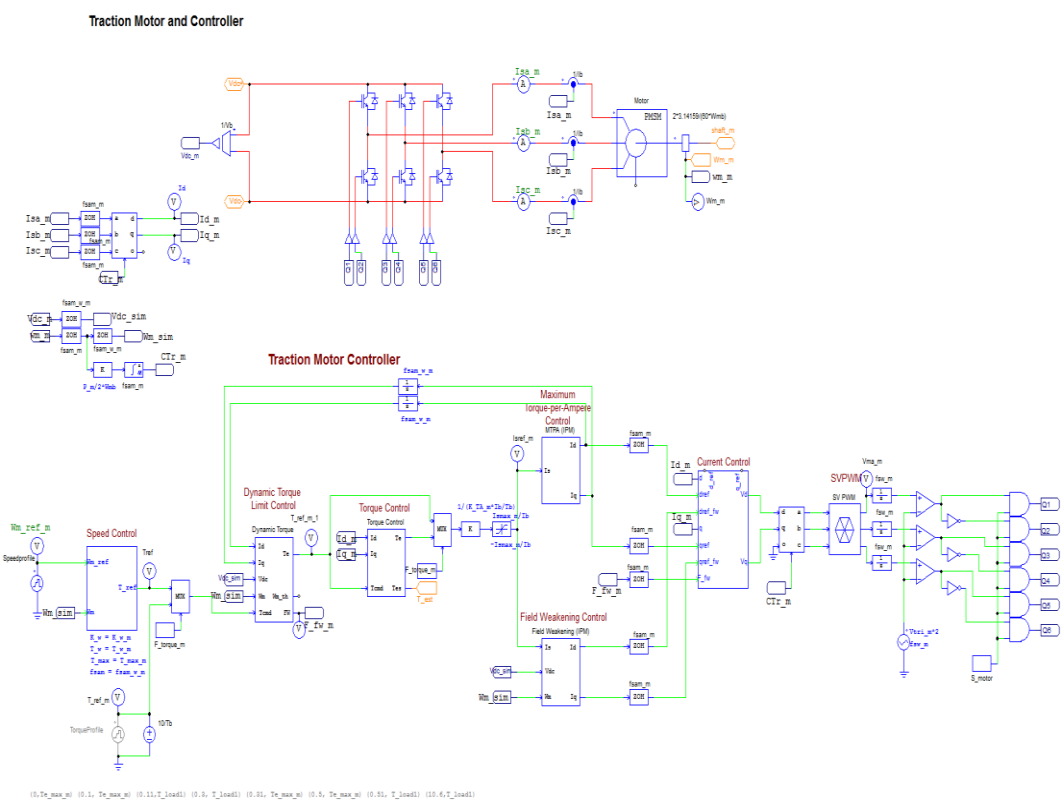

Fig. 4.5. Schematic diagram of the traction motor

Fig. 4.6 and Fig. 4.7 shows the abc 3-phase currents and the d-q currents respectively. Fig. 4.8 demonstrates the DC/DC converter losses and Fig. 4.9 depicts the losses in the inverter. It is assumed that there are no power losses in traction motor. Also the transmission system is equipped with a gear with a ratio 1:2. In practice, the gear ratio selection would be obtained automatically rather than manually but here, a simplistic gear selection strategy is used. In all of the following figures, power is measured in W, voltage in V and time in seconds.

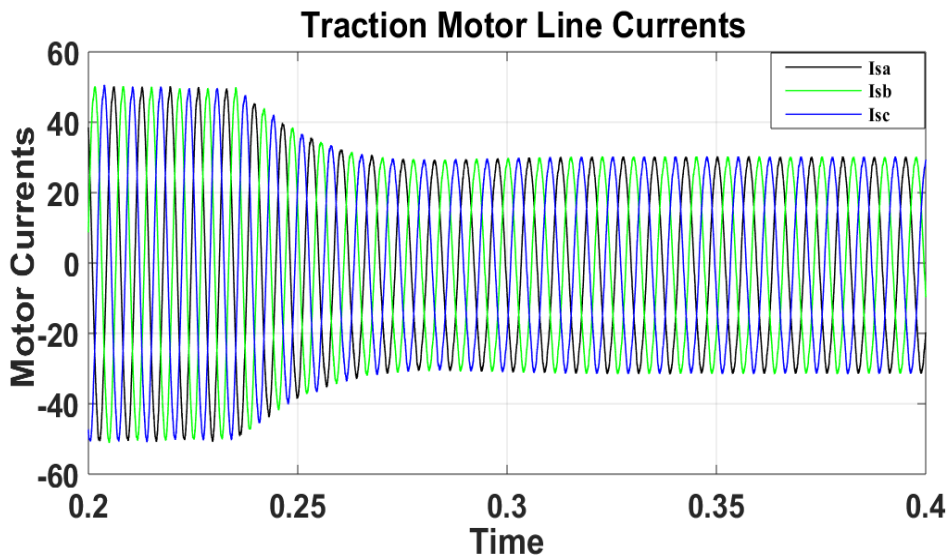

Fig. 4.6. Three phase currents of the traction motor

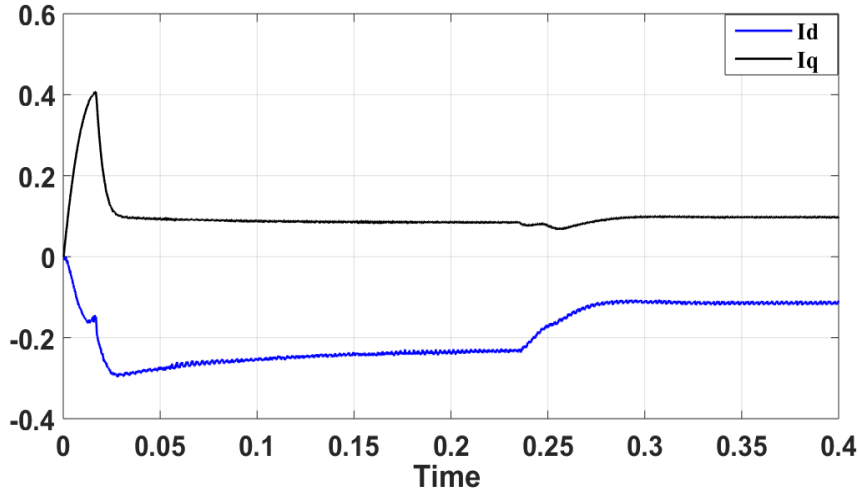

Fig. 4.7. Direct and quadrature axes currents

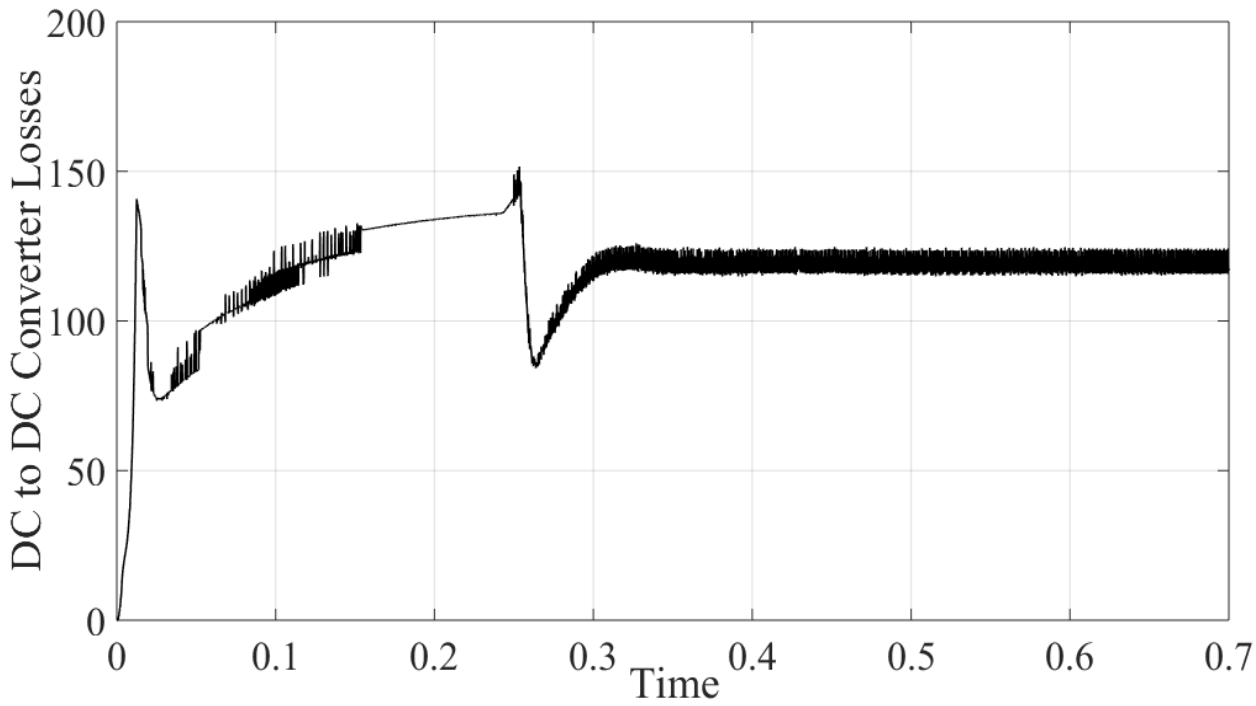

Fig. 4.8. Power losses inside the DC-DC converter

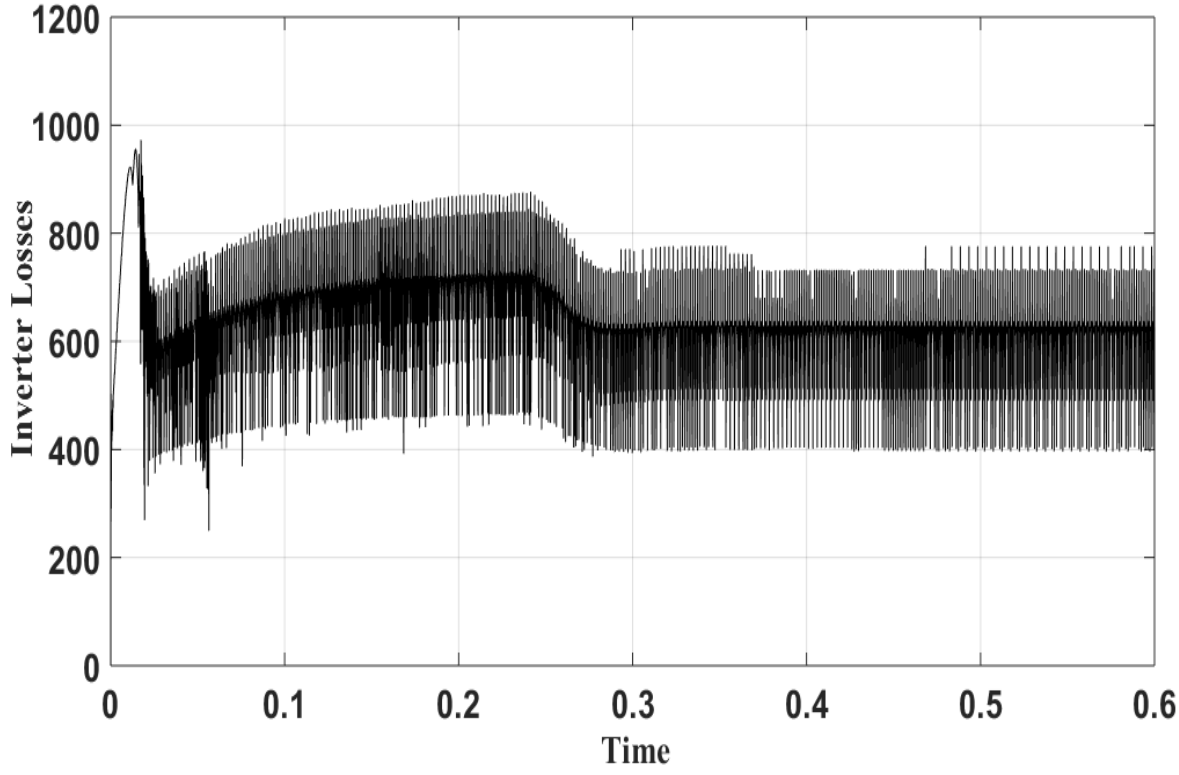

Fig. 4.9. Power losses in the inverter

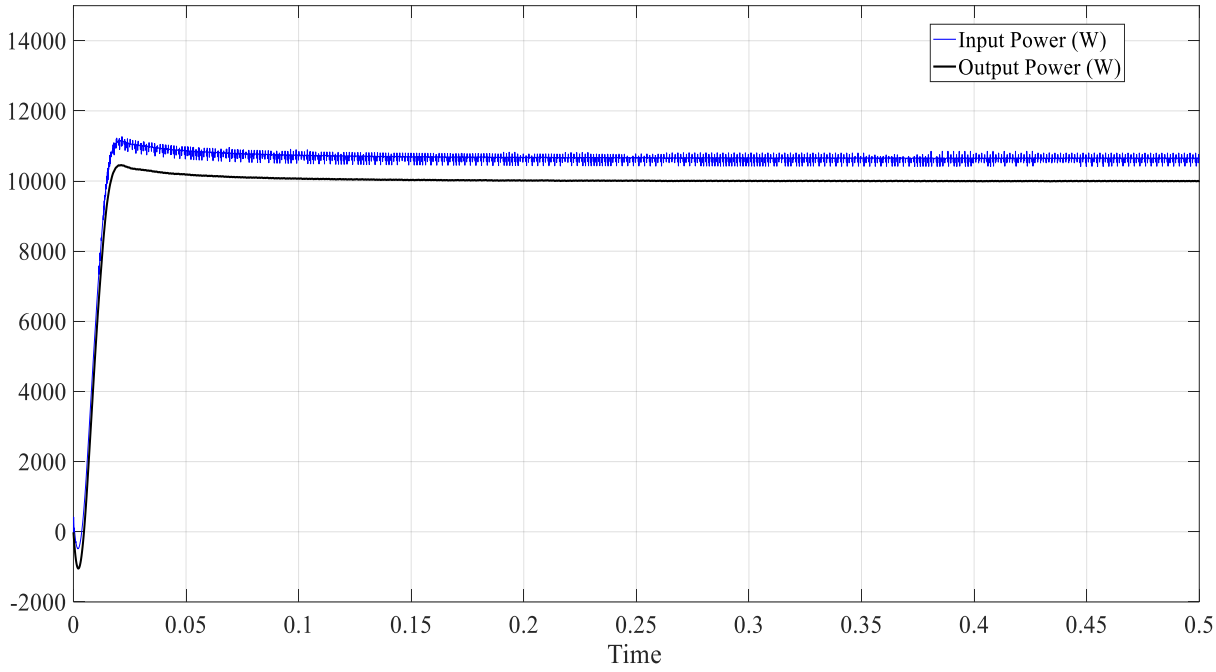

Fig. 4.10. Input and output power in case of lossless Transmission system

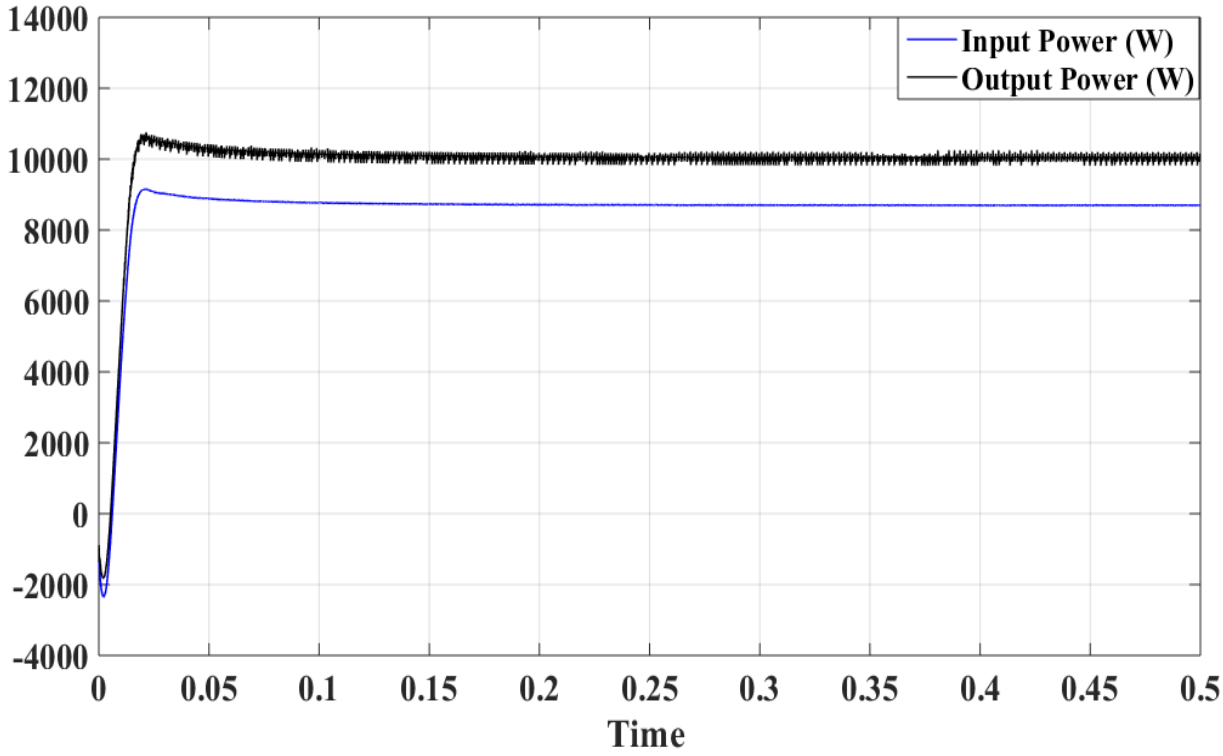

Fig. 4.11. Input and output power in lossy transmission system

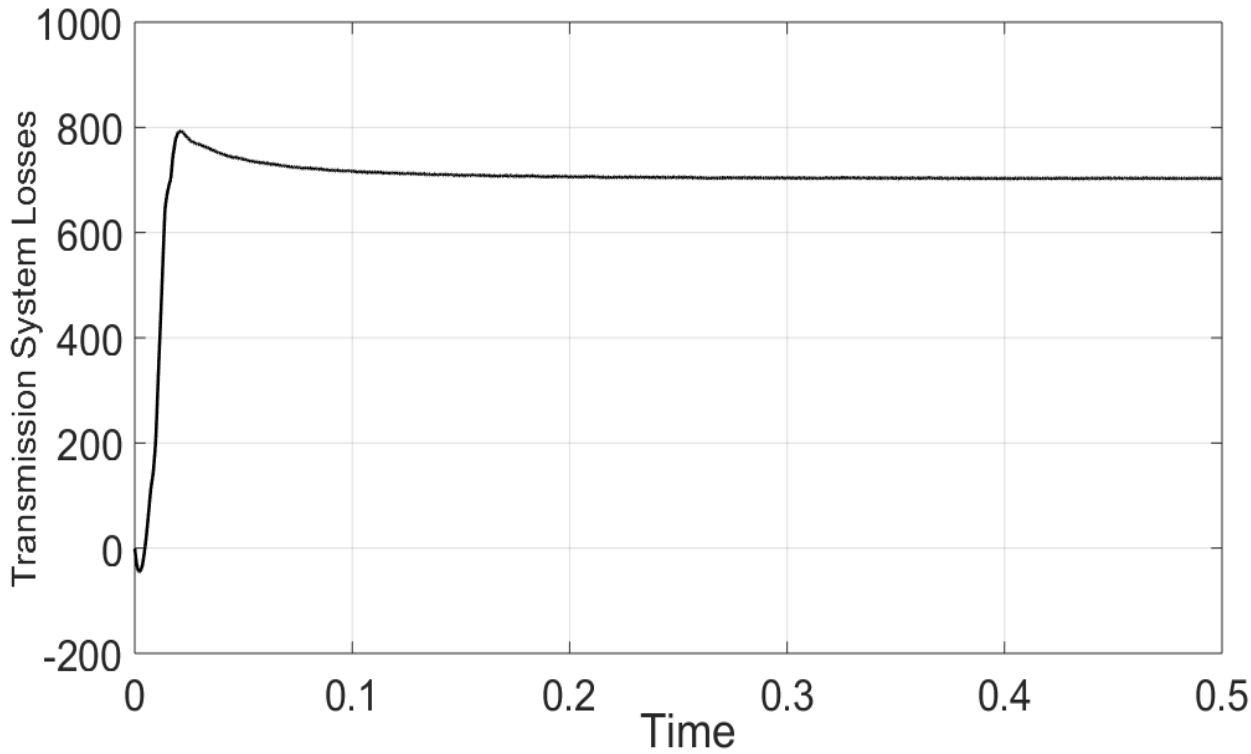

Fig. 4.12. Transmission system losses

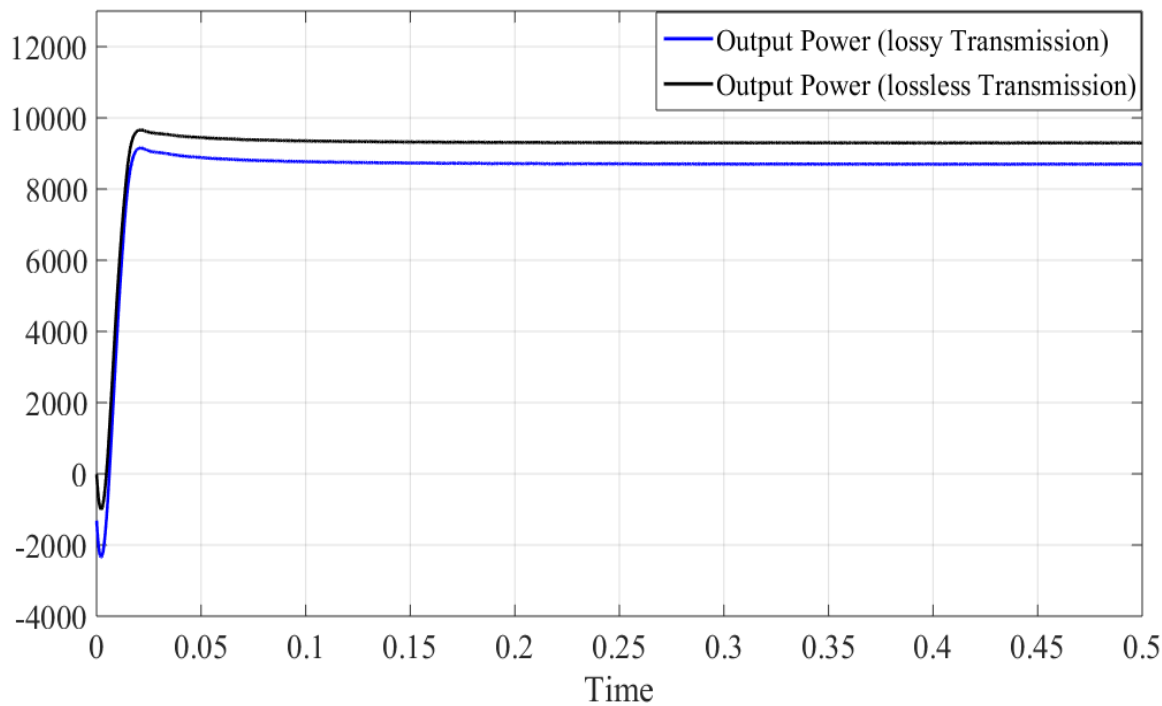

Fig. 4.13. Output power in transmission system

Table 4-1: Comparison between single and two-speed transmission

Performance	Single Ratio	2-Speed Ratio
Average Motor Efficiency	88.05 %	90.25 %
Top Speed (km/h)	110	205
Drive Range (km)	134	139

Table 4-1 compares the comprehensive performance of EV. Comparing with single ratio transmission, 2-speed transmission gives EV higher top speed than that of single EV. Moreover, when equipped with 2-speed, the average efficiency of motor is better than of that equipped with conventional 1-speed transmission.

4.4 General Performance Investigation

This section presents a novel platform for accurate mathematical modeling of the propulsion system of electric cars. It provides, for the first time, a Hardware in-the-Loop (HIL) real-time experimental verification case study of a GM Chevrolet Volt for power, control systems, and the mechanical systems. The contribution of this work can be categorized into three approaches; first, each component of the powertrain is accurately modeled taking transient dynamics of all components of the electric vehicle (EV) into consideration. Further, a PSIM simulation platform is consequently developed, to demonstrate the validity of this mathematical modeling. Finally, the Typhoon HIL, which will be discussed in detail in chapter 5, is used to provide the experimental verification of the proposed model in real-time, which precisely validate the viability of the model.

The main contribution objective here is to develop a generic versatile platform to successfully model HEVs /EVs. The model is mathematically developed and simulated using PSIM software package. A case study using real data of GM Chevrolet Volt is adopted as a benchmark to demonstrate the model viability. The energy performance of the Chevy Volt can be evaluated in

three different areas: (i) propulsion system, (ii) battery charging and discharging control, and (iii) the vehicle mechanical design [128], [129]. The second generation of vehicles included Chevy Volt have achieved improvements in all of the aforementioned areas. Those performance enhancements made the Chevy Volt 2nd Generation to be a cost efficient and fuel savvy vehicle. The propulsion system of any HEV consists of two main machines where one of them works most of the time as a motor and the other operates as a generator that is being driven by a combustion engine [130]. The propulsion system of the Chevy Volt, in particular the PHEV version, is quite sophisticated and that was one of the major motivations for selecting this car as a case study for this work where designing and implementing its model will facilitate for more achievements in enhancing the performance of any powertrain of other vehicles. The HEV version is more inclusive to the EV version, when it comes to modeling. This is the main reason behind selecting this version [131].

To meet the demands of the Chevy Volt extended range, the battery pack was increased by 12% by including an additional cell to the old design resulting in three cells instead of two. However, the battery mass was reduced by 7% to 183 kg compared with 197 kg in the 1st Generation [119], [132].

Fig. 4.14 shows the general schematic of GM Chevrolet Volt whilst the implementation proposed model is depicted in Fig. 4.15 that has been tested on PSIM. The simulation results of the 3-phase line currents are shown in Fig. 4.16 that show nearly sinusoidal waveforms in the zoom-in view. The PMSM rotor speed shown in Fig. 4.17 is shown to be constant at 2014 rpm while the average value of the vehicle torque displayed in Fig. 4.18 is 54 N.m. The torque/speed characteristics are shown in Fig. 4.19.

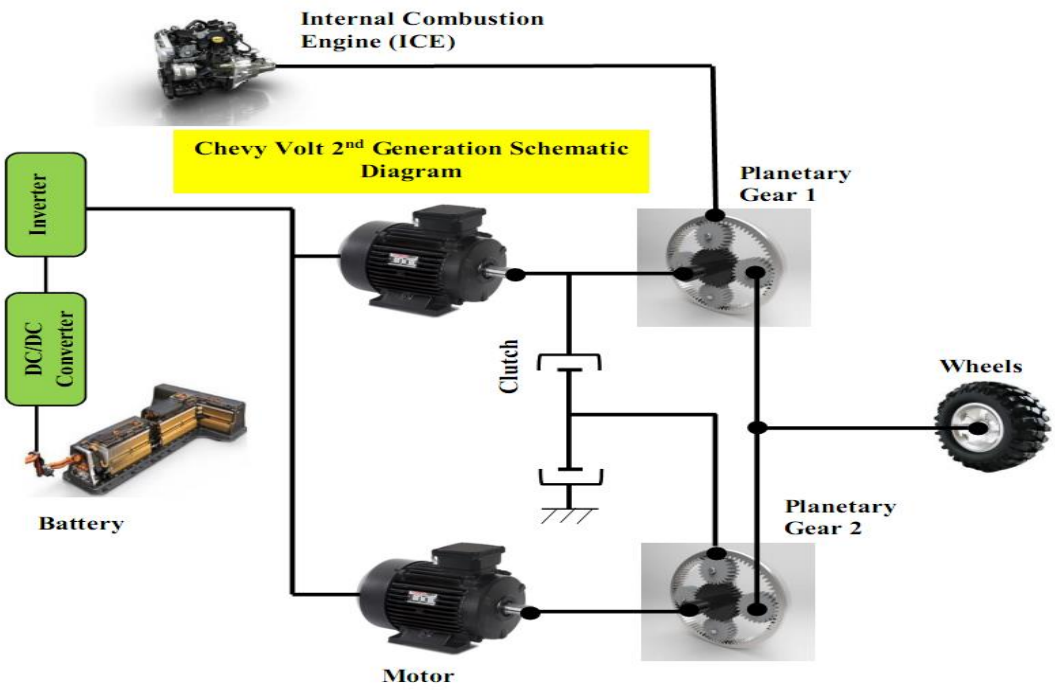

Fig. 4.14. Powertrain schemtatic of the GM Chevrolet Volt [107]

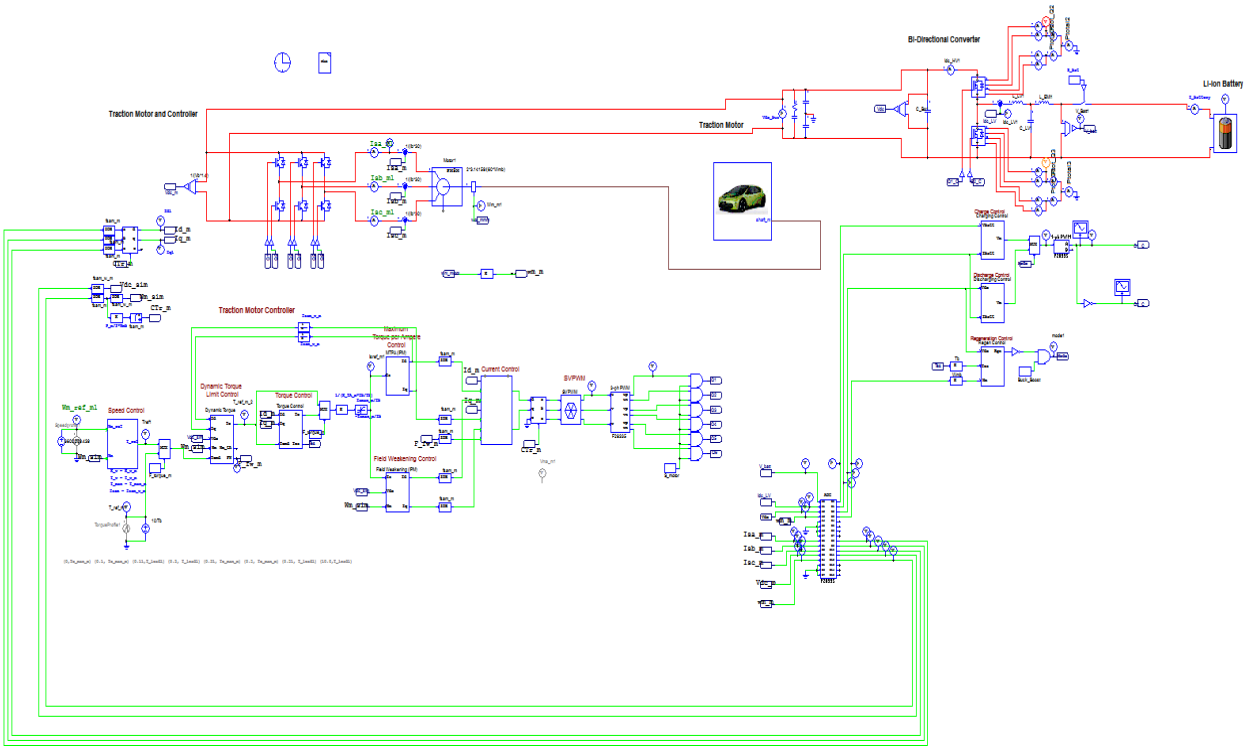

Fig. 4.15. Schematic diagram of the of the HEV in PSIM [107]

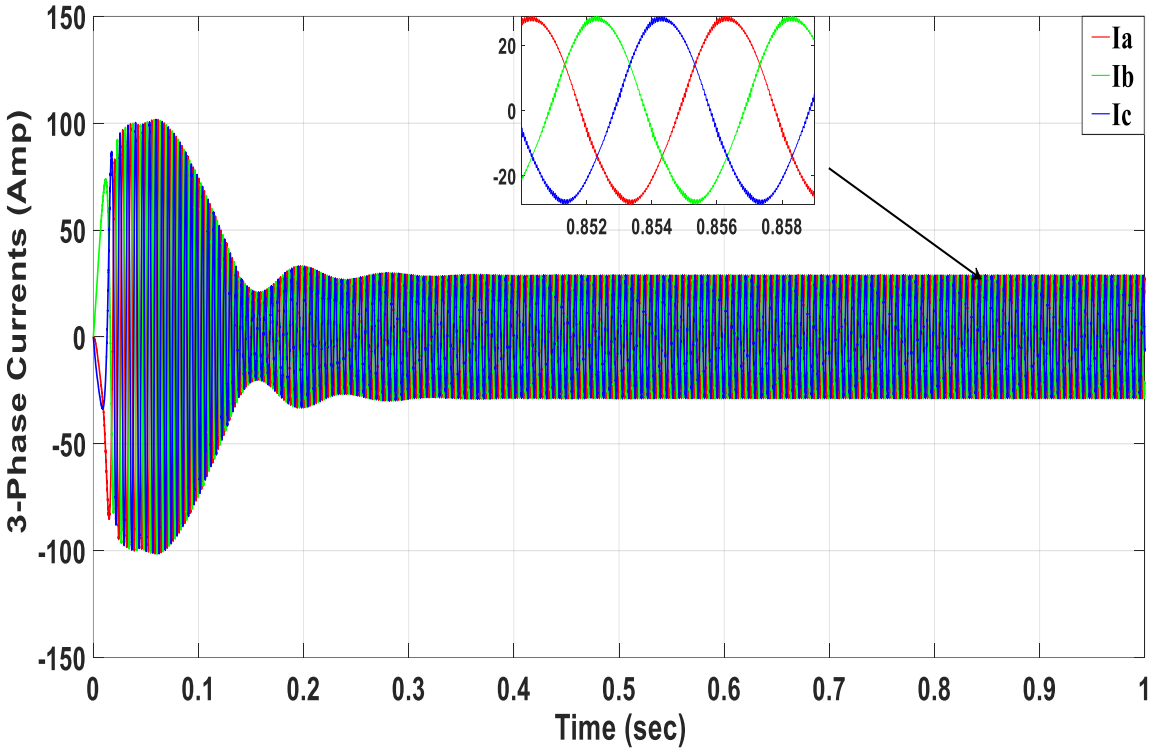

Fig. 4.16. 3-ph current waveforms for the stator of the PMSM

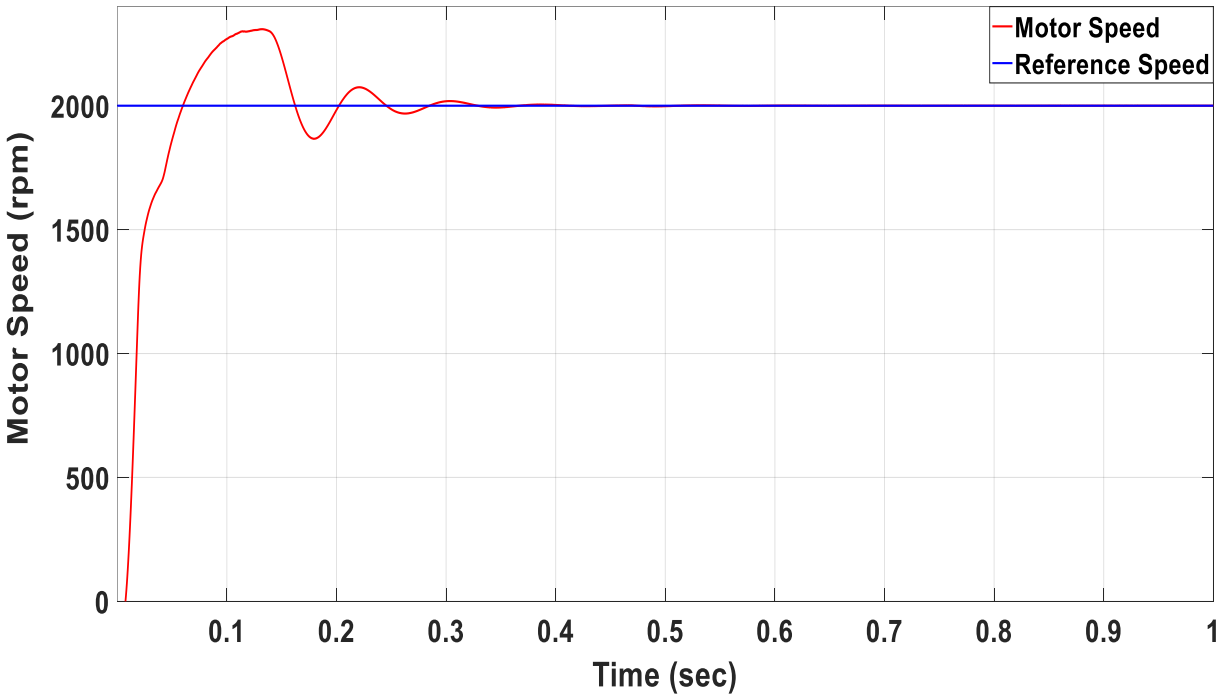

Fig. 4.17. Speed controller response

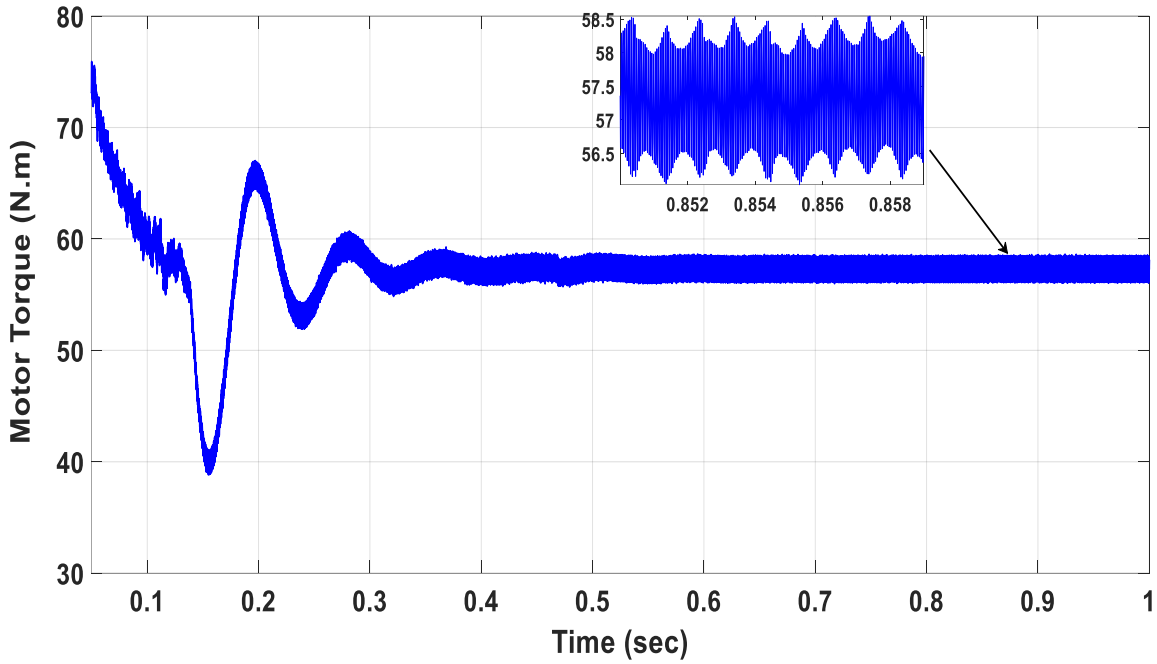

Fig. 4.18. Torque produced in the PMSM

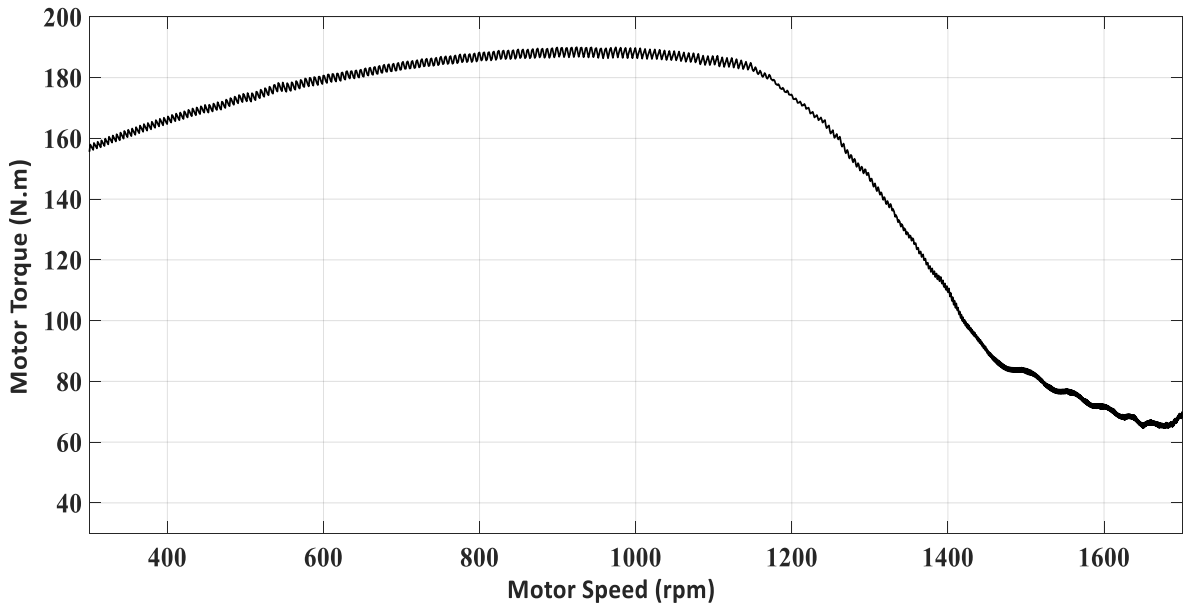

Fig. 4.19. Torque-speed characteristics of the PMSM

The Battery SOC, is a percentage representation of the energy capacity contained within the battery module [133], [134]. In Fig. 4.20, the waveform represents the SOC during dual PMSM

mode. It shows a decreasing SOC which indicates that the vehicle is drawing current from the battery for the dual PMSM. Fig. 4.21 shows the battery voltage, which has a small ripple in steady-state condition.

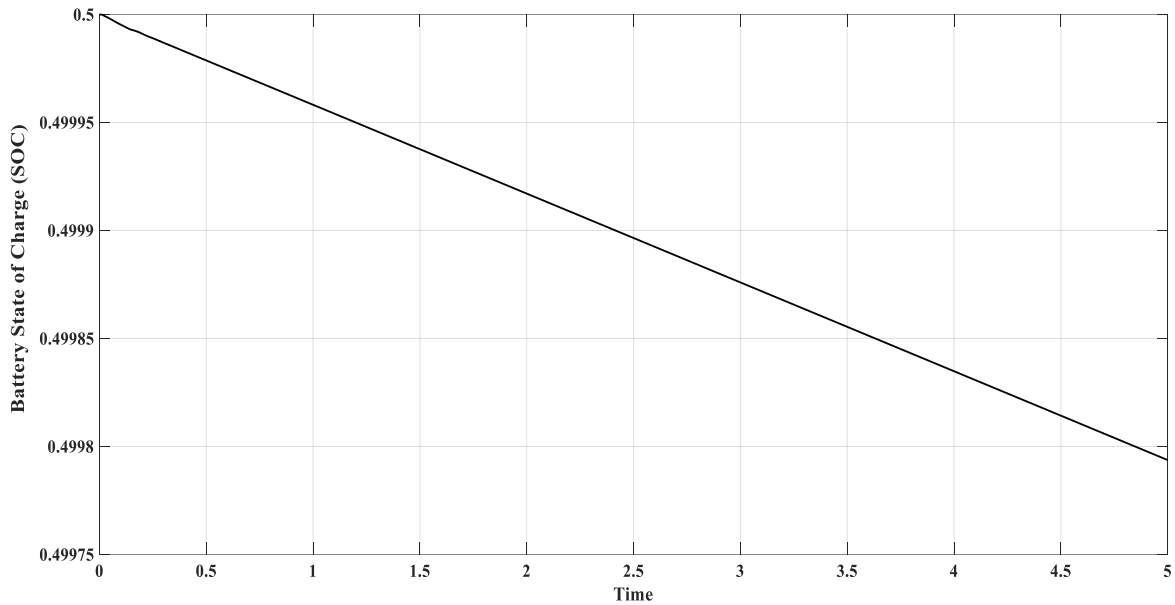

Fig. 4.20. State of charge graph of the battery

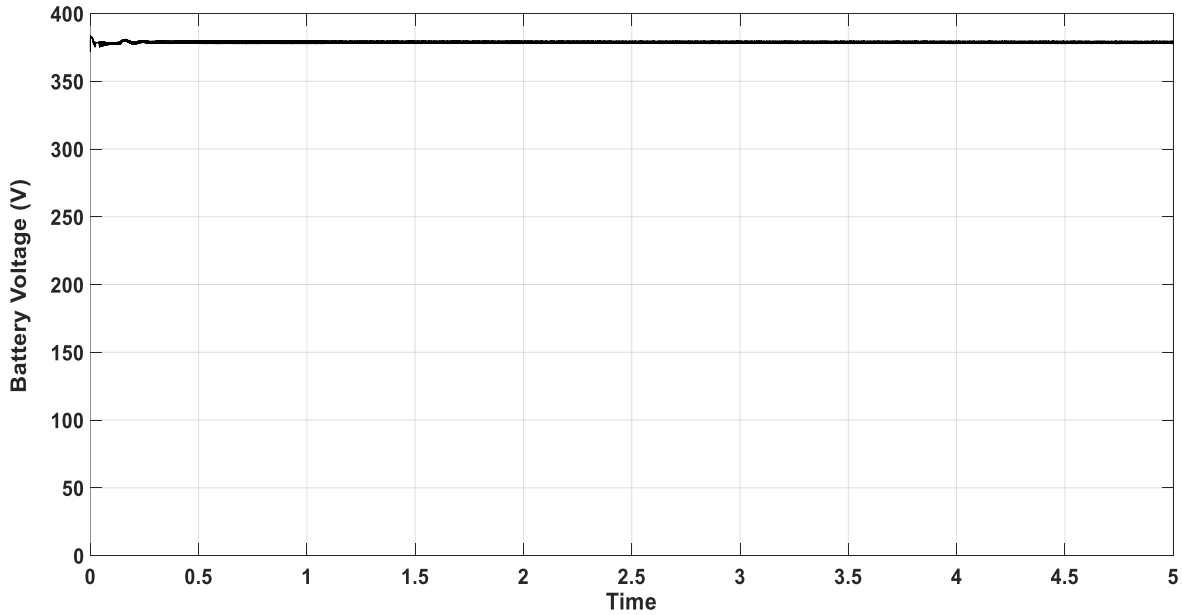

Fig. 4.21. Waveform of the battery voltage

The battery current shown in Fig. 4.22 is negative, which indicates that the flow is away from the battery going to the inverter circuit. Fig. 4.23 displays the DC Bus voltage in the motoring mode.

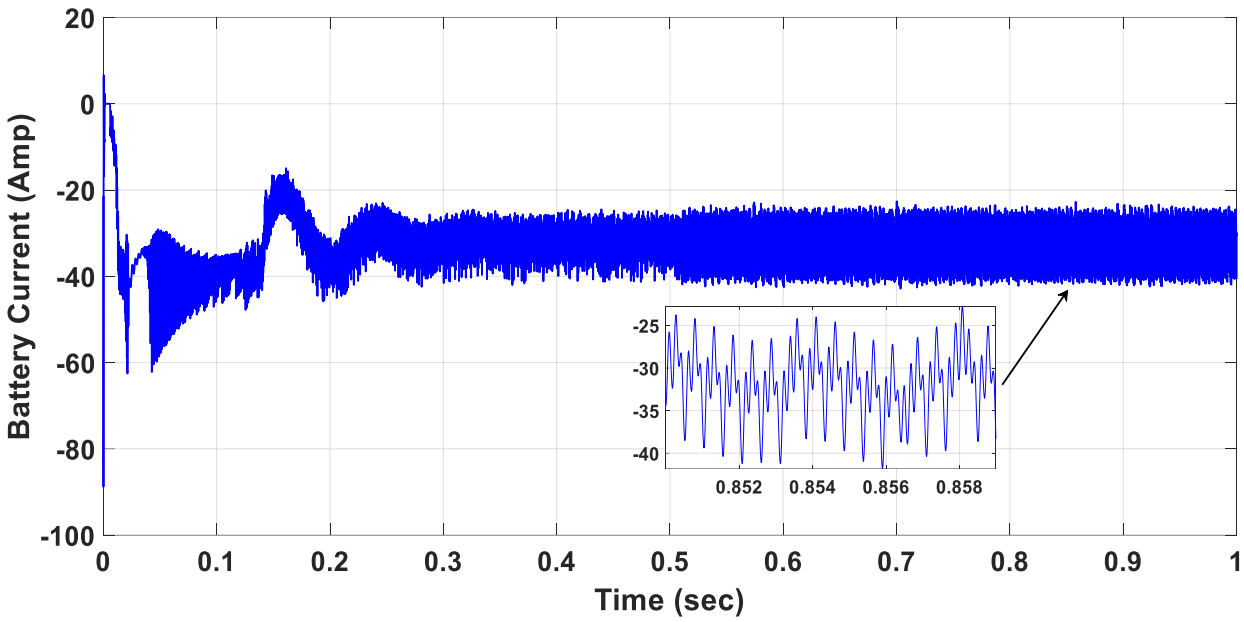

Fig. 4.22. Waveform of the battery current

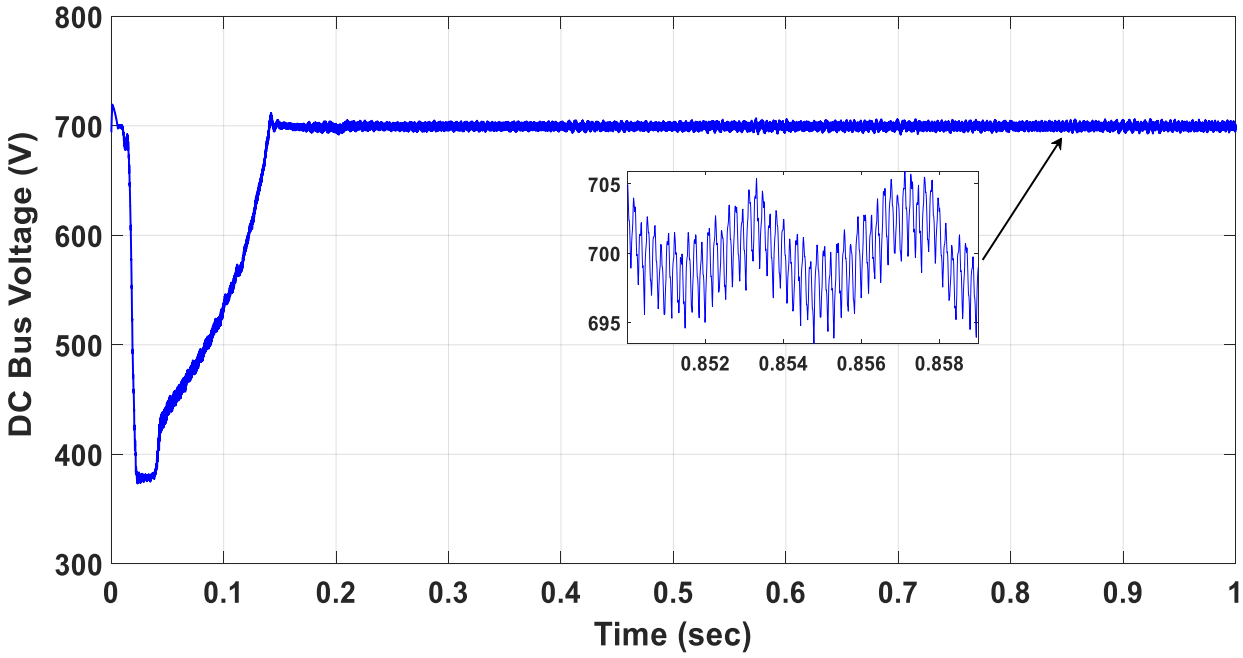

Fig. 4.23. Waveform of the DC bus voltage

The fluctuations of the DC bus capacitor current shown in Fig. 4.24 depict the EV suspension main characteristics that reflect the fact that the system is receiving and delivering power. The PWM firing of the one leg of the IGBTs of the traction inverter can be seen in Fig. 4.25.

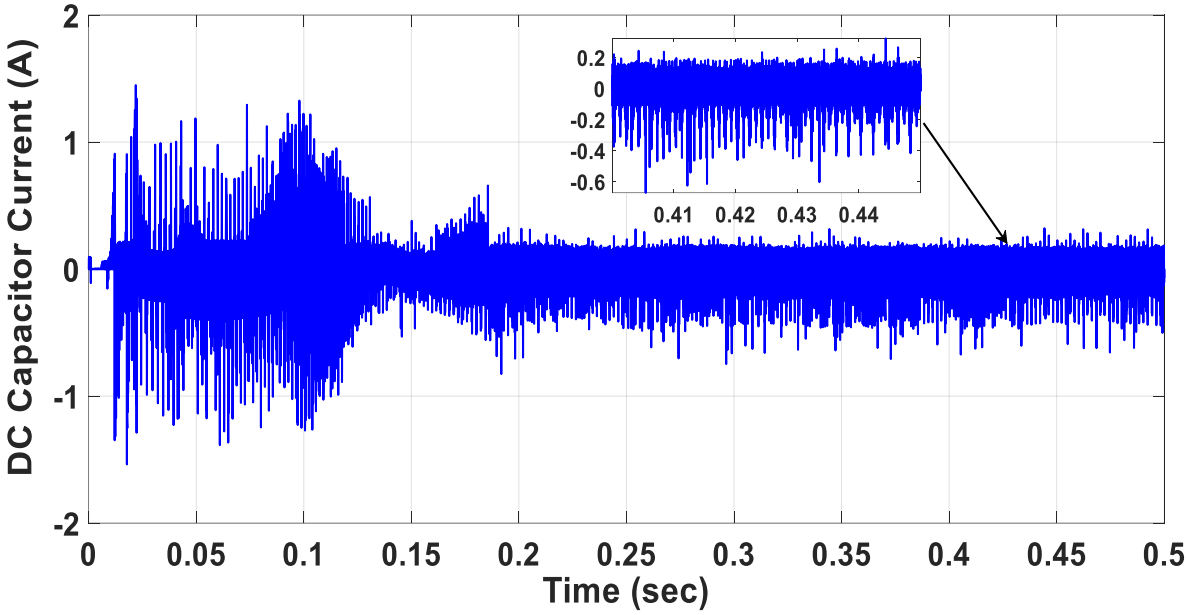

Fig. 4.24. Waveform of the current passing through the DC bus

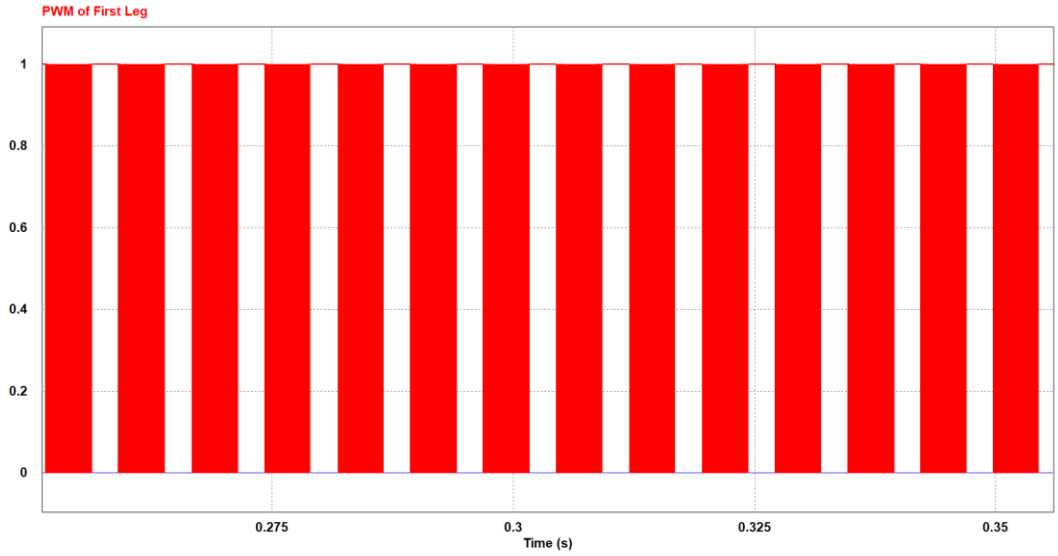

Fig. 4.25. Waveform of the pulse width modulation for the IGBTs

4.5 Hardware in-the Loop (HIL) Experimental Verification

HIL technology is used to prototype and test the proposed control system while simulating the power circuit on the HIL module platform. The Permanent Magnet Synchronous Motor (PMSM) and the Power Electronics hardware components are simulated in real-time at which the parameters can be changed during the simulation. However, the control algorithm is generated as a C code and downloaded to the TI controller that exists on a Digital Signal Processing (DSP) board. The results from the simulation based on PSIM environment and hardware validations using HIL are in agreement, which validates the developed model. The performance has been investigated under different load operating conditions in real-time to verify its robustness. The case study can be extended for any electric car as it provides a generic platform for modeling any propulsion system. The HIL verifies and tests the control algorithms in real time through virtualizing the vehicle hardware. Saving cost and time with high fidelity, the HIL technology affords a method by which the vehicle model can be investigated under a variety of realistic potential scenarios [97], [98].

The HIL topology used in this work is shown in Fig. 4.26 whereas Fig. 4.27 depicts the interface between power and control circuits [135]. The HIL, used in this work, consists of the main module HIL402 and the Digital Signal Processor (DSP 100) and the TI controller (TMS320F28335).

The processing power of the DSP controller allows the accurate control of power converters. Therefore, it provides an appealing solution for design validation. It is important to mention that this is the first time that the Typhoon HIL is used in automotive design research applications. This adds more depth to the novelty of the proposed work. Typhoon HIL is widely used for smart grid applications but this work proves its capacity to include new areas of research. One of the main objectives of the proposed work is to implement the HIL testing on the GM Chevrolet Volt

simulation model and verify the simulation results obtained with PSIM.

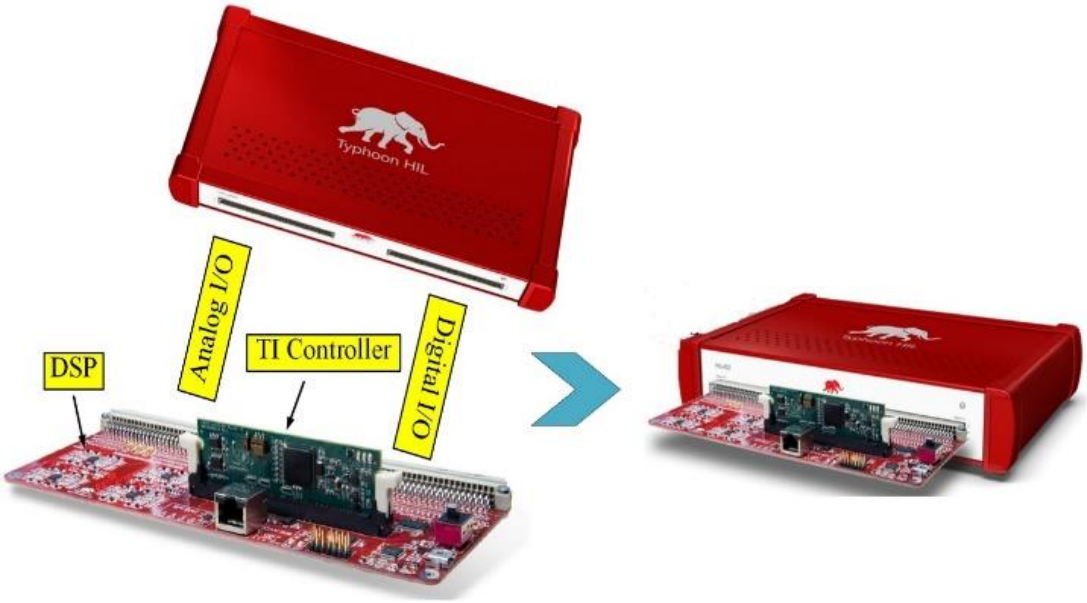

Fig. 4.26. Topology of the HIL controller

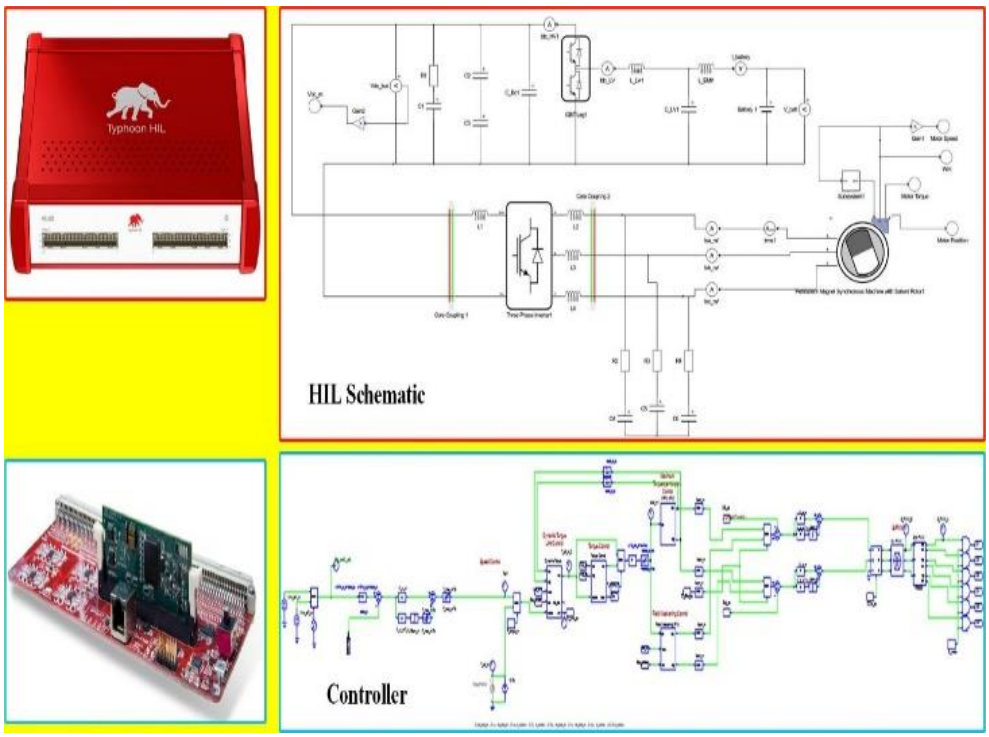

Fig. 4.27. Power and control schematics implemented on the HIL platform

Hardware-in-the-Loop (Typhoon HIL) simulation systems provide such a “virtual vehicle” for system validation and verification [136], [137]. The HIL system consists of the powertrain loop while the control loop is simulated in the computing platform on PSIM and the link between the two circuits is via the Analog to Digital converter (TI FX28335 ADC). The controller behavior can be validated at various environmental conditions and the controller robustness can be tested by introducing powertrain component and subsystem malfunctions. With HIL, we can identify and resolve problems earlier in the development cycle. There are some requirements for the HIL implementation that should be satisfied in order to ensure accurate results. These requirements include that the system should have fidelity so that the controller malfunctions are only triggered with the same settings as in the vehicle. An interface with the controller physical signals should be provided to enable modifications when required [138]. The schematic and the controller are shown in Fig. 4.28 and Fig. 4.29.

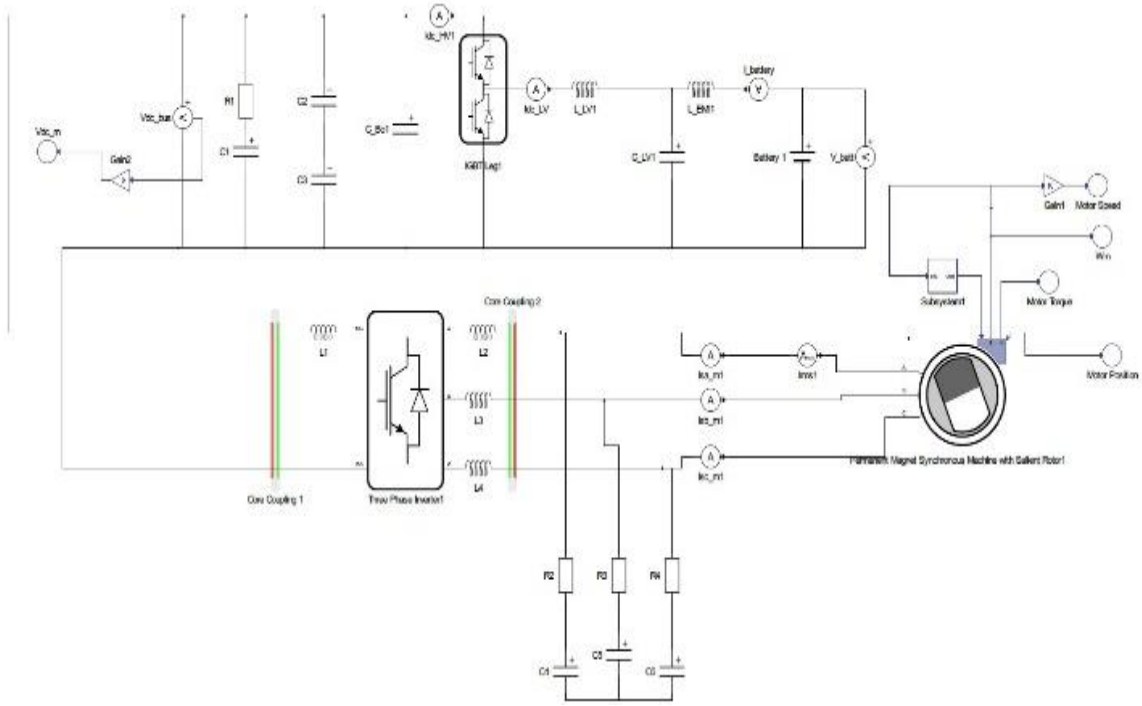

Fig. 4.28. Power circuit schematic implemented on HIL platform

Fig. 4.30 shows the HIL set-up which contains the HIL module, the oscilloscope and the HIL power circuit model on Typhoon HIL software. The control circuit code is generated from PSIM and converted to C code using Code Composer Studio software then downloaded on the TI controller.

The Typhoon HIL plays a role of an interface between power circuit and the downloaded control code. Fig. 4.31 shows the HIL results panel obtained after 5 seconds of running the simulation. Fig. 4.32 to Fig. 4.37 show the HIL results correlate to a high degree with the PSIM simulation results. In order to calculate the real measurements, the HIL scale should be multiplied by the oscilloscope scale times the number of divisions. This proves the sound accuracy of the developed model.

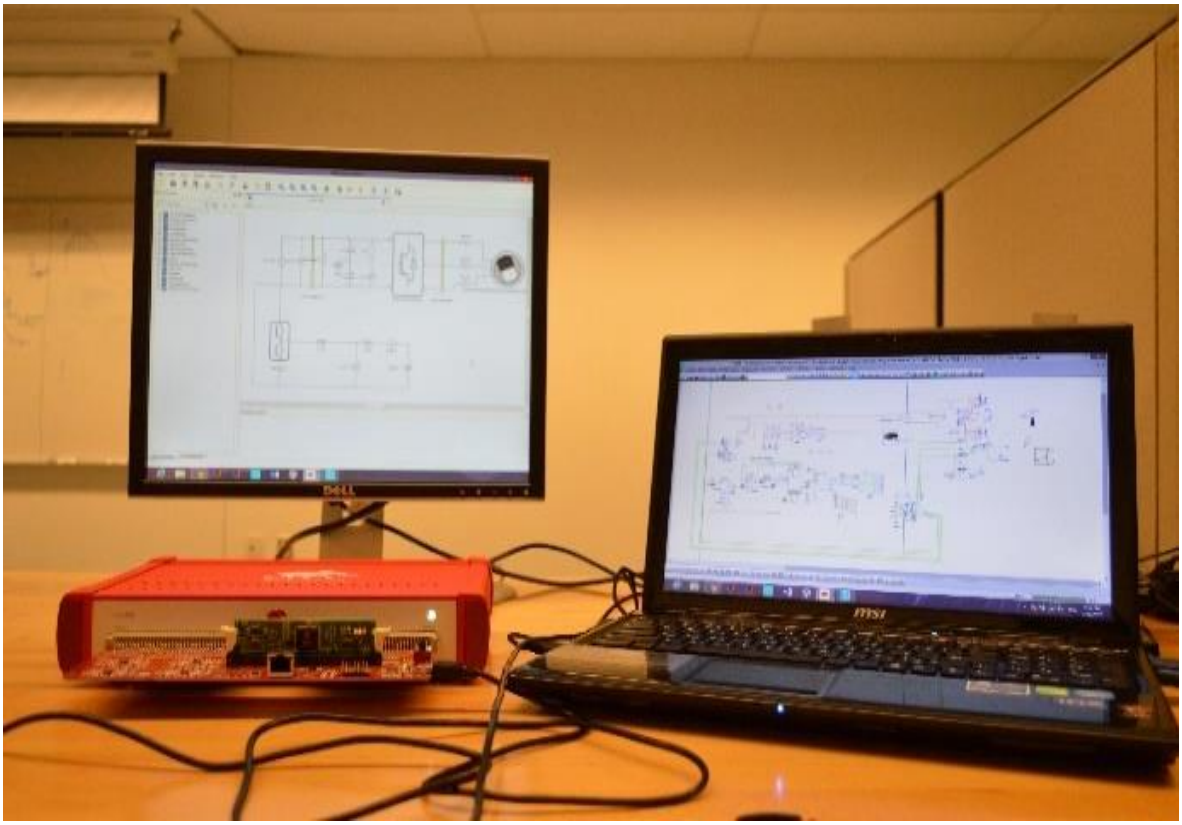

Fig. 4.29. Interface between PSIM simulation and HIL controller

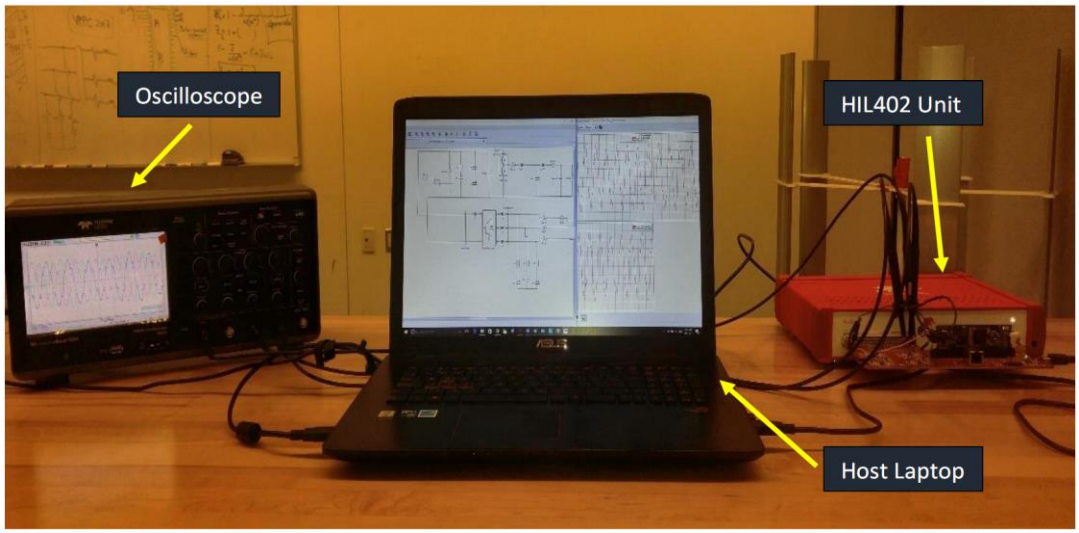

Fig. 4.30. Test bench setup of the hardware-in-the loop

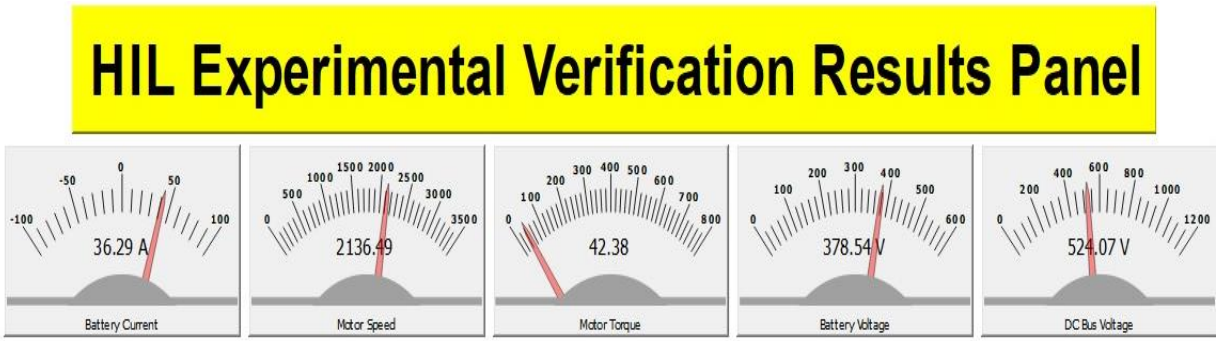

Fig. 4.31. Real time values of the HIL simulation dashboard

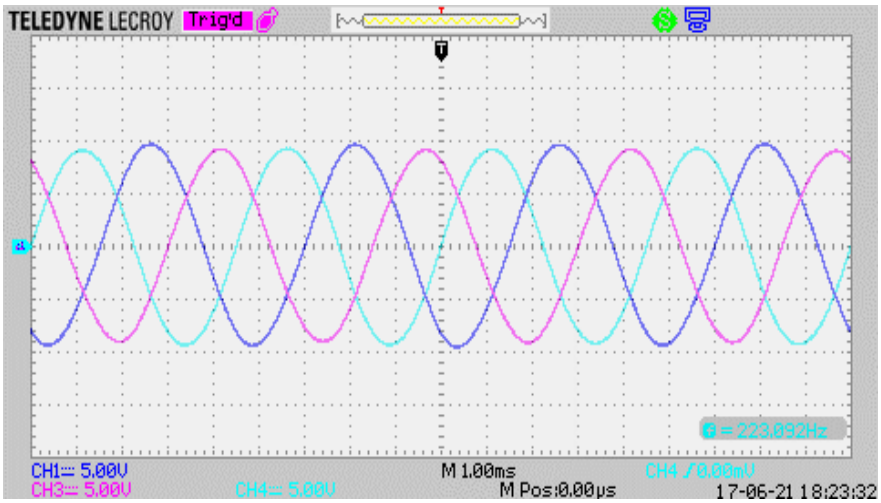

Fig. 4.32. 3-phase waveforms of the PMSM currents (5A/div) (HIL Scale 1:8) [Value: 38A]

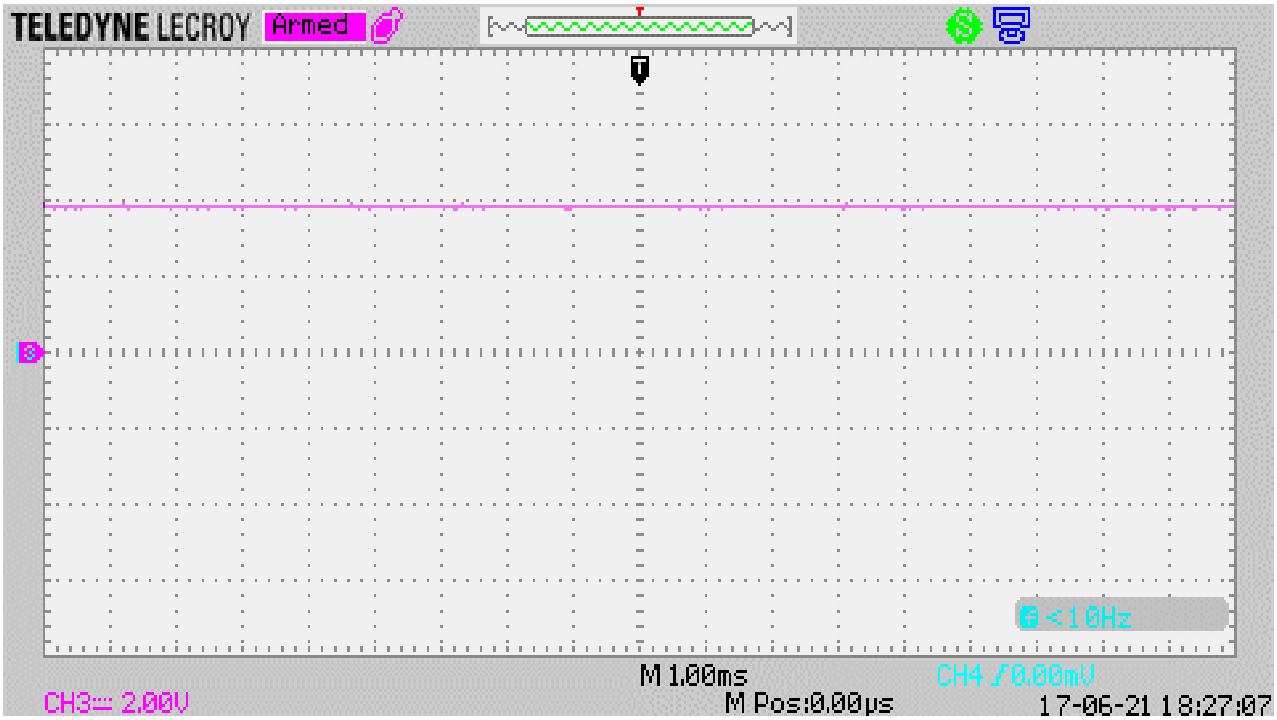

Fig. 4.33. Waveform of the battery voltage (2V/div) (HIL Scale 1:100) [Value: 379V]

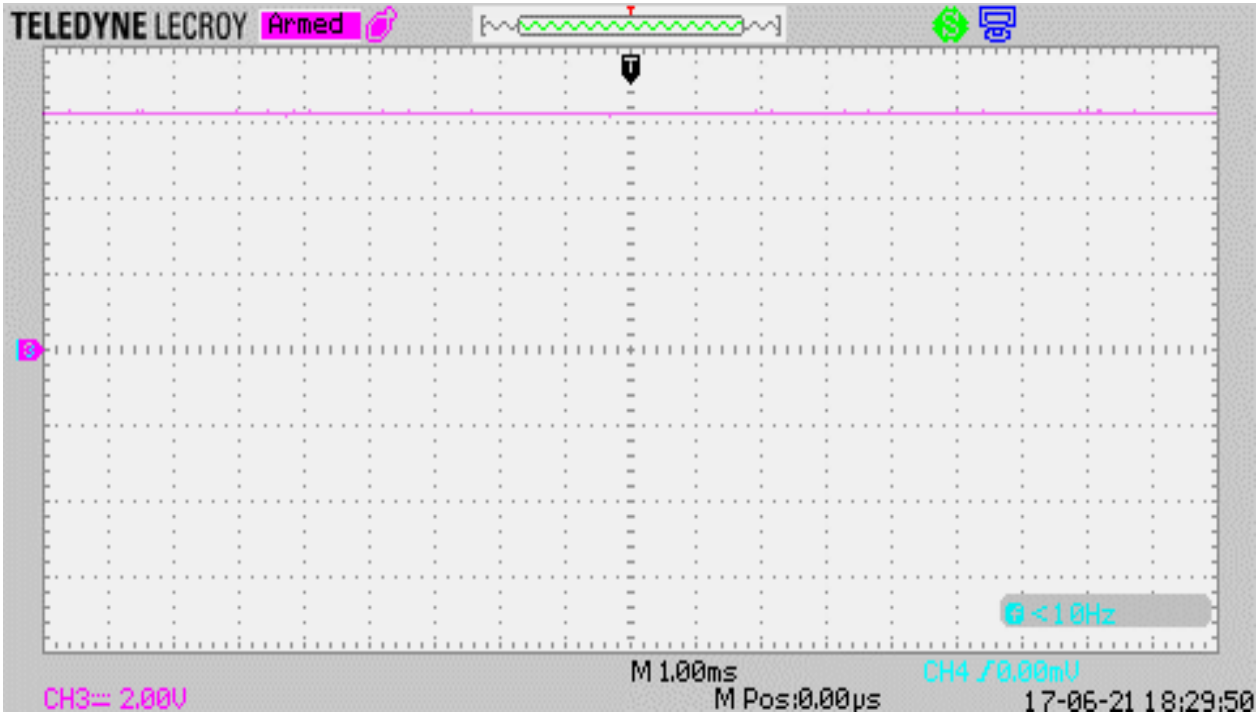

Fig. 4.34. Waveform of the DC bus voltage (2V/div) (HIL Scale 1:100) [Value: 630V]

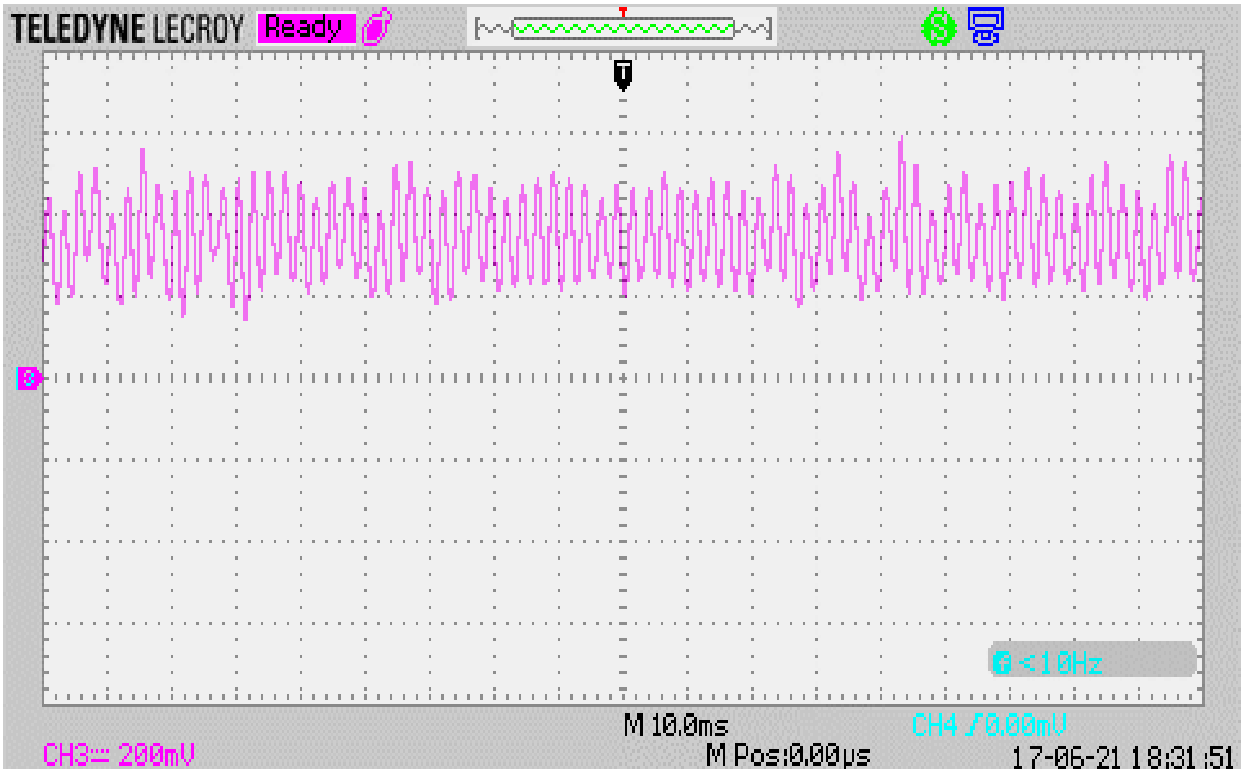

Fig. 4.35. PMSM produced torque (200 N.m/div) (HIL Scale 1:100) [Avg. Value: 57 N.m]

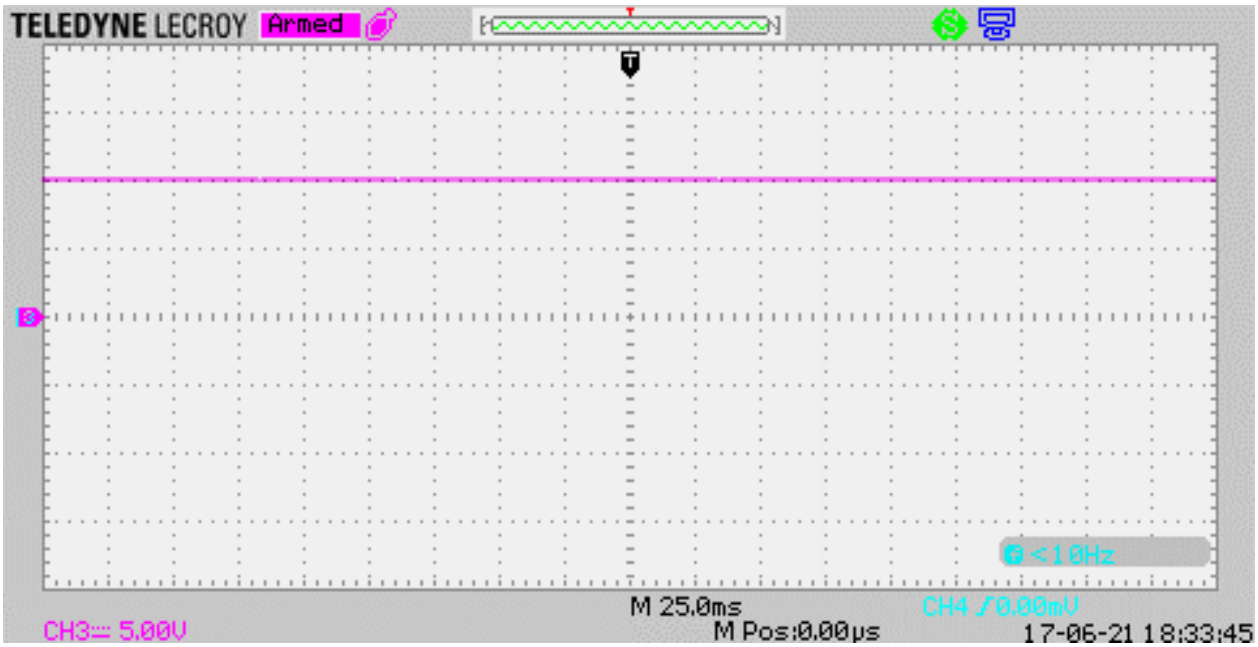

Fig. 4.36. Speed of the permanent magnet synchronous motor (5 rpm/div) (HIL Scale 1:200) [Value: 2010 rpm]

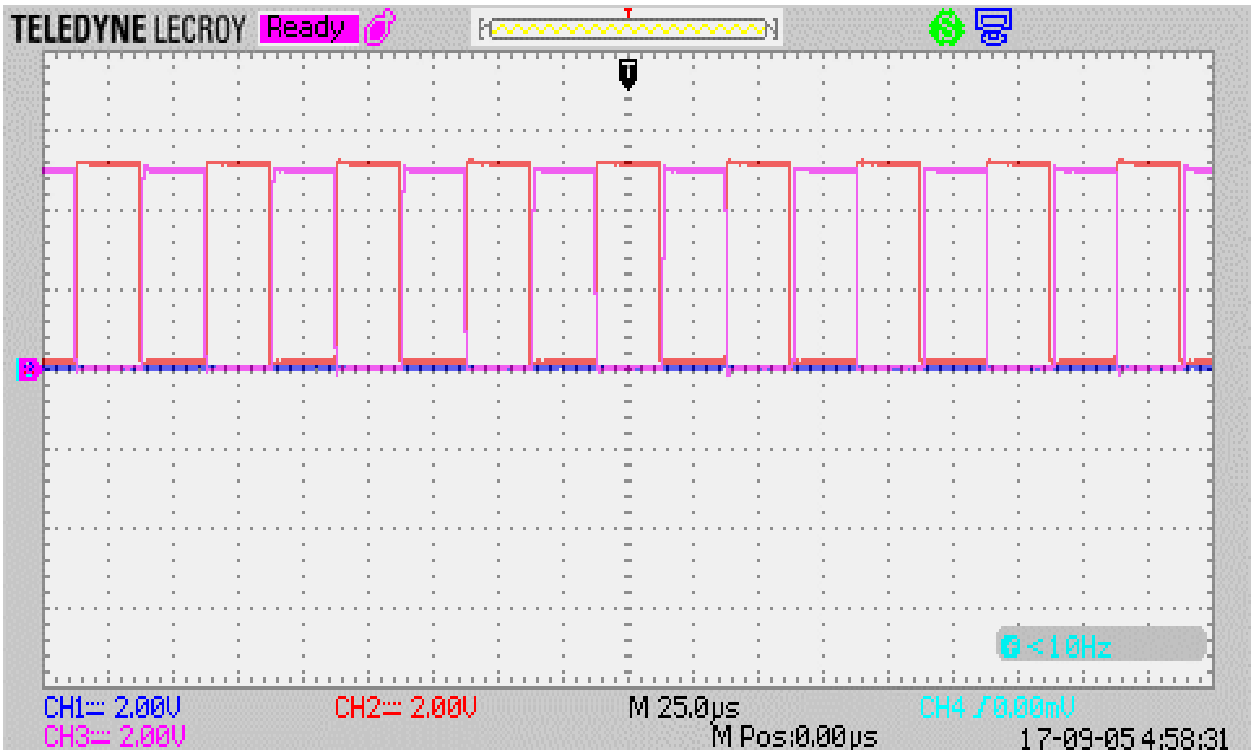

Fig. 4.37. Pulse-width modulation waveform of the IGBTs

For the purpose of making a comparison between what we obtained from the simulation results and the results obtained from the Typhoon HIL. Fig. 4.38 depicts the motor torque achieved from the simulation results, shown in red, in comparison with the motor torque output extracted from the Typhoon HIL module. It can be shown that the torque is oscillating in the beginning then settled to a normal average value of 57 N.m. The average value is obtained directly from the HIL module at steady state as the time of the transient period is too small to be captured. Also, in Fig. 4.39, the engine speed is being compared in order to verify the mechanical modeling and its performance.

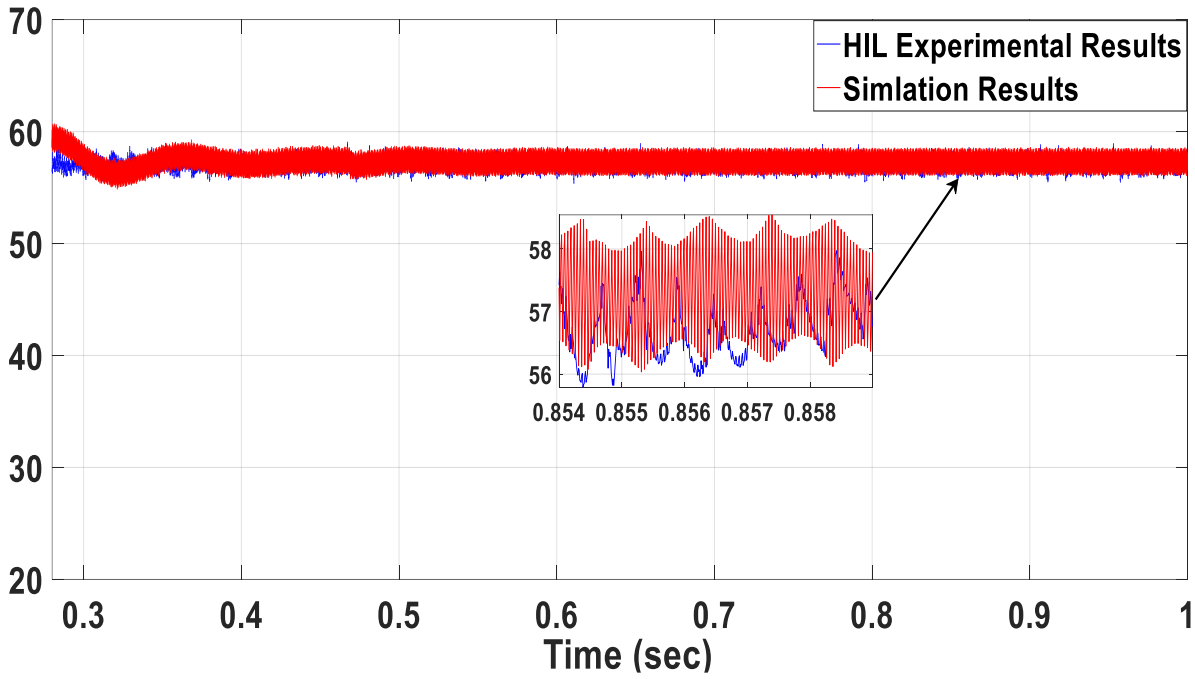

Fig. 4.38. Motor torque in N.m measured from simulation and HIL

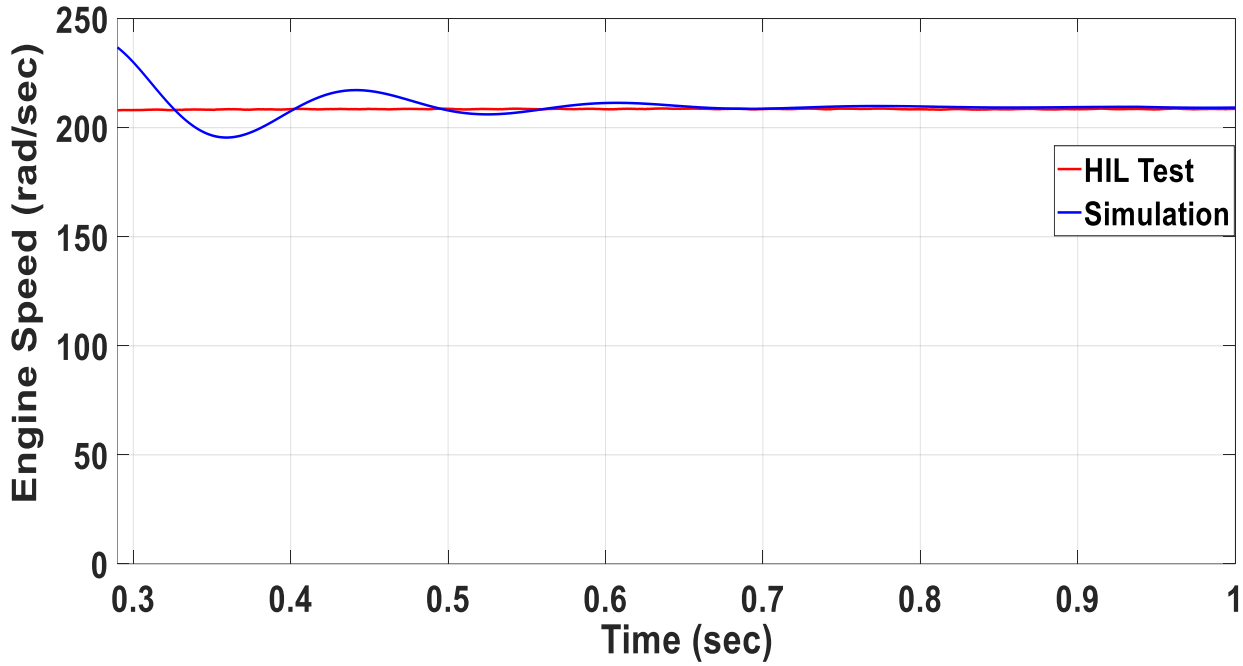

Fig. 4.39. Engine speed in rad/sec measured from simulation and HIL

4.6 Chapter Summary

The transmission efficiency typically varies with the vehicle speed as shown in Table 4-2. This relation is not linear as noticeably shown in the table. However, with inMotive it is noticeably higher than many alternatives in the market as per below.

Table 4-2: Vehicle speed vs. transmission efficiency

Vehicle speed (rpm)	Transmission Efficiency (%)
1000	95.68
1500	96.28
2000	95.98
2500	94.64
3000	93.65
3500	92.63
4000	92.97
4500	91.44
5000	90.46
5500	87.48
6000	81.96

Also, the influences of single-speed transmission and two-speed transmission have been compared. The results have shown that the two-speed transmission gives better performance in both dynamic and economic performance. Therefore, it is clear that the two-speed transmission extends the vehicle's range. Additionally, the two-speed transmission increases the efficiency of the motor by about 2% compared with the single-speed transmission.

After incorporating the two-speed transmission system, the transient technique has been used in vehicle powertrain modeling. The transient model is used to examine the dynamical behavior of the included subsystems, design the controllers of the converters, and improve the accuracy of the results and allow for a detailed dynamic analysis. Also, it has the flexibility to be applied for all

electrified vehicles. The transient model proposed is then used in the hardware-in-loop setup to simulate the vehicle behavior in real-time.

Experimental verification using Hardware in-the-Loop (HIL) new technology on a Typhoon platform has been implemented to testify the accuracy and robustness of the proposed HEV model of a Chevy Volt case study. It is worth mentioning that, the entire control algorithm has been tested in real-time through being downloaded a C-code on the dedicated HIL digital signal processing (DSP) board. Then, the individual performance of each component of the entire system was closely monitored. It can be clearly included from the simulation results and the experimental results introduced in this chapter that both results are in a very close agreement which demonstrates the effectiveness of the proposed model and its mathematical methodology especially that it is based on a real data for a real car commercially used in the market now. The approach adopted in developing this model can be extended to model new transportation systems like Hyperloop. The proposed modeling is generic and can support modeling of all Electrified Vehicles.

Chapter 5. Comparative Studies for HEV/EV System Efficiency Improvement

5.1 Introduction

In this chapter, the usage of wide band gap devices such as Gallium Nitride GaN and Silicon Carbide (SiC) as replacement of the traditional Silicon devices in Electric Vehicles' machine drive in DC/DC converters is being discussed and Nissan Leaf EV is adopted as a case study for this work. Therefore, WBG devices have been integrated within the proposed investigate the Wide their capabilities and examine the system efficiency. To conduct a fair comparison between GaN and SiC using the simulated model, the results have been collected one time using SiC and another time using GaN. The comparison relies mainly on the efficiency and total losses. A proof of concept prototype for a Nissan Leaf DC/DC converter was built in the lab and results were collected. Then, experimental results have been investigated in terms of how close they are to the simulation results.

The second objective of this chapter is to investigate the optimum motor selection for HEV/EV application. Therefore, a detailed comparative study between three types and configurations of induction motor is established. The three configurations are singly fed induction motor (SFIM), the doubly fed induction motor (DFIM), and the cascaded doubly fed induction motor (CDFIM. A detailed finite element analysis has been performed to support the comparison.

5.2 Wide Band Gap Devices in HEV/EV

Through reducing the losses in power and minimizing the weight, we can increase the power density of the DC/DC converter. Many topologies were investigated to improve the power density and efficiency of the boost converter [139]. Minimizing the power losses will result in maximizing

the power transfer and decreasing the sink size. The converter power density can be enhanced via using those low power losses that lessen the switching losses in addition to the conduction losses.

Regarding the technical performance of the vehicle, ripples in current and voltage are related to converter switching frequency. A higher switching frequency results in lower voltage ripples. Meanwhile, lower converter current ripple will reduce the harmonic power loss in the magnetic cores, hence shrinking the heat sink size and lowering its weight. On the other hand, higher switching frequencies will also allow utilizing the pulse current rating of the switch that increases as the pulse width decreases and as the frequency increases. However, operating the DC/DC converter at higher frequency will result in more switching losses. The optimal switching frequency and other converter parameters were the focus of [140]. To gain these technical and economic benefits in terms of power density and smoother current and voltage with lower ripple; the converter switches should operate at higher frequency to attenuate current and voltage ripples while still gaining better power density. The most important aspect to decrease the switching losses for the same frequency or for higher ones is the proper choice for the switch material.

Using wide band gap semiconductors such as GaN and SiC models paves the way for manufactures to design for high frequencies and lower switching losses. Their switching characteristics give the designers the availability to make a trade-off either by using the same switching frequency to enhance the efficiency or minimizing the size, weight and cost of filtering components through increasing the frequency [141]. At 100 kHz, it was found that approximately efficiency of 99 % can be reached by using Si E-HEMT or GaN for computer power supplies. The key point for obtaining such efficiency is the low On-resistance, low charge and high speed as reported by Fujitsu semiconductors [142]. A one MW motor drive case study for a shipboard in [143] showed that SiC-based inverter can decrease the total loss to 30% and cooling system size

to 15% of the Si-based design. Analysts believe that WBG devices will replace the silicon especially in the 600-700 V range in the upcoming years [144]. As many papers in the literature go through the high voltage WBG transistors performance, this paper presents the usage of GaN E-HEMT cascode and SiC trench MOSFET for the high power high voltage application of DC/DC converter for EV motor drive.

5.3 Performance Comparison

To investigate the performance of the wide band gap devices, SiC has been tested at 400 kHz and GaN at 50 kHz whilst the pure Si is evaluated at 50 kHz. The simulation results are obtained at the room temperature 25 ºC. As shown in Fig. 5.1, the losses dissipated in the GaN-HEMT cascode is measured to be 183 W which is apparently less than the pure Si-MOSFET that is considered to have a total losses of 1080 W at the same switching frequency. This case will remain the same for all the switching frequencies starting from 50 kHz up to 400 kHz. The more the switching frequency increases, smaller size and higher power density can be attained.

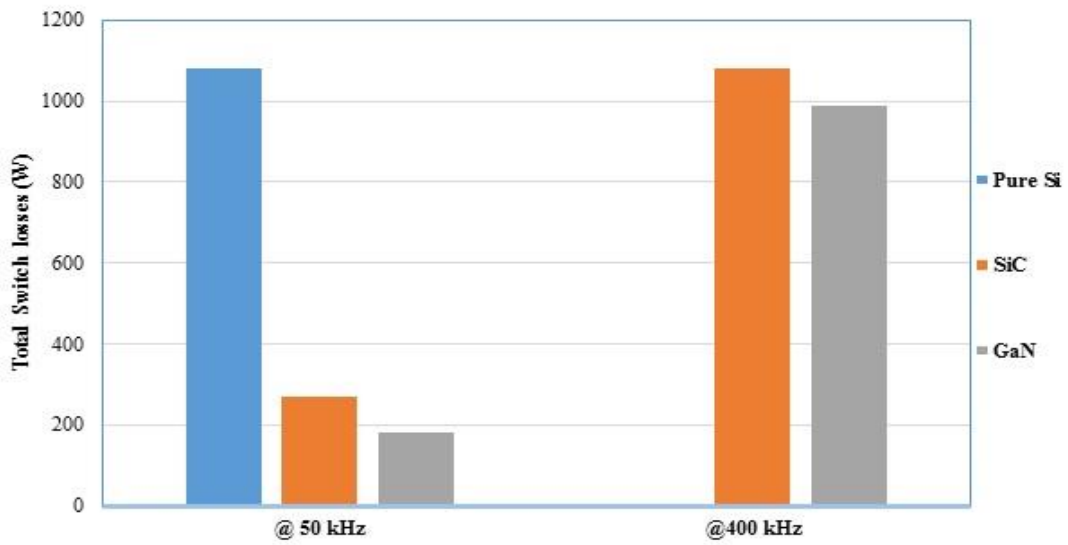

Fig. 5.1. Power losses in watts for the switch

The same conclusion is observed in case of SiC. It can be deduced that for the same range of frequencies starting from 50 kHz to 400 kHz, the switching losses inside SiC is less than the one inside pure Si. However, in terms of comparing SiC to GaN, it can be demonstrated that GaN-HEMT cascode is efficient as at 50 kHz, the losses in GaN is 270 W at 50 kHz and in SiC is 1080 W at 400 kHz which accordingly resulted in 0.457% and 0.675% as load power loss respectively.

Another comparison has been conducted at 400 kHz to show the contribution of switching and conduction loses in the total losses of the GaN-HEMT cascode switch and SiC switch as shown in Fig. 5.2. It is apparent that the GaN conduction losses is less than SiC Trench MOSFET. However, at low frequencies, this difference increases drastically as the switching losses will be much less.

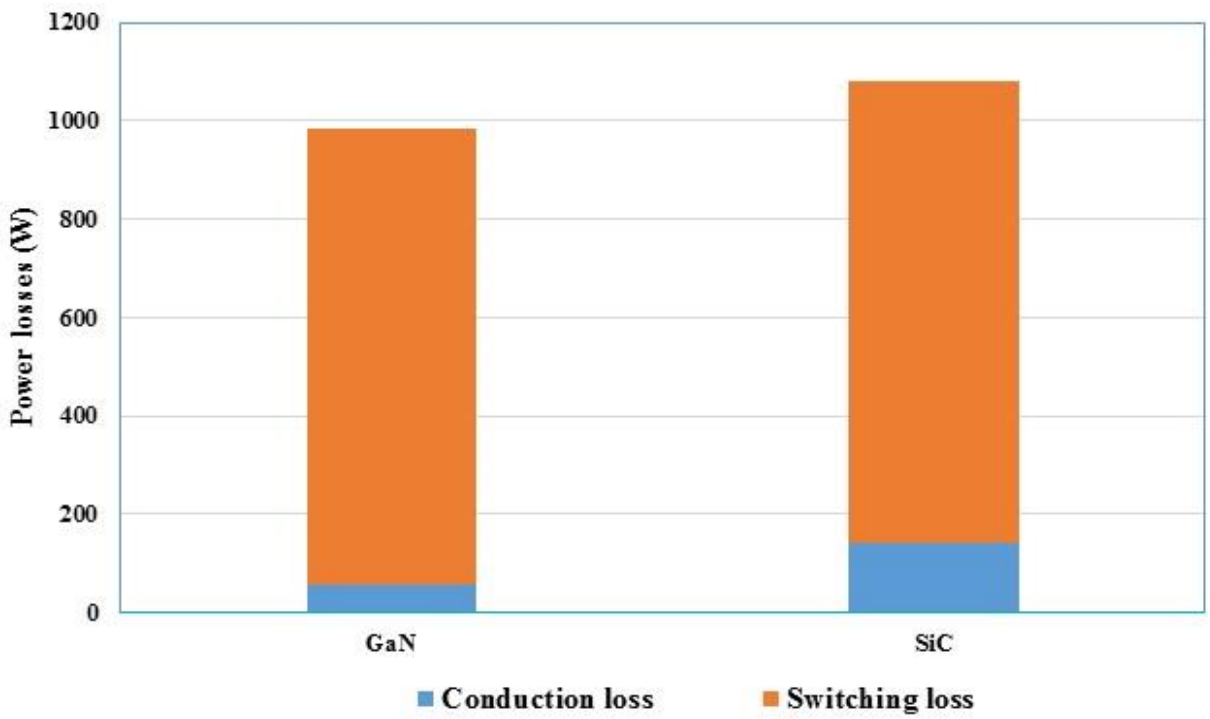

Fig. 5.2. Switch losses of in watts at 400 kHz

5.3.1 Efficiency and Size Reduction Evaluation

This section highlights and summarizes the results obtained from making a comparison between Pure Si, SiC ACCUFET, and GaN Cascode MOSFETS according to the junction temperature and switching frequency possible combination options. As illustrated in Fig. 5.3, all of the efficiencies of all NLEV cases studied.

Table 5-1: NLEV powertrain's DC/DC converter efficiencies for 50 kHz

Temp	Pure Si MOSFET	SiC ACCUFET	GaN Cascode
25 ºC	98.96	98.99	99.65
150 ºC	98.8	98.91	99.52

Table 5-2: Comparison of efficiencies of NLEV's DC/DC converter incorporated with different semiconductors at different frequencies

Temp	Pure Si MOSFET	SiC ACCUFET	GaN Cascode
25 ºC	98.96	98.3	99.06
150 ºC	98.8	98.16	98.92

Table 5-3: NLEV powertrain's DC/DC converter efficiencies at 25 ºC

Switching frequency	Pure Si MOSFET	SiC ACCUFET	GaN Cascode
50 kHz	98.96	98.99	99.65
maximum	98.96	98.3	99.06

Table 5-4: NLEV powertrain's DC/DC converter efficiencies at 150 ºC

Switching frequency	Pure Si MOSFET	SiC ACCUFET	GaN Cascode
50 kHz	98.8	98.91	99.52
maximum	98.8	98.16	98.92

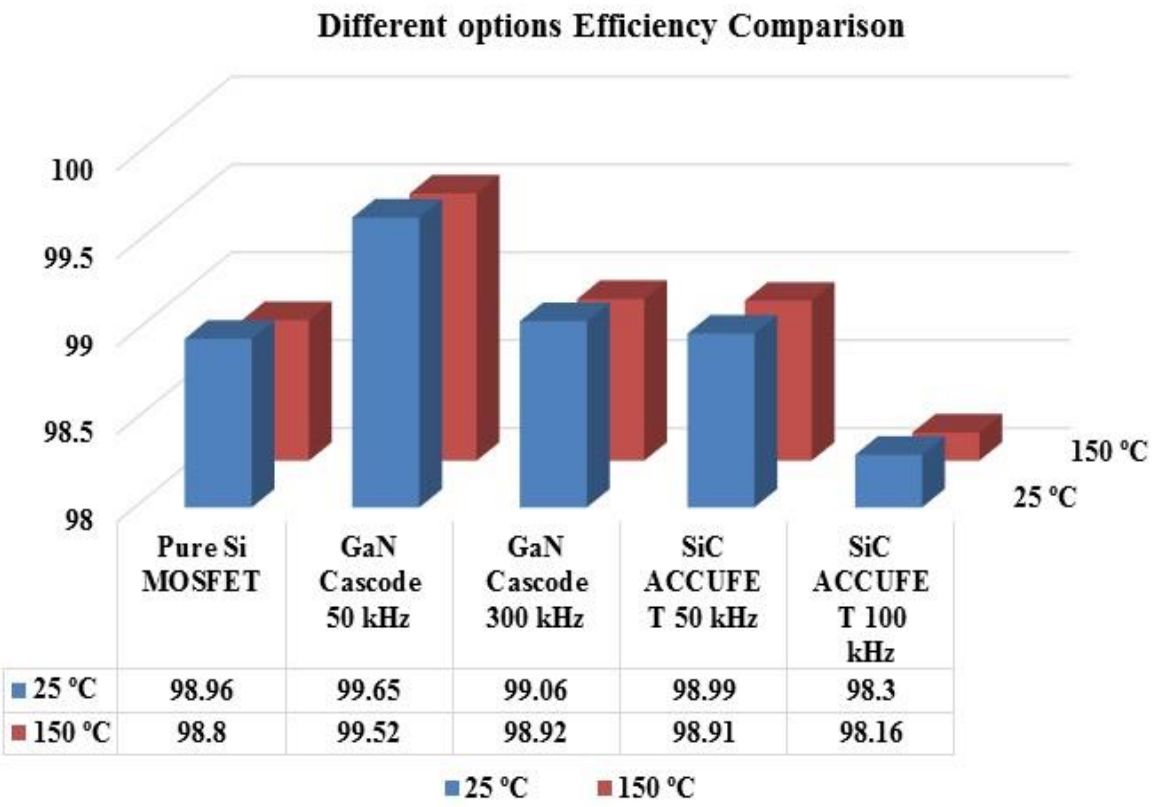

Fig. 5.3. Efficiencies for various devices

All the enhancements observed in using SiC and GaN in replacement of pure Si MOSFET are highlighted and tabulated in Table 5-1 and Table 5-2. In this study, Si MOSFET are used as a benchmark for our study. Also, variations in conversion efficiency for SiC with respect to GaN are demonstrated in Table 5-5, Table 5-6 and Table 5-7.

Table 5-5: Difference in efficiencies at 25 ºC and 150 ºC

Temp.	SiC ACCUFET	GaN Cascode
25 ºC	0.03	0.69
150 ºC	0.11	0.72

Table 5-6: Difference in efficiencies from pure Si MOSFET at different frequencies

Temp.	SiC ACCUFET	GaN-HEMT Cascode
25 ºC	- 0.34	0.14
150 ºC	- 0.64	0.12

Table 5-7: Reduction in SiC efficiency from GaN

Switching frequency	25 ºC	150 ºC
50 kHz	-0.66	-0.61
Maximum	-0.76	-0.76

It can be concluded from the previous results that introduction of GaN and SiC as wide band gap devices allows for more flexibility in operating at high frequencies while not compromising on the converter efficiency in a good power range. Therefore, the converter efficiency incorporated with those new semiconductors can be of less size, weight and cost of passive components.

The fact that these semiconductors can reduce power losses contribute to reduction in the size of an automotive cooling system by 60% or even eliminate the secondary liquid cooling system.

5.3.2 Simulation Results

As shown in Fig. 5.4, all of the three switches have almost the same average value of the supply (battery) of approximately 129.3 A. The filter is designed at 50 kHz and the ripples vary inversely to the frequency and it is recorded that the ripple in current is 0.01 A (0.008%) while 0.07 A (0.05%).

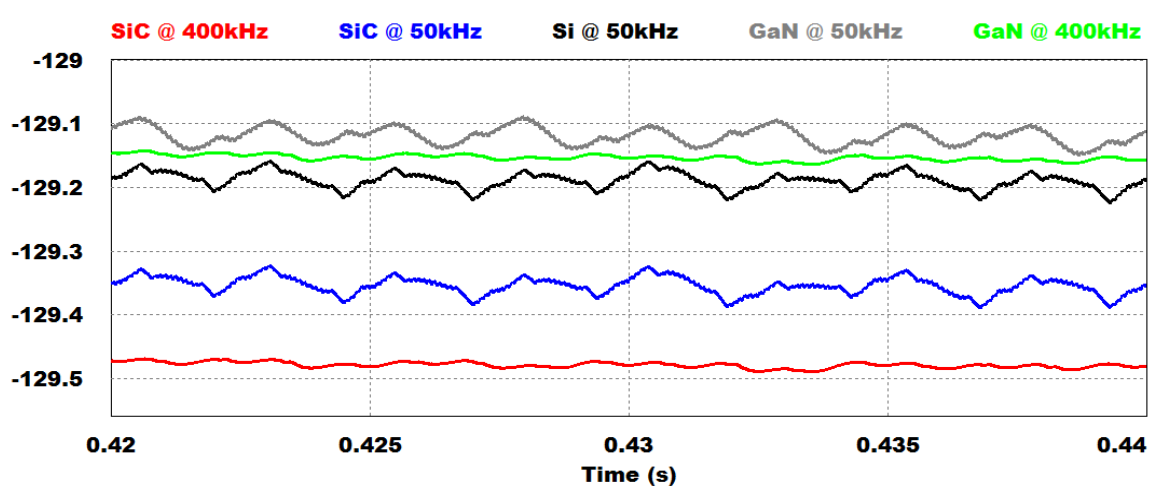

Fig. 5.4. Waveform of battery current (A)

Fig. 5.5 shows the DC bus voltage waveform slight frequency change irrespective of the switch type. The voltage ripples at 400 kHz is 2.4 V which is 4.8% whilst it is 3 V or 6% at 50 kHz. Regarding speed variation, it has been observed that operating SiC at high frequency resulted in a slightly higher of 1.5 rpm as shown in Fig. 5.6. Also, it demonstrates a higher speed for GaN at any frequency. The torque shape of the EV is almost the same as can be shown from Fig. 5.7 with a small time shift for the three switch types. This means that the control units still capable of achieving the constant load torque with increased frequencies for any switch type.

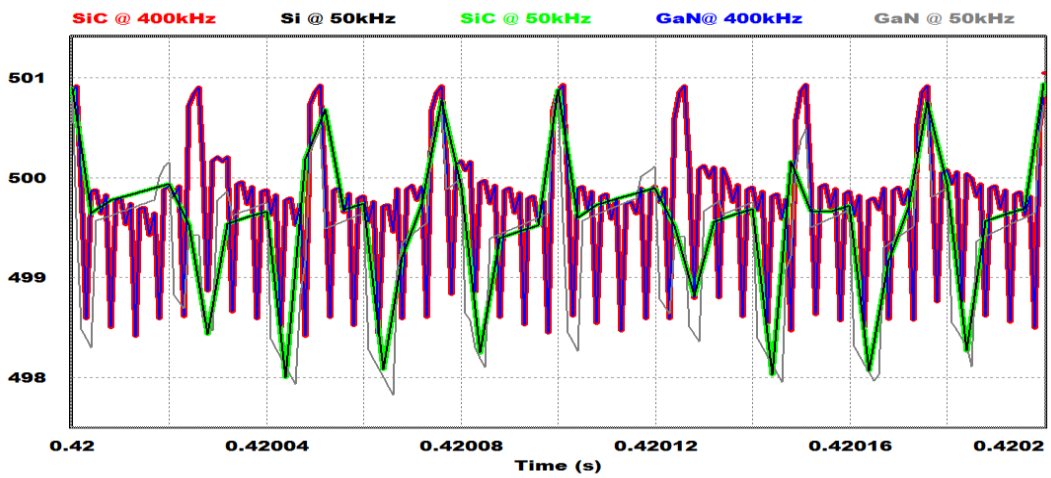

Fig. 5.5. Waveform of the DC bus voltage (V)

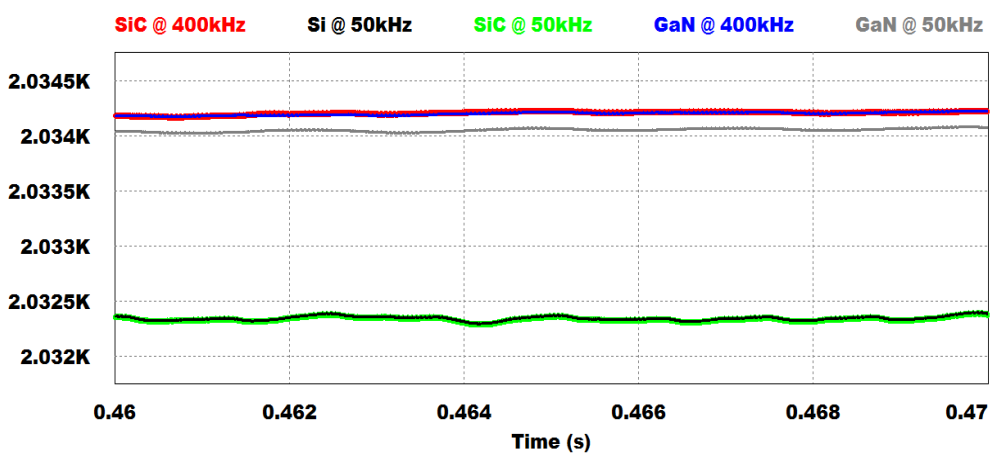

Fig. 5.6. Speed of the vehicle in rpm

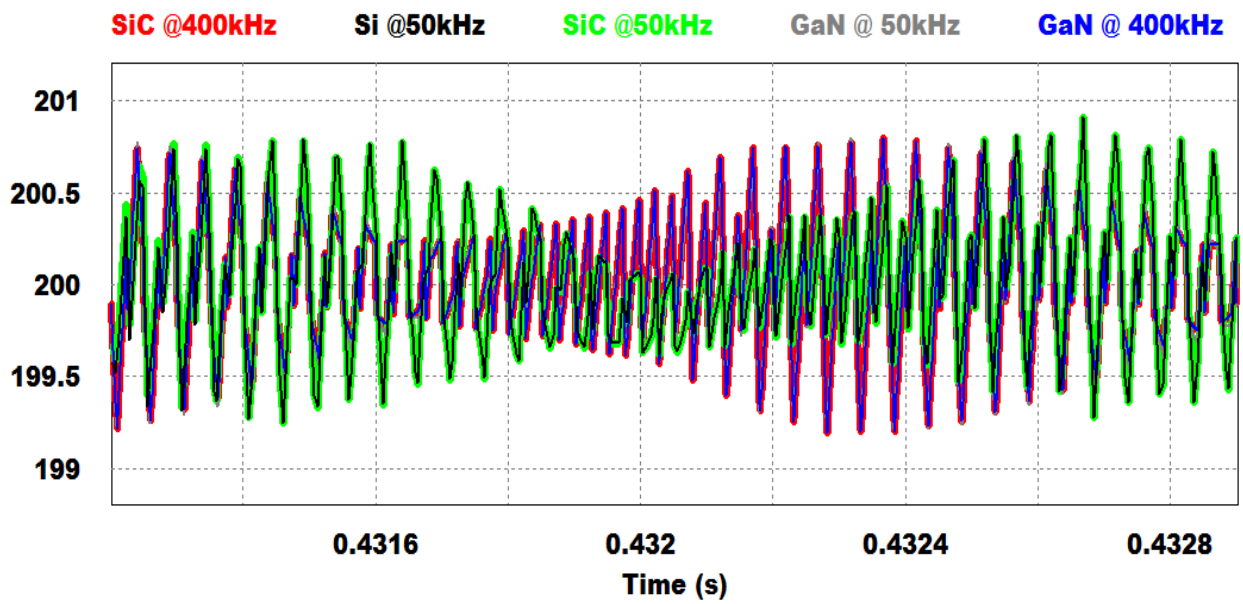

Fig. 5.7. Torque of the vehicle in newton meter

5.3.3 Regenerative Braking to 1% of Regular Speed

From the drive cycle test, it can be demonstrated that the regeneration stage within 0.1 sec followed the starting of braking command at 0.5 sec then ends within 0.7 sec with respect to the starting of the drive cycle. This delay allows for the regenerative power to reach the threshold of regeneration control. Table 5-8 summarizes the average power regenerated back to the battery over the regeneration time period at 25 ºC for the suggested maximum frequencies in kW and percentage of motoring input power. The GaN-HEMT cascode option recovered more power back into the battery, then the pure Si MOSFET, and finally the SiC ACCUFET with the same order of efficiency seen in Table 5-8.

Table 5-8: 25 ºC average regenerated power

GaN-HEMT Cascode (f=300 kHz)	7.88 kW	45.03 %
SiC ACCUFET (f=100 kHz)	6.9 kW	39.43 %
Pure Si MOSFET (f=50 kHz)	7.1 kW	40.57 %

5.3.4 Components Size Reduction

The heat sink size and the filtering components size have been investigated and the results are summarized in Table 5-9. Using SiC-ACCUFET at 100 kHz, it was found that the heat sink size is reduced by 36.6 % and a 50 % reduction in the filtering components size is achieved. However, using SiC-ACCUFET at 50 kHz will result in a 54.5 % reduction in the heat sink size.

Table 5-9: Percentage of the reduction in the heat sink and filtering components size

	ACCUFET- SiC (f=100 kHz)	ACCUFET- SiC (f=50 kHz)	Hybrid module (f=50 kHz)
Heat sink size reduction (%)	36.6	54.5	--
Filtering components size reduction (%)	50	--	--

5.3.5 Experimental Results

The experimental setup for the DC/DC converter is shown in Fig. 5.8 and Fig. 5.9. Also, Fig. 5.10 shows the overall powertrain test bench. As shown in Fig. 5.10 and Fig. 5.11, the test bench consists of a PM motor, high power rectifier, DC/DC converter and an inverter. Tests were carried out to verify the superiority of the GaN-HEMT cascode and SiC ACCUFET respectively in terms of higher efficiency and higher switching frequency. According to the descaled lab-tested system, the GaN switch can achieve a stable efficiency around 98.7% at 100 kHz switching frequency. SiC ACCUFET can record the same efficiency while switched only at 40 kHz. This GaN record efficiency is stable with different switch loading percentages. These findings, listed in Table 5-10, are in consistence with the simulation results. Also, Fig. 5.12 shows the inverter circuit waveforms which reveal that ZVS occurs in both turn-on and turn-off instants, which reduces the total power losses by eliminating the switching losses of the inverter switches. Moreover, ripple reduction in voltage/current waves is achieved with using DV/DT filters, DTC methodology, and inverter motor control loop.

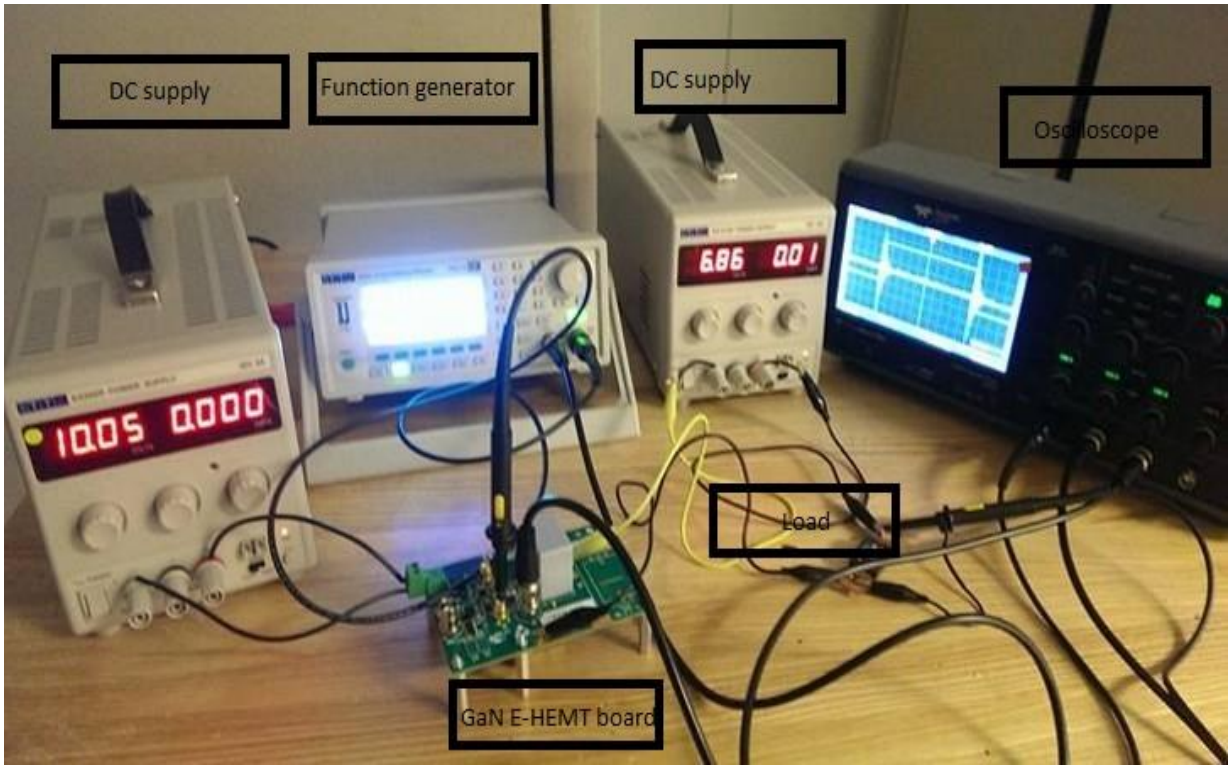

Fig. 5.8. GaN E-HEMT test bench board

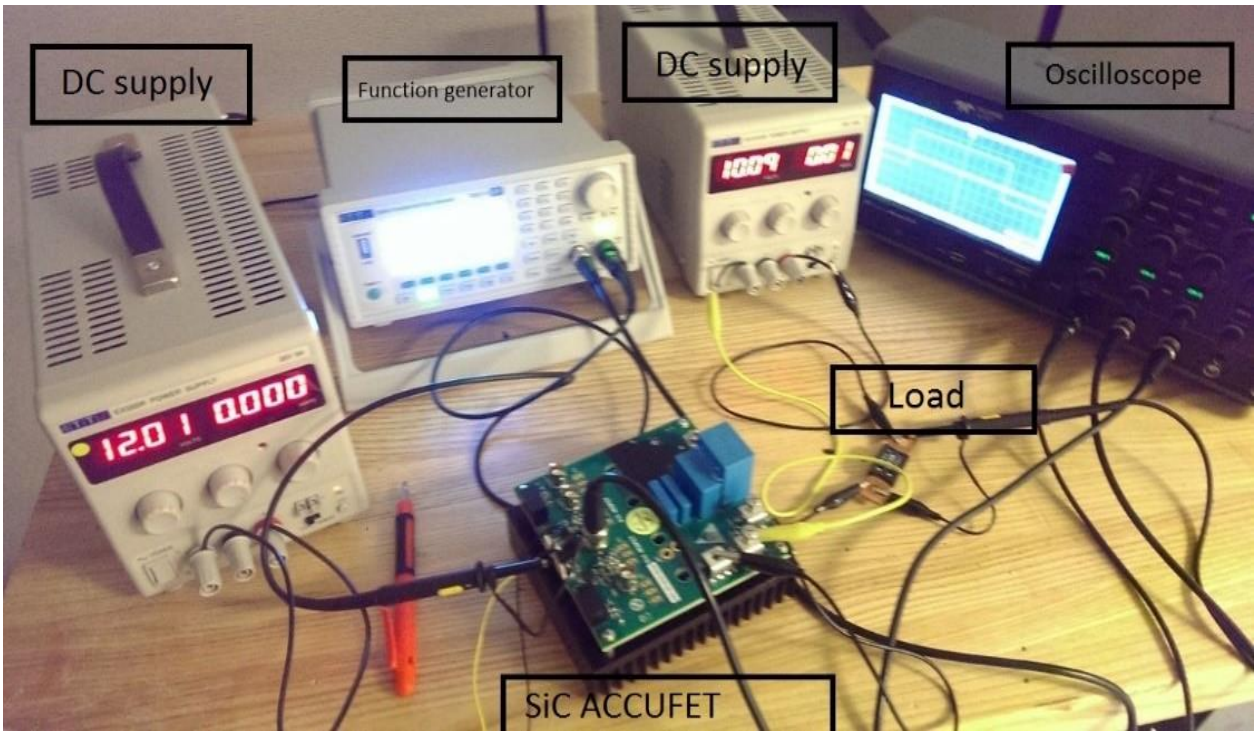

Fig. 5.9. SiC ACCUFET test bench board

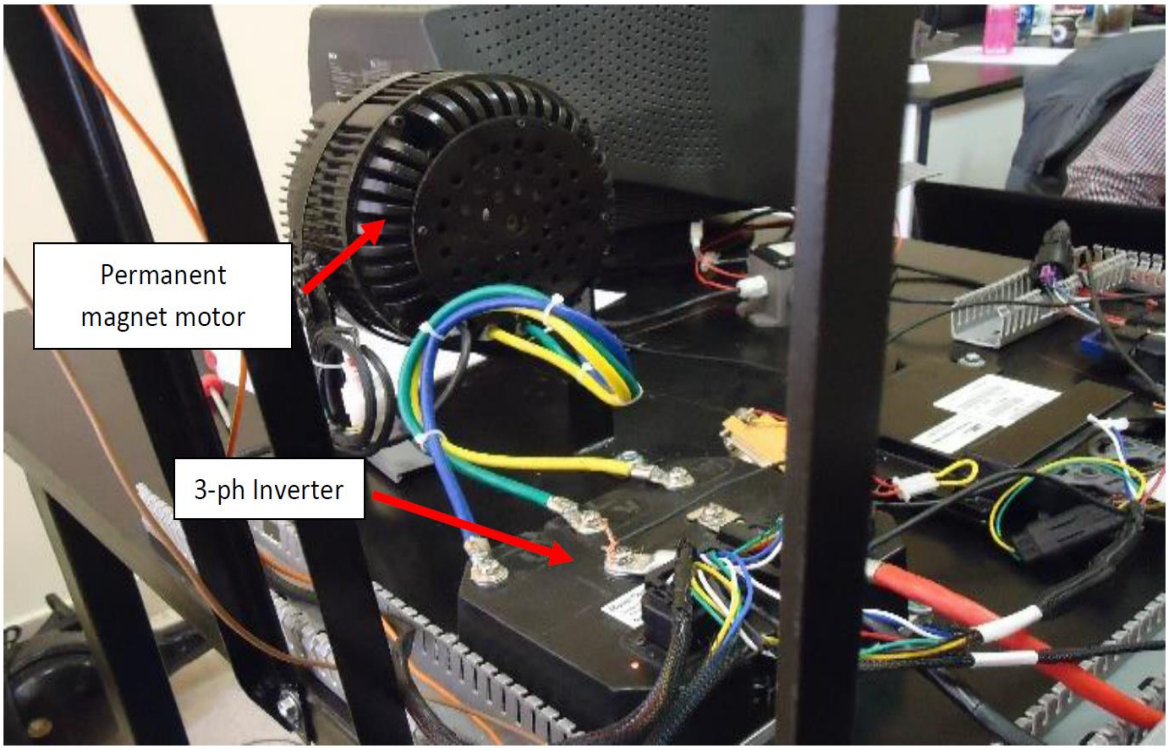

Fig. 5.10. PMSM of the test bench

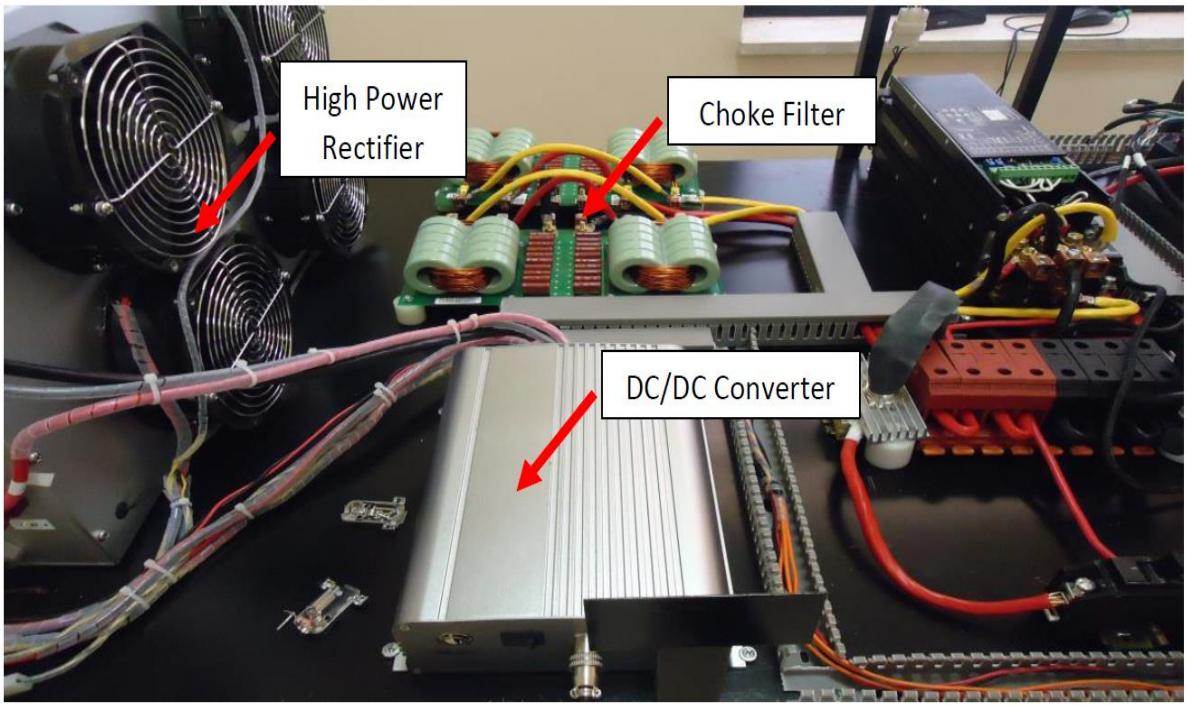

Fig. 5.11. Powertrain test bench components (High-power rectifier, DC/DC converter)

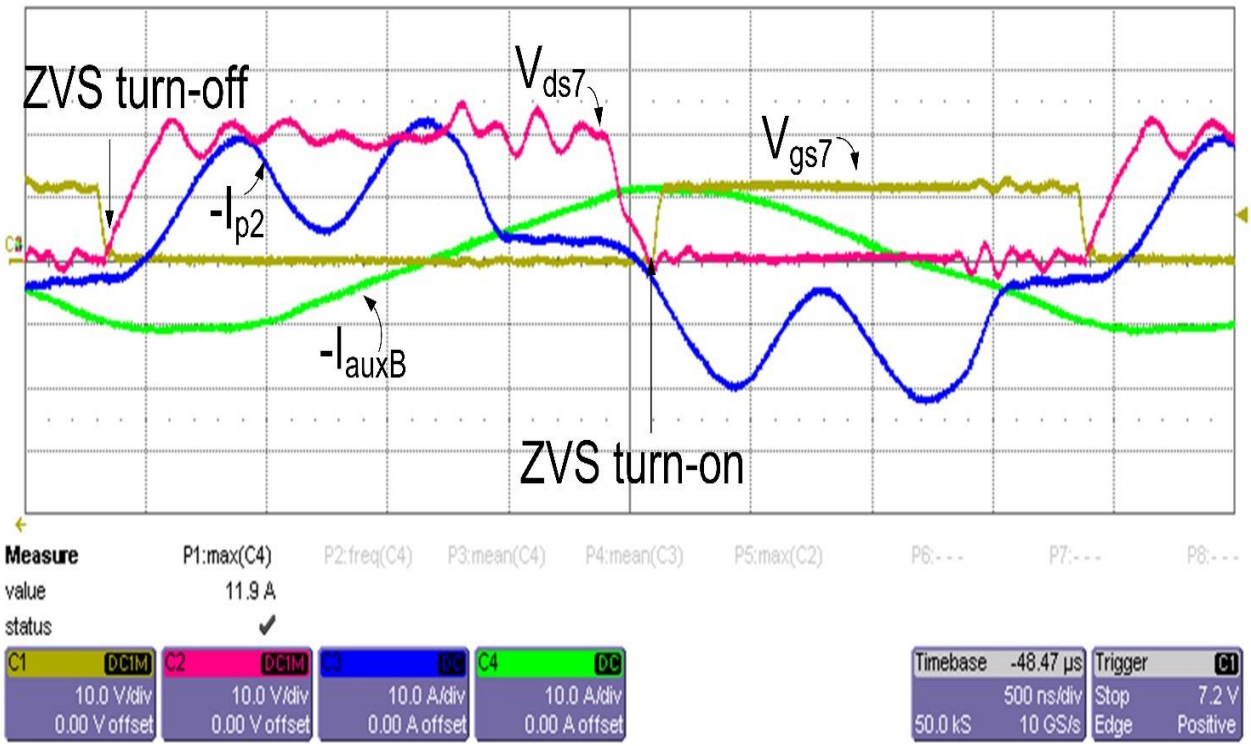

Fig. 5.12. Turn-on and turn-off instants of zero voltage switching

Table 5-10: Experimental Efficiencies of the Wide-Band Gap

	GaN	SiC
f (kHz)	100	40
Efficiency (%)	98.9	98.9

5.4 Motor Selection

In this section, a detailed comparative study between singly fed induction motor (SFIM), doubly fed induction motor (DFIM), and cascaded doubly fed induction motor (CDFIM) drive systems in EV/HEV applications is presented. The power of the three motors as well as the equivalent inverter size are the same for a given speed and equal power storage capacity. The three motors are assumed to have the same HP rating despite having different parameters such as their inductances and resistances. The design of each motor has been validated through a detailed finite element analysis (FEA) which takes into account the various variables of the motors. The SFIM

and the DFIM are designed and a finite element analysis (FEA) is being applied in details using Ansoft Maxwell 2D. The FEA simulation, which is accepted industrial-wise, is applied. Finally, the inverter sizing and cost is investigated in detail.

5.4.1 Finite Element Analysis

To perform a fair comparison between the induction motor topologies, a detailed finite element analysis (FEA) using Ansoft Maxwell. The cross-sectional areas of the SFIM and the DFIM is depicted in Fig. 5.13 and Fig. 5.14. The SFIM is set to be the baseline of this study. Therefore, we are comparing the performance of the DFIM and CDFIM with respect to the SFIM. The DFIM is assumed to work as a synchronous motor above synchronous speed (super-synchronous mode of operation). Thus, the losses are higher in this case in the SFIM compared to the DFIM. The FEA is implemented at no load based on the SFIM and the DFIM and the results obtained show the difference in operation between the two machines. Fig. 5.15 and Fig. 5.16 show the flux density distribution of the SFIM and DFIM respectively. It can be seen that the maximum magnetic flux density of the SFIM ranges from 1.12 T to 2.00 T in the stator teeth and from 1.28 T to 1.6 T in the rotor yoke. We can also see some higher saturation iron spots at the edges and in the iron bridge. For the DFIM, in the stator teeth, the magnetic flux density is in the range from 1.02 to 1.403 T. It is clear that the flux distribution decreases in the case of DFIM and this id due to the power division between the rotor and the stator in this case which in turn means lower temperature distribution in DFIM.

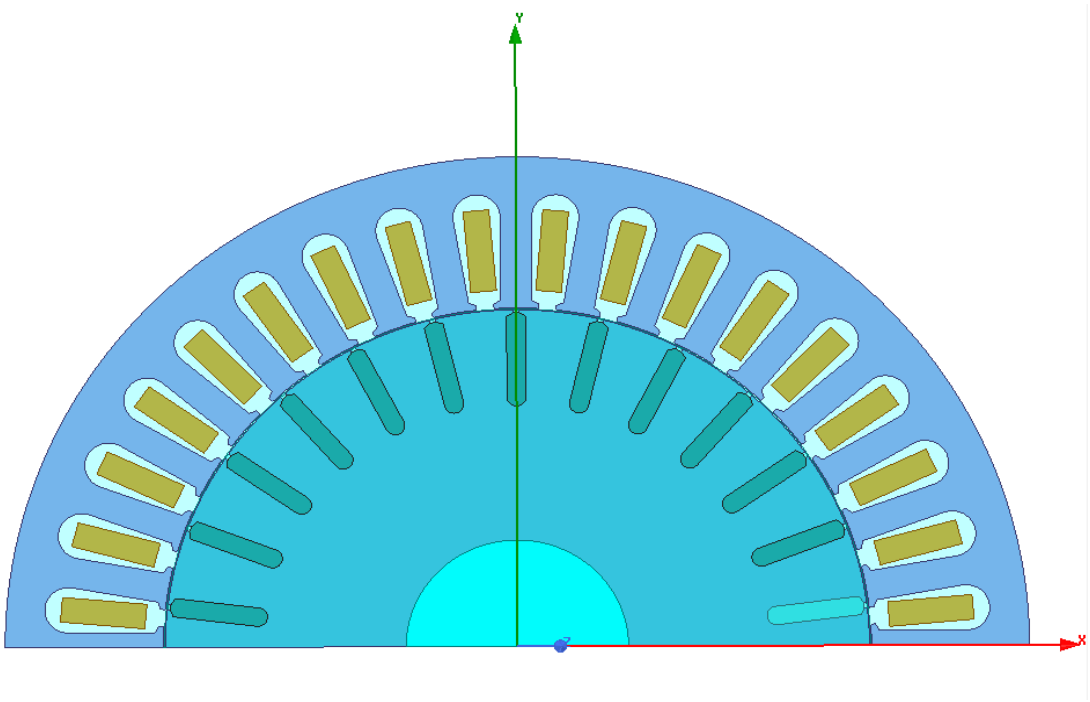

Fig. 5.13.SFIM cross section

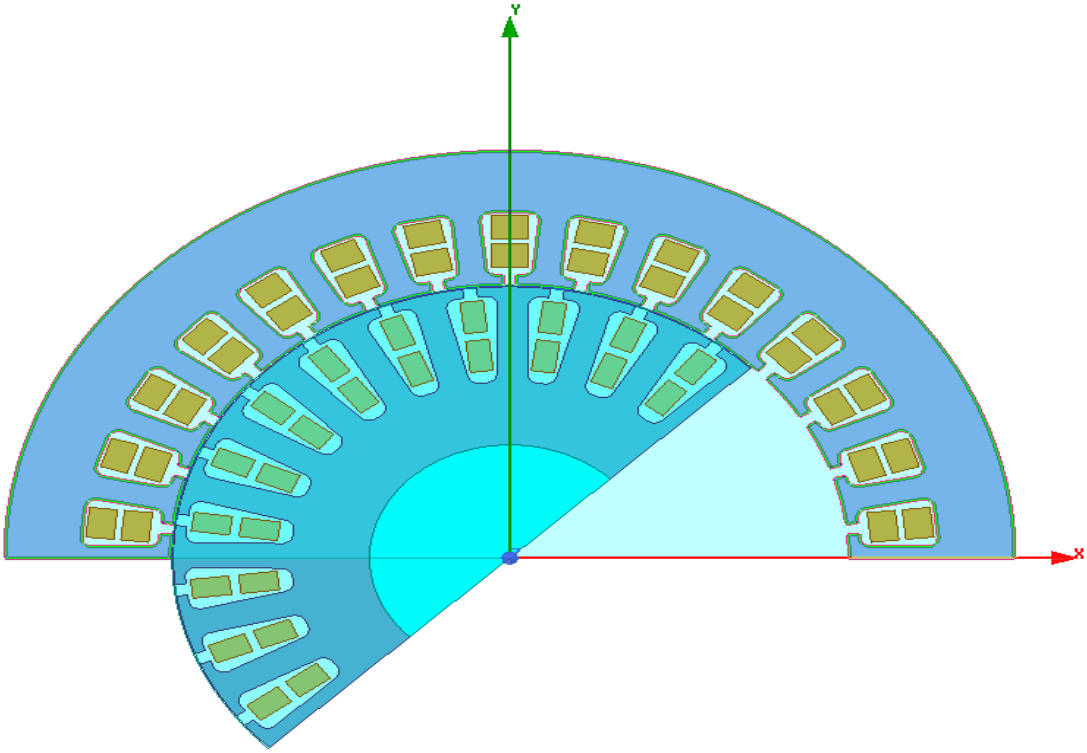

Fig. 5.14. DFIM cross section

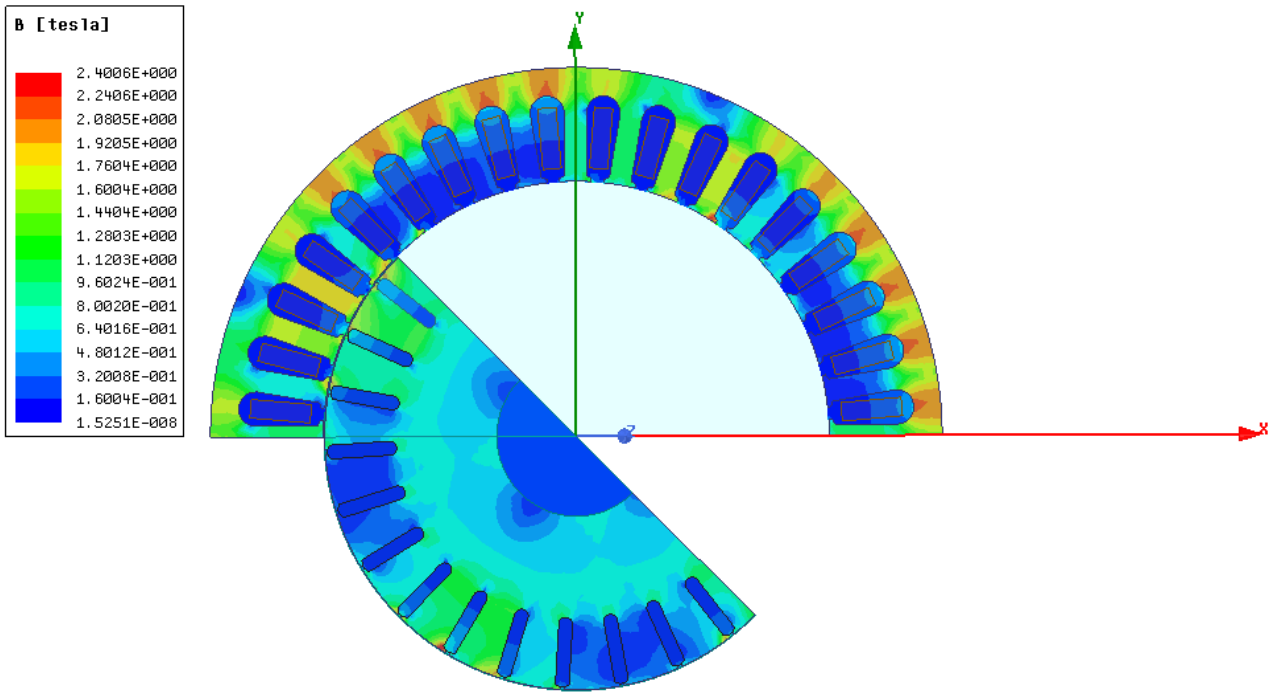

Fig. 5.15. No-load magnetic flux density of SFIM @1475 rpm

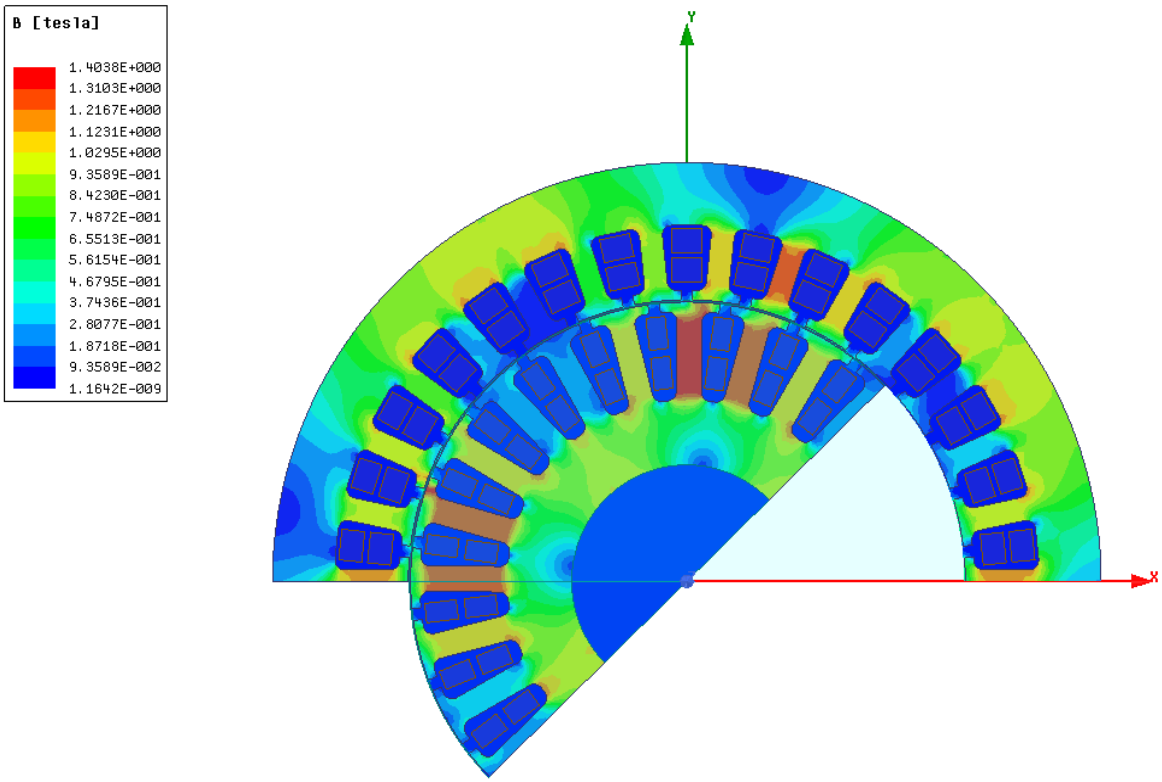

Fig. 5.16. No-load magnetic flux density of DFIM

The no-load flux intensity has been calculated for the two motors and, as can be seen in Fig. 5.17 and Fig. 5.18, the flux intensity H (A/m) is higher in SFIM than DFIM and this is due to the current density in the stator yoke for the two machines. Fig. 5.19 and Fig. 5.20 depict the Ohmic losses occurred in both the SFIM and the DFIM and it can be deduced that the Ohmic losses in the IM are higher than DFIM as well.

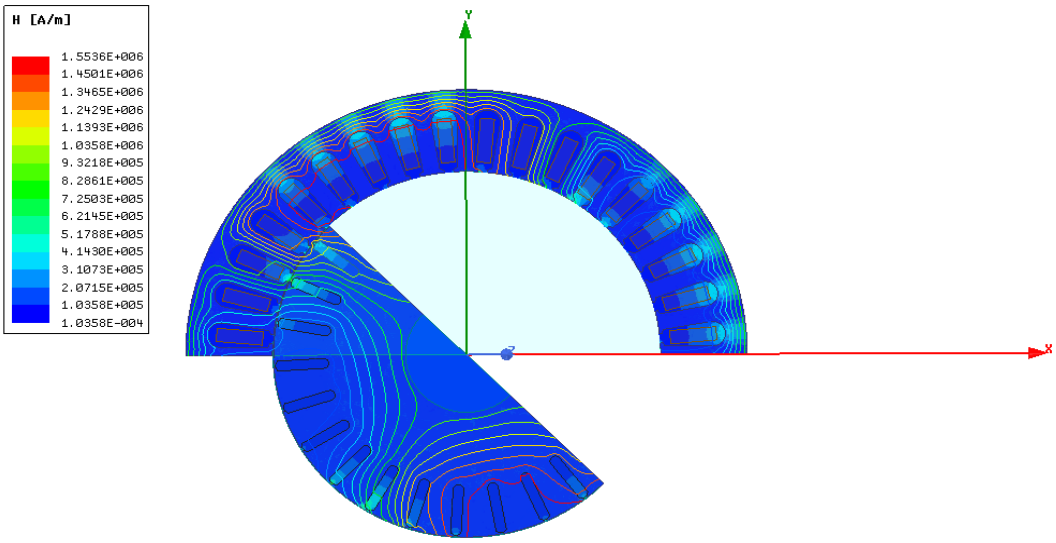

Fig. 5.17. No-load flux intensity of SFIM

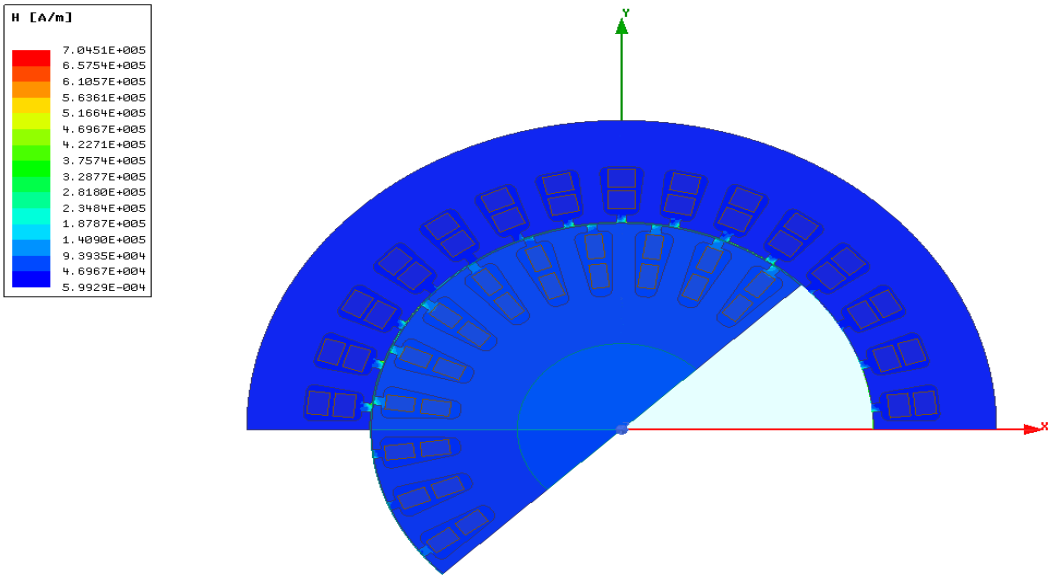

Fig. 5.18. No-load flux intensity of DFIM

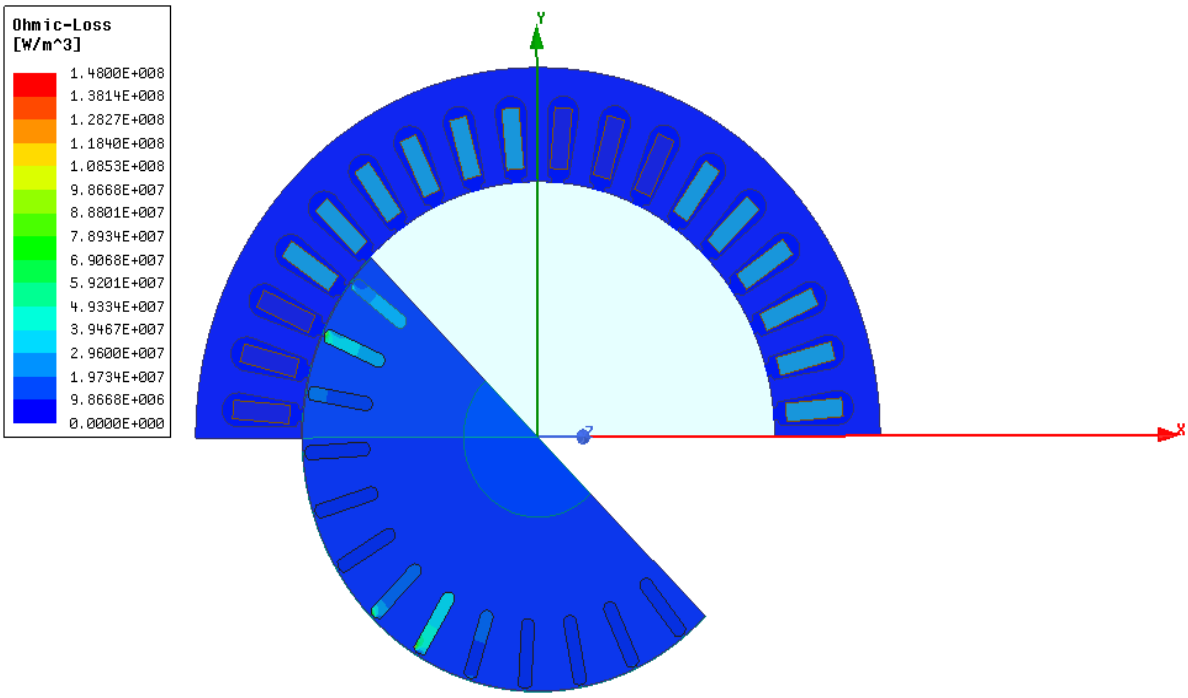

Fig. 5.19. Ohmic losses of SFIM

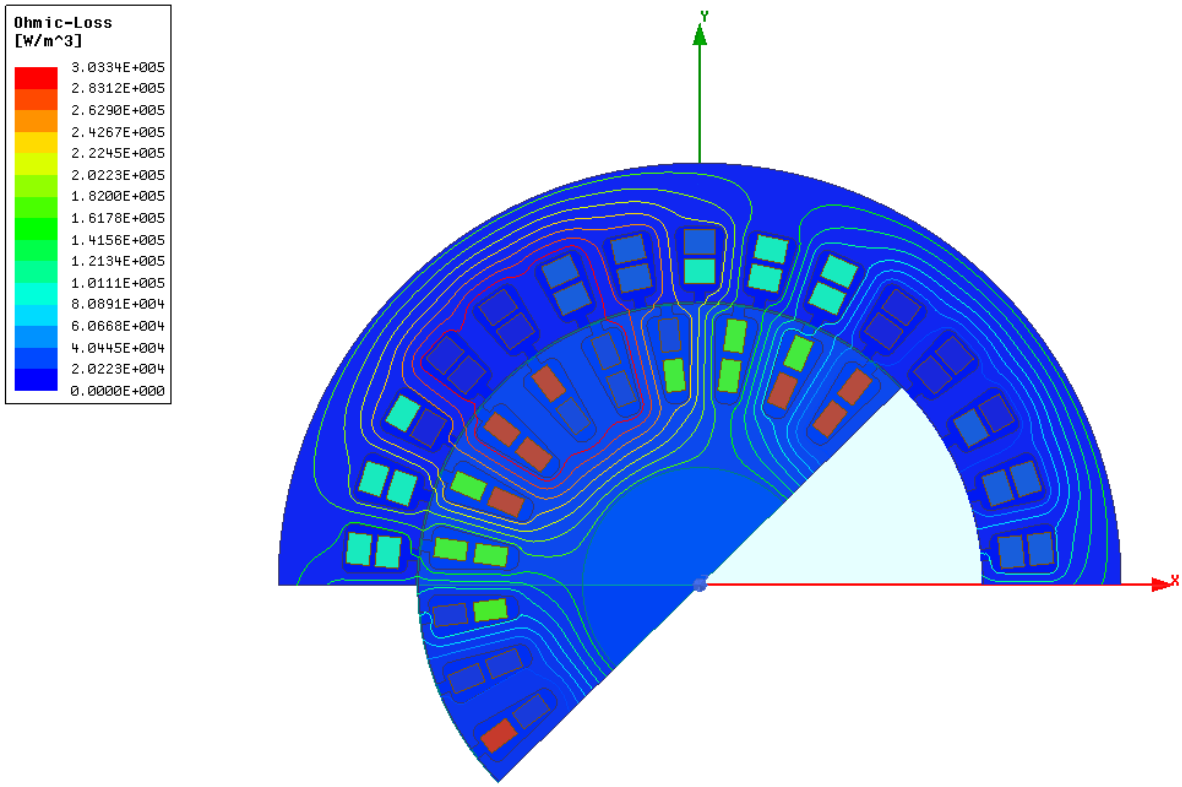

Fig. 5.20. Ohmic losses of DFIM

Fig. 5.21 and Fig. 5.22 show the 3-phase stator currents of the SFIM and the DFIM respectively. It is clear that the currents are oscillating at the beginning then settled to pure sinusoidal waveforms; a typical transient/steady state behavior for a stable system. Fig. 5.23 shows the 3-phase currents in the CDFIM.

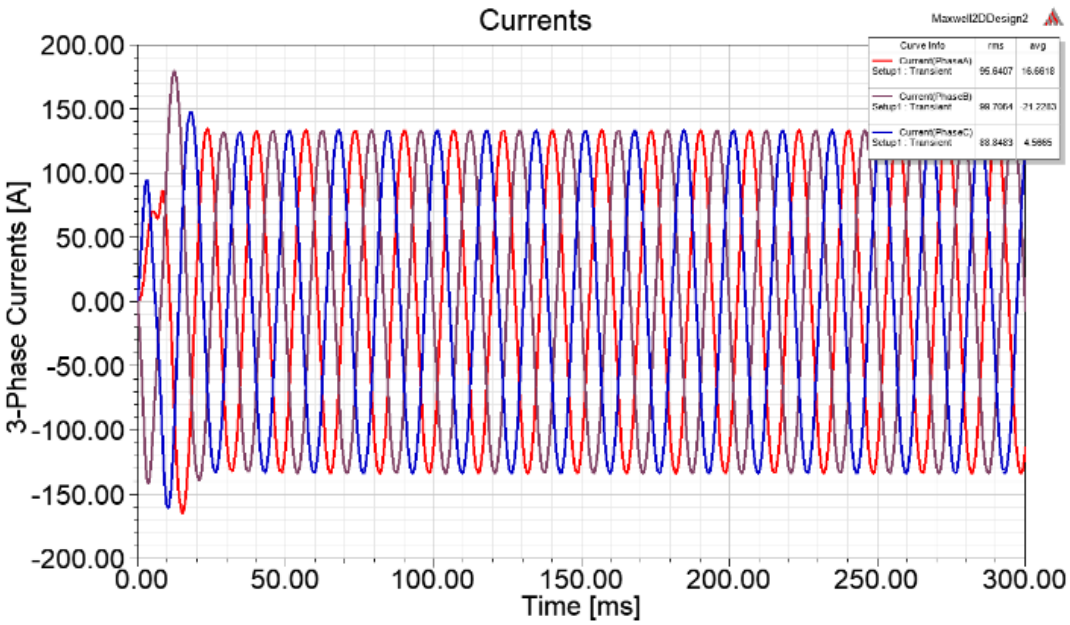

Fig. 5.21. 3-Phase currents in SFIM

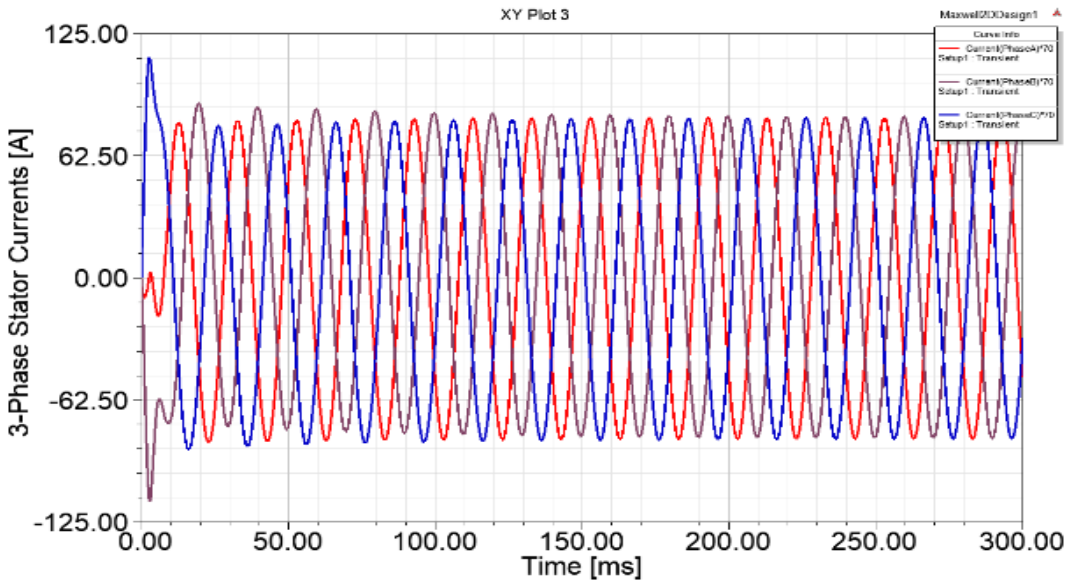

Fig. 5.22. 3-Phase currents in DFIM

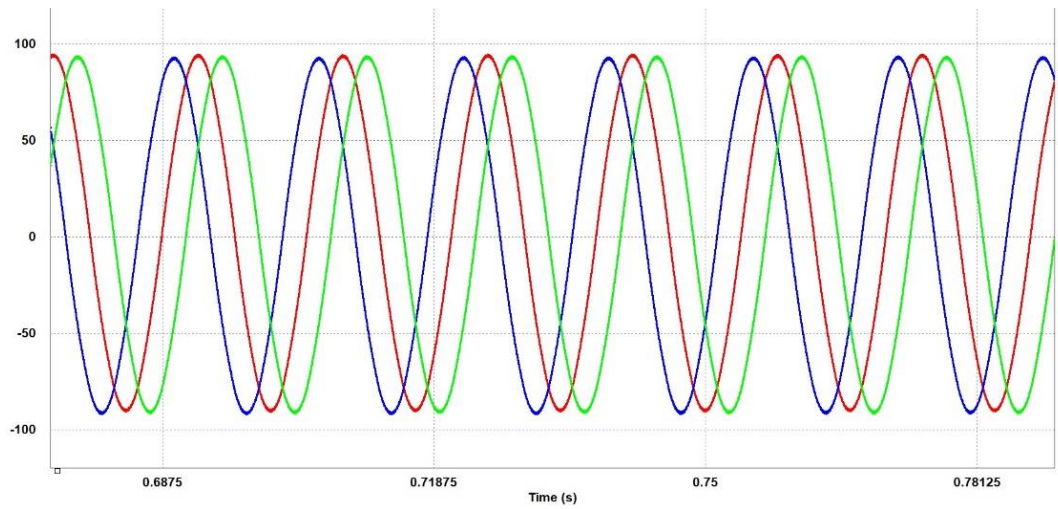

Fig. 5.23. 3-Phase currents of the CDFIM

Fig. 5.24 shows the torque speed capability of the singly fed induction motor. We always prefer to work in the stable zone of operation for which the slip does not exceed 0.2.

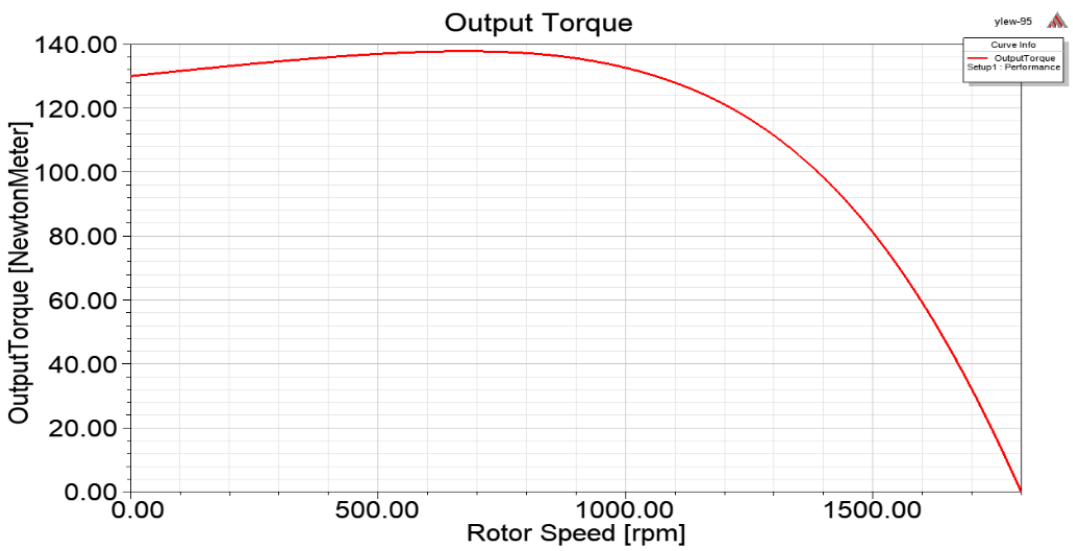

Fig. 5.24. Torque speed capability of SFIM

For an electric motor, the torque capability is always controlled by the supplied current while the speed its torque capability is generally constrained by the available supply voltage. As can be seen in Fig. 5.25 and Fig. 5.26 , the torque capability of the DFIM and the SFIM are almost the same. However, the speed range of the DFIM is double the value of the SFIM. In general, the

DFIM acts as SFIM in the sub-synchronous mode of operation for which the rotor generates power back to the supply voltage. However, if the rotor is being fed by the supply so the speed will be almost doubled.

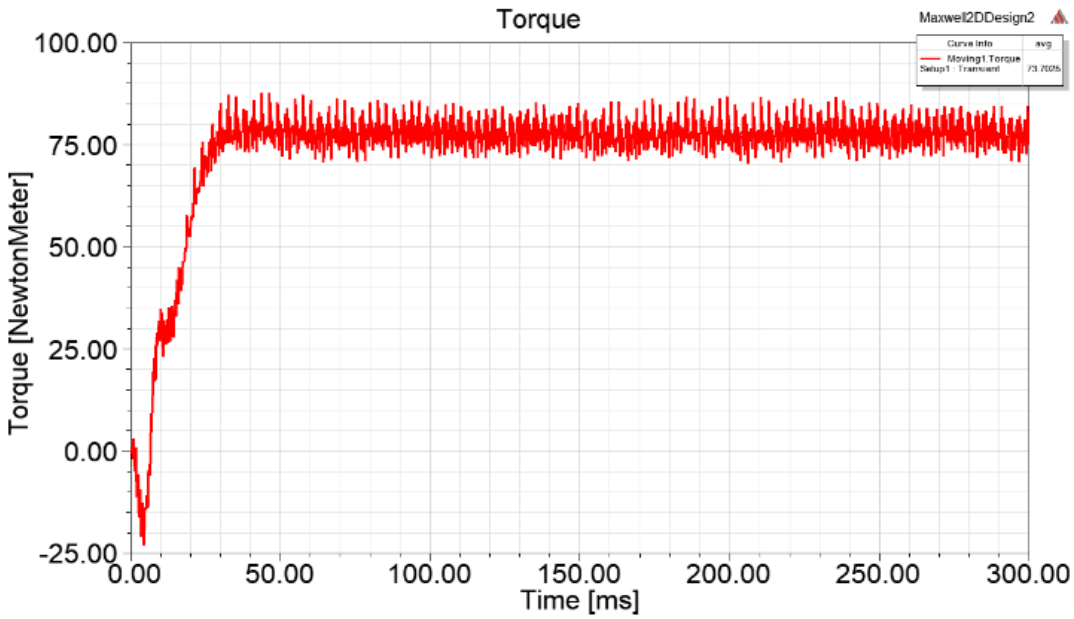

Fig. 5.25. Torque in SFIM

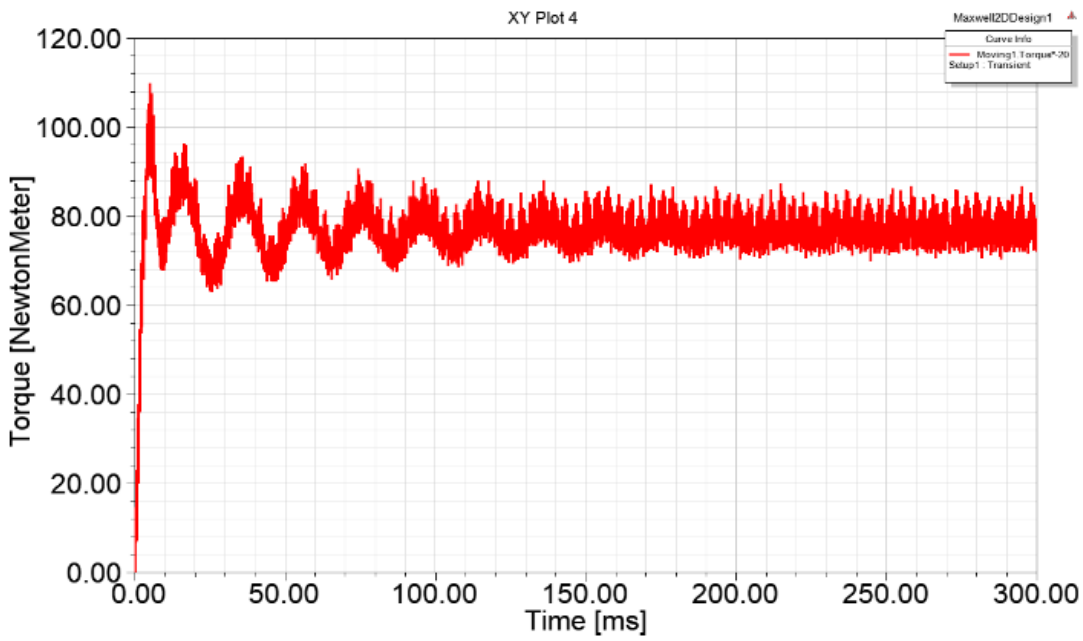

Fig. 5.26. DFIM torque production

5.4.2 Discussion

Aforementioned discussion dealt with each factor that affects the machine design, power converter(s) design, control, performance and cost individually. The results are summarized and tabulated in Table 5-11. Nonetheless, in order to provide a better insight of the advantages and disadvantages combined for the configurations under investigation. A planar figure of merits is used to better demonstrate the most important factors that affect the overall performance of each configuration. These factors are: 1) Magnetic flux density; 2) Machine Ohmic losses; 3) Motor size; 4) Torque Speed Characteristics; 5) Inverter size; 6) Inviter cost; and finally 7) Inverter efficiency. Each factor has been scaled to three levels low, moderate and high. The higher the area covered by interacting with the scales in each factor, the better the expected overall performance of the machine configuration, SFIM, DFIM and CDFIM.

Table 5-11: Simulation results comparison of the three motors drive systems

Comparison Item	SFIM	DFIM	CDFIM
Power density	Low	High	High
Torque/Speed Capability	Narrow (Not beyond base speed)	Double the SFIM	1.8 times the SFIM
Weight	Moderate	1.6 times SFIM	2 times the SFIM
Control Complexity	Moderate	Moderate	Complex
Efficiency at 1000 rpm	60.58 %	78.4 %	80.2%
DC bus voltage	480V	480V	400V

Fig. 5.27 shows the results for singly fed induction machine which is closed to the performance of the doubly fed induction machine shown in Fig. 5.28. while the SFIM has a lower efficiency and lower torque speed characteristics., its machine and inverter size and cost a significantly better.

Also, its magnetic flux density is higher. However, in DFIM, the torque speed characteristics. of the motor and its inverter efficiency are much higher.

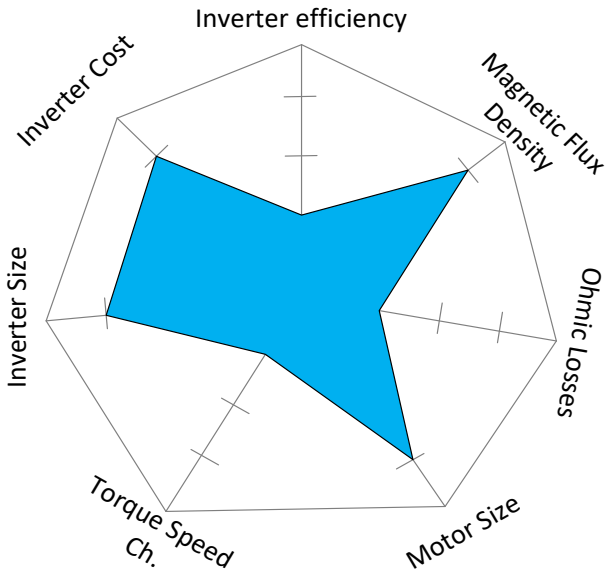

Fig. 5.27. SFIM assessment from different factors

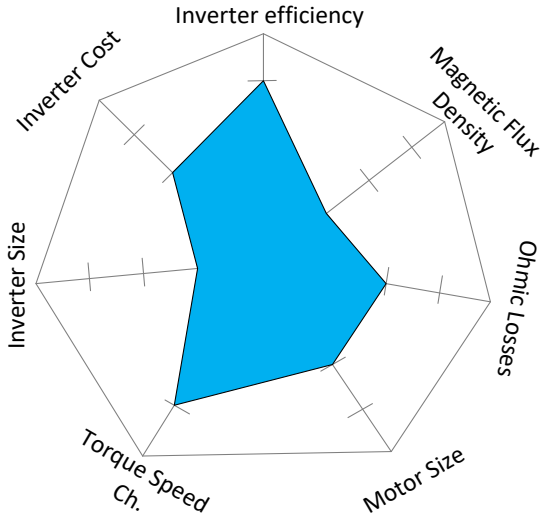

Fig. 5.28. DFIM assessment from different factors

Further, Fig. 5.29 shows the overall performance of the CDFIM, it can be seen that such configuration does offers a better Inverter efficiency and torque speed characteristics compared to the SFIM. But at the same time its overall merits and demerits are very close to the DFIM. Moreover, CDFIM is configured by two cascaded machines what increases the space envelop and the weight of the overall system without adding a significant advantage in EV/HEV applications.

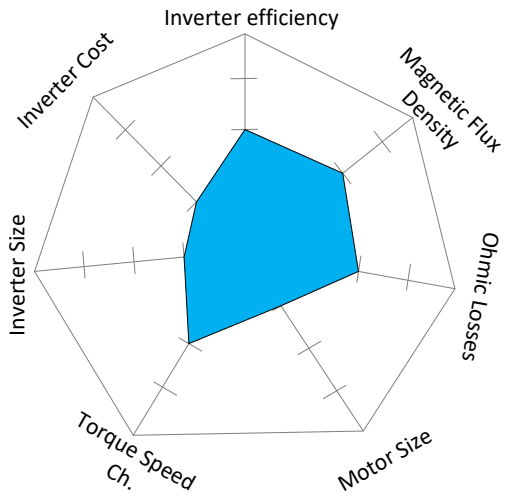

Fig. 5.29. CDFIM assessment from different factors

5.5 Chapter Summary

One of the crucial factors in optimizing the HEV/EV model is taking into account the overall efficiency of the entire system. That's why, the system has been investigated through replacing the conventional converter with the new fast response wide band gap semiconductor switches [Gallium Nitride (GaN) and Silicon Carbide (SiC)]. After performing the simulation, it can be deduced that using the GaN and SiC semiconductors reduce the power losses and hence a high frequency operation becomes viable. In terms of comparing the GaN-HEMT cascode with a SiC Trench, it has been demonstrated through the simulation results that the GaN total loss is less than the SiC Trench by 0.25% at the same frequency of 300 kHz. Therefore, the efficiency has been

improved by 2.2% in case of a GaN HEMT based converter whilst it has been improved by 2% in SiC Trench based inverter. It can be also observed that there is a constant efficiency margin ranges from 0.6%-0.7% for all tested cases under normal load. At higher frequencies, the merits of using WBG devices become obvious in terms of less passive elements and size reduction of magnetic elements and in turn leads to power density improvement and car mileage extension. As a result of operating at higher frequencies, the converter weight is reduced by 30% in comparison with the conventional converters. As a further development, future electric cars are coming back to the high efficiency induction motors; recently developed. Yet, the developed model can accommodate their performance accurately. As an introductory step; the induction motor topology selection has to be finalized before modeling.

Consequently,, the performance of the three topologies of induction motor, SFIM, DFIM and CDFIM is compared. For a fair comparison, the inverter size and the specifications of the motors are the same. Each motor is accurately simulated and the results obtained from the three simulations are quantified and analyzed. The CDFIM allows for easier flux detection especially at low and zero speeds, however, his this quite difficult in SFIM. Moreover, the CDFIM is a fault tolerant configuration due to having two inverters so it is easy to work as a SFIM in case of any failure that may happen to any inverter. Furthermore, the DFIM and the CDFIM are capable of achieving wider speed range and higher torque and power density. We can conclude that each motor has some advantages and some other drawbacks and in some applications we may sacrifice the machine weight in exchange for better efficiency and better power consumption.

Chapter 6. Conclusions and Future Work

6.1 Conclusions

6.1.1 Developing a Generic Versatile Modeling Approach for HEVs/EVs

A generic versatile modeling approach has been developed and simulated on PSIM platform based to investigate the dynamic performance of the vehicle. The transient model is used to examine the dynamical behavior of the included subsystems, design the controllers of the converters, and improve the accuracy of the results and allow for a detailed dynamic analysis. Also, it has the flexibility to be applied for all electrified vehicles. Although transient modeling is essential in studying the system dynamics but it makes the control algorithm more complex. In this thesis this model is used in the hardware-in-loop setup to simulate the vehicle behavior in real-time.

This part of the thesis is presented in 2018 IEEE Applied Power Electronics Conference and Exposition (APEC), in a paper titled " A novel platform for power train model of electric cars with experimental validation using real-time hardware in-the-loop (HIL): A case study of GM Chevrolet Volt 2nd generation,", San Antonio, TX, 2018, pp. 3510-3516.

Also, Part of this section of the thesis is published in IEEE Transactions on Transportation Electrification, in a journal titled: "Hybrid Fuel Cell/Battery Rail Car: A Feasibility Study," vol. 2, no. 4, pp. 493-503, Dec. 2016.

6.1.2 Integration of a Two-Speed Transmission System

The vehicle model was parameterized to match a prototype electric vehicle under development by the industrial partners (inMotive corporation) including the two-speed transmission system. Performance tests and driving cycles were simulated to compare the benefits of the single-speed and two-speed transmissions. The results have shown the two-speed to have significant advantages over the single-speed both in terms of performance and energy consumption. The influences of single transmission and two-speed transmission have been compared. The results have shown that the two-speed transmission gives better performance in both dynamic and economic performance. The two-speed transmission extends the vehicle's range as well as increasing the efficiency of the motor compared with the single-speed transmission. The results show clearly that the overall transmission efficiency increased by 2.2% in case of using two-speed transmission.

This part of the thesis is presented in 2017 IEEE Energy Conversion Congress and Exposition (ECCE), in a paper titled " Optimal Gear Ratios Selection for a Nissan Leaf: A Case Study of InGear Transmission System," Cincinnati, OH, 2017, pp. 2079-2085.

6.1.3 Hardware in-the-Loop Implementation

A key novel accomplishment of this thesis was the development of a hardware-in-the-loop test using the developed generic versatile approach based on transient modeling for the first time in automotive industry. A hardware in-the-Loop is used to represent the experimental verification of the proposed model. The control algorithm implemented on a dedicated DSP of the HIL system is being tested in real-time with the system power circuit built in the HIL environment. In this thesis a HIL setup with real data in the simulation loop is developed. The behaviors of the different system components are studied. The results gained from PSIM and HIL testing reveals a very close agreement which demonstrate clearly the effectiveness of the mathematical model based on real

data obtained for the Chevy Volt HEV and Nissan Leaf EV. This work provides a platform to test and model any design for a propulsion system for different HEVs/EVs. It is worth mentioning that this approach fits the need and can be expanded to model electric trains and planes. Also, this setup can be used for battery related studies including testing battery performance under different driving conditions and under different climate conditions.

Part of this section of the thesis is presented in IEEE Transactions on Power Electronics, in a journal titled " A Novel Platform for Power Train Modeling of Electric Cars with Experimental Validation Using Real-Time Hardware in-the-Loop (HIL): A Case Study of GM Chevrolet Volt 2nd Generation,", vol. PP, no. 99, pp. 1-1.

6.1.4 Integration of Wide Band Gap Devices

The WBG devices have been integrated into the dynamic model to optimize its performance. After performing the simulation, it was obvious that using the GaN and SiC semiconductors reduce the power losses and hence a high frequency operation becomes viable. In terms of comparing the GaN-HEMT cascode with a SiC Trench, it has been demonstrated through the simulation results that the GaN total loss is less than the SiC Trench by 0.25% at the same frequency of 300 kHz.

Therefore, the efficiency has been improved by 2.2% in case of a GaN HEMT based inverter whilst it has been improved by 2% in SiC Trench based inverter. It can be also observed that there is a constant efficiency margin ranges from 0.6%-0.7% for all tested cases under normal load.

This part of the thesis is published in Canadian Journal of Electrical and Computer Engineering, in a journal titled: "Wide Bandgap Devices in Electric Vehicle Converters: A Performance Survey," vol. 41, no. 1, pp. 45-54, winter 2018.

Also, Part of this section of the thesis is presented in 2018 20th European Conference on Power Electronics and Applications (EPE'18 ECCE Europe) in a paper titled "Performance of Wide Band

Gap Devices in Electric Vehicles Converters: A Case Study Evaluation," Riga, Latvia, 2018, pp. P.1-P.9.

Further, Part of this section of the thesis is presented in 2016 IEEE Transportation Electrification Conference and Expo, Asia-Pacific (ITEC Asia-Pacific) in a paper titled " SiC devices performance overview in EV DC/DC converter: A case study in a Nissan Leaf,", Busan, 2016, pp. 214-219.

6.1.5 Electric Motors Selection

As a comparison between different induction motor based topologies; the Cascaded Doubly Fed Induction Motor (CDFIM), the Doubly Fed Induction Motor (DFIM) and the Singly Fed Induction Motor (SFIM) have been investigated. The DFIM provides approximately double the torque-speed characteristics for the HEV/EV application. The new CDFIM topology introduces a new topology that exploit the advantage of reducing the total losses by replacing the slip rings and carbon brushes of the DFIM and simultaneously have a wide torque-speed operation. Simulation schematics for the three motors have been setup using PSIM software and a profound performance comparison, for the same inverter size and power ratings, among the three topologies has been conducted along with pointing out the merits and demerits of each topology. Moreover, different topologies are FEA evaluated in terms of magnetic quantities and Ohmic losses. The results obtained are verified via simulation of the three topologies. The results are in full agreement with the previous results for each motor individually explained in literature. The novelty of this work is to provide a comprehensive comparison of the three motors for the same HP rating which is done for the first time.

6.2 Future Work and Recommendations

6.2.1 Analyze Further Transmission Designs

The developed work in this thesis has shown that a multiple-speed transmission can benefit the energy consumption and performance of an electric vehicle over a two-speed transmission.

However, the research was limited to analyzing the transmissions provided by the industrial partners (inMotive corporation), i.e., the single-speed and two-speed transmissions. It would be beneficial to analyze further transmission designs such as multiple speed transmissions capable of seamless shifts, utilizing planetary gear sets to understand the benefits in terms of energy consumption over driving cycles and vehicle performance.

6.2.2 Testing New Transportation Systems

In this thesis the concept of Hardware-in-loop simulation was used to investigate the dynamic performance in HEVs/EVs. The same strategy can be applied to new transportation systems like Hyperloop. The strategies adopted in the research for selecting the gear ratio for two-speed transmission systems could be further developed to use genetic algorithms or other non-linear optimizations, or advanced controllers to minimize the computational time. The HIL setup may also be used to understand the effect of using different components on the efficiency of the transmission as this was not conducted within the research presented.

6.2.3 Further Investigation of the Cascaded Doubly-fed Induction Motor in HEV/EV Applications

Incorporating CDFIM into the transient model of the HEV/EV needs to be further investigated for both single-port electrical and dual port electrical control methodologies. In this thesis, a generic comparison between SFIM, DFIM, and CDFIM has been performed. However, it needs to be in more depth and considers different control algorithms for optimal performance.

Appendix A: Modeling Parameters

A.1 Nissan Leaf Electric Vehicle

Table A-1: Details of 2012 Nissan Leaf machine [121]

Description	Nissan Leaf IPM machine
Outer diameter of stator (mm)	200
Inner diameter of stator (mm)	131
Stack length of stator (mm)	151
Number of slot	48
Winding type	Full pitch single layer distributed winding
No. of turns per coil	8
No. of strands per turn	15
Diameter of copper wire (mm)	0.812
Outer diameter of rotor (mm)	130
Inner diameter of rotor (mm)	45
Active axial length (mm)	151
No. of poles	8
Large magnet dimensions (mm)	3.79 (DOM) 28.85 8.36*
Small magnet dimensions (mm)	2.29 (DOM) 21.3 8.34*
Total magnet mass (kg)	1.8954
Pole arc/pole pitch ratio	0.9765
Skew angle (degrees mech.)	3.75
Top speed	10,000 rpm
DC-link voltage	375 V
Stator excitation	Three-phase AC
Peak phase current amplitude (A)	625A

Table A-2: Battery Parameters [121]

Mass (Kg)	294
Chemistry	Lithium-ion Laminate type
Thermal System	Liquid active thermal control
Cells	192
Cell configuration	2 parallel, 96 series
Energy (kWh)	24
Resistance (Ω)	0.09
Capacity (Q) (Ah)	66.2

A.2 GM Chevrolet Volt

Table A-3: CVHEV Battery Parameters [17]

Mass (Kg)	183
Chemistry	Lithium-ion
Thermal System	Liquid active thermal control
Cells	192
Energy (kWh)	18.4
Resistance (Ω)	0.09
Capacity (Q) (Ah)	15

Table A-4: Motor parameters [17]

Type	Permanent Magnet Synchronous Motor (PMSM)
No. of Poles	8
Max Speed (rpm)	4000
No. of stator slots	72
Power (kW)	111

Table A-5: Chevy Volt parameters [17]

Curb Weight (kg)	1607
Passenger Maximum Weight (kg)	90
Frontal Area [A_f] (m2)	2.2
Aerodynamic Drag Coefficient (C_{dr})	0.28
Gravitational Acceleration (m/s2)	9.8
Air density (kg/m2)	1.2
Wheel radius (m)	0.367
Wheel inertia (kg/m^2)	1.1

References

[1] O. Tremblay, L.-A. Dessaint, and A.-I. Dekkiche, “A Generic Battery Model for the Dynamic Simulation of Hybrid Electric Vehicles,” *the IEEE Vehicle Power and Propulsion Conference (VPPC)*, 2007, pp. 284–289.

[2] G. Pebriyanti, “A lithium-ion battery modeling for a HIL-battery simulator,” *the International Conference on Computer, Control, Informatics and Its Applications (IC3INA)*, 2013, pp. 185–190.

[3] S. Jeschke and H. Hirsch, “Analysing the Impact of Different Electric Traction Drives on the Vehicle’s Energy Consumption Using HiL Simulation,” *the Vehicle Power and Propulsion Conference (VPPC*), 2014, pp. 1–6.

[4] J. Yu, C. Dou and X. Li, "MAS-Based Energy Management Strategies for a Hybrid Energy Generation System," in IEEE Transactions on Industrial Electronics, vol. 63, no. 6, pp. 3756-3764, June 2016.

[5] J. Jocsak, D. White, C. Armand, and R. S. Davis, “Development of the Combustion System for General Motors’ High-Efficiency Range Extender Ecotec Small Gas Engine,” *SAE International Journal of Engines*, vol. 8, no. 4, pp. 2015–01–1272, 2015.

[6] J. Deur, J. Petric, Asgari, and D. Hrovat, “Recent Advances in Control-Oriented Modeling of Automotive Power Train Dynamics,” *IEEE/ASME Transactions on Mechatronics*, vol. 11, no. 5, pp. 513–523, Oct. 2006.

[7] R. Mura, V. Utkin, and S. Onori, “Energy Management Design in Hybrid Electric Vehicles: A Novel Optimality and Stability Framework,” *IEEE Trans. on Control Systems Technology*, vol. 23, no. 4, pp. 1307–1322, Jul. 2015.

[8] H. Li, M. Steurer, K. L. Shi, S. Woodruff, and D. Zhang, “Development of a Unified Design, Test, and Research Platform for Wind Energy Systems Based on Hardware-in-the-Loop Real-Time Simulation,” *IEEE Trans. on Industrial Electronics*, vol. 53, no. 4, pp. 1144–1151, Jun. 2006.

[9] S. C. Oh, “Evaluation of Motor Characteristics for Hybrid Electric Vehicles Using the Hardware-in-the-Loop Concept,” *IEEE Trans. on Vehicular Technology*, vol. 54, no. 3, pp. 817–824, May 2005.

[10] A.-L. Allègre, R. Trigui, and A. Bouscayrol, "Flexible real-time control of a hybrid energy storage system for electric vehicles," *IET Electrical Systems in Transportation*, vol. 3, no. 3, pp. 79–85, Sep. 2013.

[11] L. Herrera, C. Li, X. Yao, and J. Wang, "FPGA-Based Detailed Real-Time Simulation of Power Converters and Electric Machines for EV HIL Applications," *IEEE Trans. on Industry Applications*, vol. 51, no. 2, pp. 1702–1712, Mar. 2015.

[12] C. Dufour, S. Cense, and J. Belanger, "FPGA-based Switched Reluctance Motor Drive and DC-DC converter models for high-bandwidth HIL real-time simulator," *the European Conference on Power Electronics and Applications (EPE-ECCE)*, 2013, pp. 1–8.

[13] J. V. Barreras *et al.*, "Functional analysis of Battery Management Systems using multi-cell HIL simulator," *the Ecological Vehicles and Renewable Energies (EVER)*, 2015, pp. 1–10.

[14] V. V. Nair and P. Pathiyil, "High dynamic HIL model for complete software testing solution of Hev/Ev," *the IEEE Transportation Electrification Conference and Exposition (ITEC)*, 2015, pp. 1–7.

[15] H. Sahin, N. Fukushima, T. Mochizuki, and I. Hagiwara, "HIL simulation evaluation of a novel hybrid-type self-powered active suspension system," *the IEEE International Conference on Industrial Technology (ICIT)*, 2010, pp. 1123–1130.

[16] S. Jeschke, H. Hirsch, M. Koppers, and D. Schramm, "HiL simulation of electric vehicles in different usage scenarios," *the IEEE International Electric Vehicle Conference (IEVC)*, 2012, pp. 1–8.

[17] S. Jurkovic, K. Rahman, B. Bae, N. Patel, and P. Savagian, "Next generation chevy volt electric machines; design, optimization and control for performance and rare-earth mitigation," *the IEEE Energy Conversion Congress and Exposition (ECCE)*, 2015, pp. 5219–5226.

[18] Ke Song, Weiguo Liu, and Guangzhao Luo, "Permanent magnet synchronous motor field oriented control and HIL Simulation," *the Vehicle Power and Propulsion Conference (VPPC)*, 2008, pp. 1–6.

[19] S. Kermani, R. Trigui, S. Delprat, B. Jeanneret, and T. M. Guerra, "PHIL Implementation of Energy Management Optimization for a Parallel HEV on a Predefined Route," *IEEE Trans. on Vehicular Technology*, vol. 60, no. 3, pp. 782–792, Mar. 2011.

[20] A. Ingalalli, H. Satheesh, and M. Kande, "Platform for Hardware In Loop Simulation," *the Power Electronics, Electrical Drives, Automation and Motion (SPEEDAM)*, 2016, pp. 41–46.

[21] M. Lemaire, P. Sicard, and J. Belanger, "Prototyping and Testing Power Electronics Systems Using Controller Hardware-In-the-Loop (HIL) and Power Hardware-In-the-Loop (PHIL) Simulations," *the Vehicle Power and Propulsion Conference (VPPC)*, 2015, pp. 1–6.

[22] C. Dufour, S. Cense, V. Jalili-Marandi, and J. Belanger, "Review of state-of-the-art solver solutions for HIL simulation of power systems, power electronic and motor drives," *the Power Electronics and Applications (EPE) Conference*, 2013, pp. 1–12.

[23] C. S. Edrington, M. Steurer, J. Langston, T. El-Mezyani, and K. Schoder, "Role of Power Hardware in the Loop in Modeling and Simulation for Experimentation in Power and Energy Systems," *Proceedings of the IEEE*, vol. 103, no. 12, pp. 2401–2409, Dec. 2015.

[24] F. Mocera and A. Soma, "Study of a Hardware-In-the-Loop bench for hybrid electric working vehicles simulation," *the Ecological Vehicles and Renewable Energies (EVER), 2017*, pp. 1–8.

[25] S. C. Oh and A. Emadi, "Test and Simulation of Axial Flux-Motor Characteristics for Hybrid Electric Vehicles," *IEEE Trans. on Vehicular Technology*, vol. 53, no. 3, pp. 912–919, May 2004.

[26] S. Dennetiere, H. Saad, B. Clerc, E. Ghahremani, W. Li, and J. Belanger, "Validation of a MMC model in a real-time simulation platform for industrial HIL tests," *the IEEE Power & Energy Society General Meeting*, 2015, pp. 1–5.

[27] D.-H. Shin *et al.*, "Verification of battery system model for environmentally friendly vehicles using a battery hardware-in-the-loop simulation," *IET Power Electronics*, vol. 6, no. 2, pp. 417–424, Feb. 2013.

[28] R. Parrish *et al.*, "Voltec Battery Design and Manufacturing," *SAE Technical Paper*, Apr. 2011.

[29] Y.-K. Jung, F. Mak, F. Qingele, and I. Alzahid, "WEX-HIL: Design of a Wireless Extensible hardware-in-the-loop real-time simulator for electric vehicle applications," *the Frontiers in Education Conference (FIE)*, 2016, pp. 1–9.

[30] N. Schetinin, N. Moriz, B. Kumar, A. Maier, S. Faltinski, and O. Niggemann, “Why do verification approaches in automation rarely use HIL-test?,” *the IEEE International Conference on Industrial Technology (ICIT)*, 2013, pp. 1428–1433.

[31] K. Li, F.-C. Chou, and J.-Y. Yen, “Real-Time, Energy-Efficient Traction Allocation Strategy for the Compound Electric Propulsion System,” *IEEE/ASME Trans. on Mechatronics*, vol. 22, no. 3, pp. 1371–1380, Jun. 2017.

[32] A. Cordoba-Arenas, S. Onori, Y. Guezennec, and G. Rizzoni, “Capacity and power fade cycle-life model for plug-in hybrid electric vehicle lithium-ion battery cells containing blended spinel and layered-oxide positive electrodes,” *Journal of Power Sources*, vol. 278, pp. 473–483, Mar. 2015.

[33] T. Xia, M. Li, P. Zi, L. Tian, X. Qin and N. An, "Modeling and simulation of Battery Energy Storage System (BESS) used in power system," 2015 5th International Conference on Electric Utility Deregulation and Restructuring and Power Technologies (DRPT), Changsha, 2015, pp. 2120-2125.

[34] L. Tribioli and S. Onori, “Analysis of energy management strategies in plug-in hybrid electric vehicles: Application to the GM Chevrolet Volt,” *the American Control Conference (ACC)*, 2013, pp. 5966–5971.

[35] Weiguo Liu, Guangzhao Luo, Nannan Zhao, and Manfeng Dou, “Design and HIL simulation of proportional compression salient-pole permanent magnet synchronous motor for electrical traction vehicle,” the *IEEE Vehicle Power and Propulsion Conference (VPPC)*, 2009, pp. 884–889.

[36] E. Tara *et al.*, “Dynamic Average-Value Modeling of Hybrid-Electric Vehicular Power Systems,” *IEEE Transactions on Power Delivery*, vol. 27, no. 1, pp. 430–438, Jan. 2012.

[37] Y. Cao, R. C. Kroeze and P. T. Krein, "Multi-timescale Parametric Electrical Battery Model for Use in Dynamic Electric Vehicle Simulations," in IEEE Transactions on Transportation Electrification, vol. 2, no. 4, pp. 432-442, Dec. 2016.

[38] G. Pebriyanti, “A lithium-ion battery modeling for a HIL-battery simulator,” in *2013 International Conference on Computer, Control, Informatics and Its Applications (IC3INA)*, Jakarta, Indonesia, 2013, pp. 185–190.

[39] S. Jeschke and H. Hirsch, "Analysing the Impact of Different Electric Traction Drives on the Vehicle's Energy Consumption Using HiL Simulation," *the Vehicle Power and Propulsion Conference (VPPC)*, 2014, pp. 1–6.

[40] N. Roshandel Tavana and V. Dinavahi, "A General Framework for FPGA-Based Real-Time Emulation of Electrical Machines for HIL Applications," *IEEE Transactions on Industrial Electronics*, vol. 62, no. 4, pp. 2041–2053, Apr. 2015.

[41] M. Goetz, "Integrated powertrain control for twin clutch transmissions," Thesis (PhD), University of Leeds, 2005.

[42] C. R. Ciesla and M. J. Jennings, "A Modular Approach to Powertrain Modeling and Shift Quality Analysis," *Journal of materials & manufacturing*, 1995.

[43] J. J. Moskwa, S. A. Munns, and Z. J. Rubin, "Development of system analysis methodologies and tools for modeling and optimizing vehicle system efficiency," Ph.D. Thesis, University of Michigan, 2007.

[44] G. Lucente, M. Montanari, and C. Rossi, "Modelling of an automated manual transmission system," *Mechatronics*, vol. 17, no. 2–3, pp. 73–91, Mar. 2007.

[45] L. Glielmo, L. Iannelli, V. Vacca, and F. Vasca, "Gearshift control for automated manual transmissions," *IEEE/ASME Transactions on Mechatronics*, vol. 11, no. 1, pp. 17–26, Feb. 2006.

[46] P. D. Walker and N. Zhang, "Modelling of dual clutch transmission equipped powertrains for shift transient simulations," *Mechanism and Machine Theory*, vol. 60, pp. 47–59, Feb. 2013.

[47] G. A. Hubbard and K. Youcef-Toumi, "Modeling and simulation of a hybrid-electric vehicle powertrain," in *Proceedings of the 1997 American Control Conference (Cat. No.97CH36041)*, Albuquerque, NM, USA, 1997, pp. 636–640 vol.1.

[48] D. Hrovat and W. E. Tobler, "Bond graph modeling of automotive power trains," *Journal of the Franklin Institute*, vol. 328, no. 5–6, pp. 623–662, Jan. 1991.

[49] J. Deur, J. Petric, Asgari, and D. Hrovat, "Recent Advances in Control-Oriented Modeling of Automotive Power Train Dynamics," *IEEE/ASME Transactions on Mechatronics*, vol. 11, no. 5, pp. 513–523, Oct. 2006.

[50] B. Mashadi and S. A. M. Emadi, "Dual-Mode Power-Split Transmission for Hybrid Electric Vehicles," *IEEE Transactions on Vehicular Technology*, vol. 59, no. 7, pp. 3223–3232, Sep. 2010.

[51] M. S. Rahimi Mousavi and B. Boulet, "Modeling, simulation and control of a seamless two-speed automated transmission for electric vehicles," in *2014 American Control Conference*, Portland, OR, USA, 2014, pp. 3826–3831.

[52] H. V. Alizadeh, M. K. Helwa, and B. Boulet, "Constrained control of the synchromesh operating state in an electric vehicle's clutchless automated manual transmission," in *2014 IEEE Conference on Control Applications (CCA)*, Juan Les Antibes, France, 2014, pp. 623–628.

[53] H. V. Alizadeh and B. Boulet, "Robust control of synchromesh friction in an electric vehicle's clutchless automated manual transmission," in *2014 IEEE Conference on Control Applications (CCA)*, Juan Les Antibes, France, 2014, pp. 611–616.

[54] H. V. Alizadeh, M. S. R. Mousavi, and B. Boulet, "Synchromesh Torque Estimation in an Electric Vehicle's Clutchless Automated Manual Transmission Using Unknown Input Observer," in *2015 IEEE Vehicle Power and Propulsion Conference (VPPC)*, Montreal, QC, Canada, 2015, pp. 1–5.

[55] H. Naunheimer, B. Bertsche, J. Ryborz, and W. Novak, *Automotive Transmissions*. Berlin, Heidelberg: Springer Berlin Heidelberg, 2011.

[56] E. Galvagno, M. Velardocchia, and A. Vigliani, "Dynamic and kinematic model of a dual clutch transmission," *Mechanism and Machine Theory*, vol. 46, no. 6, pp. 794–805, Jun. 2011.

[57] Namwook Kim, Sukwon Cha, and Huei Peng, "Optimal Control of Hybrid Electric Vehicles Based on Pontryagin's Minimum Principle," *IEEE Transactions on Control Systems Technology*, vol. 19, no. 5, pp. 1279–1287, Sep. 2011.

[58] N. Srivastava and I. Haque, "Nonlinear dynamics of a friction-limited drive: Application to a chain continuously variable transmission (CVT) system," *Journal of Sound and Vibration*, vol. 321, no. 1–2, pp. 319–341, Mar. 2009.

[59] N. Srivastava and I. Haque, "Transient dynamics of metal V-belt CVT: Effects of band pack slip and friction characteristic," *Mechanism and Machine Theory*, vol. 43, no. 4, pp. 459–479, Apr. 2008.

[60] G.-H. Jung, B.-H. Cho, and K.-I. Lee, *Dynamic Analysis and Closed-Loop Shifting Control of EF-Automatic Transmission with Proportional Control Solenoid Valves*. 2000.

[61] A. Haj-Fraj and F. Pfeiffer, "Dynamic modeling and analysis of automatic transmissions," in *1999 IEEE/ASME International Conference on Advanced Intelligent Mechatronics (Cat. No.99TH8399)*, Atlanta, GA, USA, 1999, pp. 1026–1031.

[62] C. Lazar, F. C. Caruntu, and A. E. Balau, "Modelling and predictive control of an electro-hydraulic actuated wet clutch for automatic transmission," in *2010 IEEE International Symposium on Industrial Electronics*, Bari, 2010, pp. 256–261.

[63] H. Adibi Asl, N. Lashgarian Azad, and J. McPhee, "Modeling Torque Converter Characteristics in Automatic Drivelines: Lock-up Clutch and Engine Braking Simulation," in *Volume 6: 1st Biennial International Conference on Dynamics for Design; 14th International Conference on Advanced Vehicle Technologies*, Chicago, Illinois, USA, 2012, p. 359.

[64] A. Khajepour, S. Fallah, and A. Goodarzi, *Electric and hybrid vehicles: technologies, modeling, and control ; a mechatronic approach*. Chichester, West Sussex, United Kingdom: Wiley, 2014.

[65] I. Husain, *Electric and hybrid vehicles: design fundamentals*, 2nd ed. Boca Raton, FL: CRC Press, 2011.

[66] A. Ge, H. Jin, and Y. Lei, *Engine Constant Speed Control in Starting and Shifting Process of Automated Mechanical Transmission (AMT)*. 2018.

[67] B. Gao, Q. Liang, Y. Xiang, L. Guo, and H. Chen, "Gear ratio optimization and shift control of 2-speed I-AMT in electric vehicle," *Mechanical Systems and Signal Processing*, vol. 50–51, pp. 615–631, Jan. 2015.

[68] Q. Liang, B. Z. Gao, and H. Chen, "Gear Shifting Control for Pure Electric Vehicle with Inverse-AMT," *Applied Mechanics and Materials*, vol. 190–191, pp. 1286–1289, Jul. 2012.

[69] B. Zhu, N. Zhang, P. Walker, W. Zhan, X. Zhou, and J. Ruan, "Two-Speed DCT Electric Powertrain Shifting Control and Rig Testing," *Advances in Mechanical Engineering*, vol. 5, p. 323917, Jan. 2013.

[70] X. Zhou, P. Walker, N. Zhang, B. Zhu, and J. Ruan, "Study of Power Losses in a Two-Speed Dual Clutch Transmission," *the SAE 2014 World Congress & Exhibition*, 2014.

[71] M. S. Rahimi Mousavi and B. Boulet, "Dynamical modeling and optimal state estimation using Kalman-Bucy filter for a seamless two-speed transmission for electric vehicles," in *2015 23rd Mediterranean Conference on Control and Automation (MED)*, Torremolinos, Malaga, Spain, 2015, pp. 76–81.

[72] K. B. Siriyapuraju, V. Konduru, and P. Eswaramoorthy, "Detent Profile Optimization to Improve Shift Quality of Manual Transmissions," *the SAE 2015 World Congress & Exhibition*, 2015.

[73] M. P. Gahagan, T. Yoshimura, and J. N. Vinci, "Technologies for Modern Manual Transmission Performance," *the 2003 JSAE/SAE International Spring Fuels and Lubricants Meeting*, 2003.

[74] M. Kubur, A. Kahraman, D. M. Zini, and K. Kienzle, "Dynamic Analysis of a Multi-Shaft Helical Gear Transmission by Finite Elements: Model and Experiment," *Journal of Vibration and Acoustics*, vol. 126, no. 3, p. 398, 2004.

[75] X. Li, W. Zhang, J. Li, M. Jiang, and Y. Zhang, "Analysis on Synchronizer of Manual Transmission using Finite Element Analysis," *the SAE 2015 World Congress & Exhibition*, 2015.

[76] A. Sorniotti *et al.*, "Analysis and simulation of the gearshift methodology for a novel two-speed transmission system for electric powertrains with a central motor," *Proceedings of the Institution of Mechanical Engineers, Part D: Journal of Automobile Engineering*, vol. 226, no. 7, pp. 915–929, Jul. 2012.

[77] D. W. Wenthen, "Two-speed transaxle gearbox for electric vehicles," 8,517,882.

[78] M. Zeraoulia, M. E. H. Benbouzid, and D. Diallo, "Electric Motor Drive Selection Issues for HEV Propulsion Systems: A Comparative Study," *IEEE Transactions on Vehicular Technology*, vol. 55, no. 6, pp. 1756–1764, Nov. 2006.

[79] K. T. Chau, C. C. Chan, and Chunhua Liu, "Overview of Permanent-Magnet Brushless Drives for Electric and Hybrid Electric Vehicles," *IEEE Transactions on Industrial Electronics*, vol. 55, no. 6, pp. 2246–2257, Jun. 2008.

[80] R. N. Tuncay, O. Ustun, M. Yilmaz, C. Gokce, and U. Karakaya, "Design and implementation of an electric drive system for in-wheel motor electric vehicle applications," in *2011 IEEE Vehicle Power and Propulsion Conference*, Chicago, IL, USA, 2011, pp. 1–6.

[81] T. Jahns, "Getting Rare-Earth Magnets Out of EV Traction Machines: A review of the many approaches being pursued to minimize or eliminate rare-earth magnets from future EV powertrains," *IEEE Electrification Magazine*, vol. 5, no. 1, pp. 6–18, 2017.

[82] A. Dadashnialehi, A. Bab-Hadiashar, Z. Cao, and R. Hoseinnezhad, "Reliable EMF-Sensor-Fusion-Based Antilock Braking System for BLDC Motor In-Wheel Electric Vehicles," *IEEE Sensors Letters*, vol. 1, no. 3, pp. 1–4, 2017.

[83] Z. Yang, F. Shang, I. P. Brown, and M. Krishnamurthy, "Comparative Study of Interior Permanent Magnet, Induction, and Switched Reluctance Motor Drives for EV and HEV Applications," *IEEE Transactions on Transportation Electrification*, vol. 1, no. 3, pp. 245–254, 2015.

[84] W. Ding, S. Yang, Y. Hu, S. Li, T. Wang, and Z. Yin, "Design Consideration and Evaluation of a 12/8 High-Torque Modular-Stator Hybrid Excitation Switched Reluctance Machine for EV Applications," *IEEE Transactions on Industrial Electronics*, vol. 64, no. 12, pp. 9221–9232, 2017.

[85] A. Haddoun, M. E. H. Benbouzid, D. Diallo, R. Abdessemed, J. Ghouili, and K. Srairi, "A loss-minimization DTC scheme for EV induction motors," *IEEE Transactions on Vehicular Technology*, vol. 56, no. 1, pp. 81–88, 2007.

[86] H. E. V Applications, P. Han, S. Member, M. Cheng, Z. Chen, and S. Member, "Dual-Electrical-Port Control of Cascaded Doubly-Fed Induction Machine," *IEEE Transactions on Industry Applications*, vol. 53, no. 2, pp. 1390–1398, 2017.

[87] H. E. V Applications, P. Han, S. Member, M. Cheng, Z. Chen, and S. Member, "Single-Electrical-Port Control of Cascaded Doubly-Fed Induction Machine," *IEEE Transactions on Power Electronics*, vol. 32, no. 9, pp. 7233–7243, 2017.

[88] J. J. Eckert, L. C. A. Silva, E. S. Costa, F. M. Santiciolli, F. G. Dedini, and F. C. Corrêa, "Electric vehicle powertrain optimisation," *IET Electrical Systems in Transportation*, vol. 7, no. 1, pp. 32–40, 2017.

[89] L. Xu, Y. Liu, and X. Wen, "Comparison study of singly-fed electric machine with doubly-fed machine for EV/HEV applications," *2011 International Conference on Electrical Machines and Systems, ICEMS 2011*, pp. 2–6, 2011.

[90] Z. Zhang, L. Shi, Q. Ge, and Y. Li, "Characteristics analysis of single-sided ironless linear synchronous motor based on permanent magnet Halbach array," *2015 18th International Conference on Electrical Machines and Systems, ICEMS 2015*, pp. 275–278, 2016.

[91] F. Yi and W. Cai, "Modeling, Control, and Seamless Transition of the Bidirectional Battery-Driven Switched Reluctance Motor/Generator Drive Based on Integrated Multiport Power Converter for Electric Vehicle Applications," *IEEE Transactions on Power Electronics*, vol. 31, no. 10, pp. 7099–7111, 2016.

[92] T. Puleva, G. Rouzhekov, T. Slavov, and B. Rakov, "Hardware in the loop (HIL) simulation of wind turbine power control," in *Mediterranean Conference on Power Generation, Transmission, Distribution and Energy Conversion (MedPower 2016)*, Belgrade, Serbia, 2016, pp. 64 (8 .)-64 (8 .).

[93] K. Li, F.-C. Chou, and J.-Y. Yen, "Real-Time, Energy-Efficient Traction Allocation Strategy for the Compound Electric Propulsion System," *IEEE/ASME Transactions on Mechatronics*, vol. 22, no. 3, pp. 1371–1380, Jun. 2017.

[94] S. Kermani, R. Trigui, S. Delprat, B. Jeanneret, and T. M. Guerra, "PHIL Implementation of Energy Management Optimization for a Parallel HEV on a Predefined Route," *IEEE Transactions on Vehicular Technology*, vol. 60, no. 3, pp. 782–792, Mar. 2011.

[95] J. P. F. Trovao, V. D. N. Santos, C. H. Antunes, P. G. Pereirinha, and H. M. Jorge, "A Real-Time Energy Management Architecture for Multisource Electric Vehicles," *IEEE Transactions on Industrial Electronics*, vol. 62, no. 5, pp. 3223–3233, May 2015.

[96] S. C. Oh and A. Emadi, "Test and Simulation of Axial Flux-Motor Characteristics for Hybrid Electric Vehicles," *IEEE Transactions on Vehicular Technology*, vol. 53, no. 3, pp. 912–919, May 2004.

[97] Y. Liu, M. Steurer, and P. Ribeiro, "A Novel Approach to Power Quality Assessment: Real Time Hardware-in-the-Loop Test Bed," *IEEE Trans. on Power Delivery*, vol. 20, no. 2, pp. 1200–1201, Apr. 2005.

[98] W. C. Lee and D. Drury, "Development of a Hardware-in-the-Loop Simulation System for Testing Cell Balancing Circuits," *IEEE Trans. on Power Electronics*, vol. 28, no. 12, pp. 5949–5959, Dec. 2013.

[99] X. Huang, Q. Li, Z. Liu, and F. C. Lee, "Analytical Loss Model of High Voltage GaN HEMT in Cascode Configuration," *IEEE Transactions on Power Electronics*, vol. 29, no. 5, pp. 2208–2219, May 2014.

[100] C. Zhao *et al.*, "Design and Implementation of a GaN-Based, 100-kHz, 102-W/in ^{3} Single-Phase Inverter," *IEEE Journal of Emerging and Selected Topics in Power Electronics*, vol. 4, no. 3, pp. 824–840, Sep. 2016.

[101] Y. S. Noh and I. B. Yom, "A Linear GaN High Power Amplifier MMIC for Ka-Band Satellite Communications," *IEEE Microwave and Wireless Components Letters*, vol. 26, no. 8, pp. 619–621, Aug. 2016.

[102] X. Huang, Z. Liu, Q. Li, and F. C. Lee, "Evaluation and Application of 600 V GaN HEMT in Cascode Structure," *IEEE Trans. on Power Electronics*, vol. 29, no. 5, pp. 2453–2461, May 2014.

[103] A. Lidow, J. Strydom, R. Strittmatter, and C. Zhou, "GaN: A Reliable Future in Power Conversion: Dramatic performance improvements at a lower cost," *IEEE Power Electronics Magazine*, vol. 2, no. 1, pp. 20–26, Mar. 2015.

[104] E. Tara, S. Filizadeh, and E. Dirks, "Battery-in-the-Loop Simulation of a Planetary-Gear-Based Hybrid Electric Vehicle," *IEEE Trans. on Vehicular Technology*, vol. 62, no. 2, pp. 573–581, Feb. 2013.

[105] P. D. Walker and N. Zhang, "Modelling of dual clutch transmission equipped powertrains for shift transient simulations," *Mechanism and Machine Theory*, vol. 60, pp. 47–59, Feb. 2013.

[106] A. S. Abdelrahman, K. S. Algarny, and M. Z. Youssef, "Optimal gear ratios selection for a nissan leaf: A case study of InGear transmission system," in *2017 IEEE Energy Conversion Congress and Exposition (ECCE)*, Cincinnati, OH, 2017, pp. 2079–2085.

[107] A. S. Abdelrahman, K. S. Algarny, and M. Z. Youssef, "A Novel Platform for Powertrain Modeling of Electric Cars With Experimental Validation Using Real-Time Hardware in the Loop (HIL): A Case Study of GM Second Generation Chevrolet Volt," *IEEE Transactions on Power Electronics*, vol. 33, no. 11, pp. 9762–9771, Nov. 2018.

[108] D. T. Greenwood, *Advanced dynamics*, Digitally printed 1st pbk. version. Cambridge; New York: Cambridge University Press, 2006.

[109] B. Eller and J.-F. Hetet, “Study of an optimization criterion of mounting blocks for drivability evaluation of an electric vehicle,” in *2010 IEEE Vehicle Power and Propulsion Conference*, Lille, France, 2010, pp. 1–6.

[110] P. J. Kollmeyer, “Development and Implementation of a Battery-Electric Light-Duty Class 2a Truck including Hybrid Energy Storage,” p. 475, 2015.

[111] K. Jalali, “Stability Control of Electric Vehicles with In-wheel Motors,” 2010.

[112] F. Di Nicola, A. Sorniotti, T. Holdstock, F. Viotto, and S. Bertolotto, “Optimization of a Multiple-Speed Transmission for Downsizing the Motor of a Fully Electric Vehicle,” *SAE International Journal of Alternative Powertrains*, vol. 1, no. 1, pp. 134–143, Apr. 2012.

[113] L. Herrera, C. Li, X. Yao, and J. Wang, “FPGA-Based Detailed Real-Time Simulation of Power Converters and Electric Machines for EV HIL Applications,” *IEEE Trans. on Industry Applications*, vol. 51, no. 2, pp. 1702–1712, Mar. 2015.

[114] D. N. Dyck, T. Rahman, and C. Dufour, “Internally Consistent Nonlinear Behavioral Model of a PM Synchronous Machine for Hardware-in-the-Loop Simulation,” *IEEE Trans. on Magnetics*, vol. 50, no. 2, pp. 853–856, Feb. 2014.

[115] Ke Song, Weiguo Liu, and Guangzhao Luo, “Permanent magnet synchronous motor field oriented control and HIL Simulation,” *the Vehicle Power and Propulsion Conference (VPPC)*, 2008, pp. 1–6.

[116] C. Dufour, S. Cense, and J. Belanger, “FPGA-based Switched Reluctance Motor Drive and DC-DC converter models for high-bandwidth HIL real-time simulator,” *the European Conference on Power Electronics and Applications (EPE-ECCE)*, 2013, pp. 1–8.

[117] A. Cordoba-Arenas, S. Onori, Y. Guezennec, and G. Rizzoni, “Capacity and power fade cycle-life model for plug-in hybrid electric vehicle lithium-ion battery cells containing blended spinel and layered-oxide positive electrodes,” *Journal of Power Sources*, vol. 278, pp. 473–483, Mar. 2015.

[118] N. Daniil and D. Drury, "Investigation and validation of methods to implement a two-quadrant battery emulator for power Hardware-in-the-Loop Simulation," *IECON 2016 - 42nd Annual Conference of the IEEE Industrial Electronics Society*, Florence, 2016, pp. 2070-2075. .

[119] R. Parrish *et al.*, "Voltec Battery Design and Manufacturing," *SAE Technical Paper*, Apr. 2011.

[120] W. Li and J. Belanger, "An Equivalent Circuit Method for Modelling and Simulation of Modular Multilevel Converters in Real-Time HIL Test Bench," *IEEE Trans. on Power Delivery*, vol. 31, no. 5, pp. 2401–2409, Oct. 2016.

[121] T. Burress, "Benchmarking of Competitive Technologies," p. 30.

[122] Y. Hori, "Future Vehicle Driven by Electricity and Control—Research on Four-Wheel-Motored 'UOT Electric March II,'" *IEEE Trans. on Industrial Electronics*, vol. 51, no. 5, pp. 954–962, Oct. 2004.

[123] A. E. Qinglian Ren, "Performance Analysis of Hybrid and Full Electrical Vehicles Equipped with Continuously Variable Transmissions," *Advances in Automobile Engineering*, vol. 02, no. 01, 2013.

[124] B. K. Powell, K. E. Bailey, and S. R. Cikanek, "Dynamic modeling and control of hybrid electric vehicle powertrain systems," *IEEE Control Systems Magazine*, vol. 18, no. 5, pp. 17–33, Oct. 1998.

[125] S. Amjad, S. Neelakrishnan, and R. Rudramoorthy, "Review of design considerations and technological challenges for successful development and deployment of plug-in hybrid electric vehicles," *Renewable and Sustainable Energy Reviews*, vol. 14, no. 3, pp. 1104–1110, Apr. 2010.

[126] A. Vasebi, M. Partovibakhsh, and S. M. T. Bathaee, "A novel combined battery model for state-of-charge estimation in lead-acid batteries based on extended Kalman filter for hybrid electric vehicle applications," *Journal of Power Sources*, vol. 174, no. 1, pp. 30–40, Nov. 2007.

[127] G. Sivaramaiah and V. R. Subramanian, "An overview of the development of lead/acid traction batteries for electric vehicles in India," *Journal of Power Sources*, vol. 38, no. 1–2, pp. 165–170, Mar. 1992.

[128] J. P. F. Trovao, V. D. N. Santos, C. H. Antunes, P. G. Pereirinha, and H. M. Jorge, "A Real-Time Energy Management Architecture for Multisource Electric Vehicles," *IEEE Trans. on Industrial Electronics*, vol. 62, no. 5, pp. 3223–3233, May 2015.

[129] S. C. Oh and A. Emadi, "Test and Simulation of Axial Flux-Motor Characteristics for Hybrid Electric Vehicles," *IEEE Trans. on Vehicular Technology*, vol. 53, no. 3, pp. 912–919, May 2004.

[130] K. M. Rahman, S. Jurkovic, C. Stancu, J. Morgante, and P. J. Savagian, "Design and Performance of Electrical Propulsion System of Extended Range Electric Vehicle (EREV) Chevrolet Volt," *IEEE Trans. on Industry Applications*, vol. 51, no. 3, pp. 2479–2488, May 2015.

[131] K. Algarny, A. S. Abdelrahman, and M. Youssef, "A novel platform for power train model of electric cars with experimental validation using real-time hardware in-the-loop (HIL): A case study of GM Chevrolet Volt 2nd generation," in *2018 IEEE Applied Power Electronics Conference and Exposition (APEC)*, San Antonio, TX, USA, 2018, pp. 3510–3516.

[132] Y. Zhang, R. Xiong, H. He, and W. Shen, "Lithium-Ion Battery Pack State of Charge and State of Energy Estimation Algorithms Using a Hardware-in-the-Loop Validation," *IEEE Trans. on Power Electronics*, vol. 32, no. 6, pp. 4421–4431, Jun. 2017.

[133] G. Pebriyanti, "A lithium-ion battery modeling for a HIL-battery simulator," *the International Conference on Computer, Control, Informatics and Its Applications (IC3INA)*, 2013, pp. 185–190.

[134] C. S. Edrington, M. Steurer, J. Langston, T. El-Mezyani, and K. Schoder, "Role of Power Hardware in the Loop in Modeling and Simulation for Experimentation in Power and Energy Systems," *Proceedings of the IEEE*, vol. 103, no. 12, pp. 2401–2409, Dec. 2015.

[135] K. Liu, H. Tian, and Y. Zhang, "Development of HIL simulation platform for metro vehicle Linear induction motor driving system," the *IEEE International Conference on Mechatronics and Automation (ICMA)*, 2015, pp. 403–408.

[136] H. Sahin, N. Fukushima, T. Mochizuki, and I. Hagiwara, "HIL simulation evaluation of a novel hybrid-type self-powered active suspension system," the *IEEE International Conference on Industrial Technology (ICIT)*, 2010, pp. 1123–1130.

[137] S. Jeschke, H. Hirsch, M. Koppers, and D. Schramm, "HiL simulation of electric vehicles in different usage scenarios," the *IEEE International Electric Vehicle Conference (IEVC)*, 2012, pp. 1–8.

[138] N. Roshandel Tavana and V. Dinavahi, "A General Framework for FPGA-Based Real-Time Emulation of Electrical Machines for HIL Applications," *IEEE Trans. on Industrial Electronics*, vol. 62, no. 4, pp. 2041–2053, Apr. 2015.

[139] K. Hamada, M. Nagao, M. Ajioka, and F. Kawai, "SiC—Emerging Power Device Technology for Next-Generation Electrically Powered Environmentally Friendly Vehicles," *IEEE Trans. on Electron Devices*, vol. 62, no. 2, pp. 278–285, Feb. 2015.

[140] H. Mejbri, K. Ammous, S. Abid, H. Morel, and A. Ammous, "Bi-objective sizing optimization of power converter using genetic algorithms: Application to photovoltaic systems," *COMPEL - The international journal for computation and mathematics in electrical and electronic engineering*, vol. 33, no. 1/2, pp. 398–422, Dec. 2013.

[141] P. Choi, U. Radhakrishna, C.-C. Boon, D. Antoniadis, and L.-S. Peh, "A Fully Integrated Inductor-Based GaN Boost Converter With Self-Generated Switching Signal for Vehicular Applications," *IEEE Transactions on Power Electronics*, vol. 31, no. 8, pp. 5365–5368, Aug. 2016.

[142] D. J. Meyer *et al.*, "Epitaxial Lift-Off and Transfer of III-N Materials and Devices from SiC Substrates," *IEEE Transactions on Semiconductor Manufacturing*, vol. 29, no. 4, pp. 384–389, Nov. 2016.

[143] E. Gurpinar and A. Castellazzi, "Single-Phase T-Type Inverter Performance Benchmark Using Si IGBTs, SiC MOSFETs and GaN HEMTs," *IEEE Transactions on Power Electronics*, pp. 1–1, 2015.

[144] A. Bindra, "Wide-Bandgap-Based Power Devices: Reshaping the power electronics landscape," *IEEE Power Electronics Magazine*, vol. 2, no. 1, pp. 42–47, Mar. 2015.